

UNIVERSITÀ DEGLI STUDI DI PADOVA



Facoltà di Scienze MM. FF. NN.

Dipartimento di Scienze Chimiche

Tesi di Laurea Magistrale in Chimica

**Electrochemical Immunosensors and
Peptide Self-Assembled Monolayers
for Cancer Biomarker Protein
Detection**

Relatore: Prof. Flavio Maran

Correlatore: Prof. James F. Rusling (University of Connecticut, USA)

Controrelatore: Prof. Fabrizio Mancin

Laureando: Alice Soldà

Anno Accademico 2009-2010

*“Non basta guardare,
occorre guardare con occhi che vogliono vedere,
e che credono in quello che vedono.”*

(Galileo Galilei)

Acknowledgments

I would like to thank Prof. Flavio Maran for believing in me since the first time. He gave me the opportunity to complete my Thesis work in the University of Connecticut (UCONN, Storrs, CT). Most importantly, I would like to thank him for his moral and financial support, and for the thousands of good advice that helped me to grow professionally and temperamentally in these months.

I would like to thank Prof. James Rusling, (Department of Chemistry of the University of the Connecticut – UCONN, Storrs, CT) for his great hospitality, the financial support and the opportunity that he gave me to work in his research group: in those months, I learnt many things about the immunosensors' world.

I would like also to thank Dr. Dharamainder Chaudary (UCONN Health Center, Farmington, CT) to provide me Nanog biomarker samples and the relative antibodies and Prof. Edward Samulski (Department of Chemistry, University of North Carolina, Chapel Hill, NC) for clearing to all my doubts about IRRAS investigation, even though he did not know me directly.

I am grateful to all members of Prof. Maran's group: from Dr. Sabrina Antonello, who constantly helped and supported me even in the most critical moments with good advices, to Martina for her friendship and for making more pleasant the hard lab's days with her songs and Ivan, for providing me all peptides, even in relatively short times. A special thank is addressed to Pierangelo, which initially convinced me to take this road and after passed me his knowledge about SAMs' procedure ... *(lo ringrazio un po' meno per le costanti battutine a doppio senso con cui mi perseguitava ogni giorno)*.

I am grateful also to all members of Prof. Rusling's group that followed and helped me during the period that I spent there. In particular Bhaskara, for teaching me everything I know now about the biosensors *(although sometimes the experiments followed more a mystical way, that a scientific one with all those "Abrakadabra")*, and Ruchika for her support and advices. I would say also thanks to Ahbay, Danuka, Vigneshwaran, Alex, Linlin, Collen, Sadagopan, Niamesh, Shenmin, and the others.

Index

Chapter 1. Introduction	9
1.1 Biosensors	9
1.1.1 Electrochemical Immunosensors	11
1.1.2 Microfluidic Electrochemical Device for High Sensitivity Biosensing	13
1.1.3 Nanog Protein as Biomarker of Cancer	14
1.2 Self-Assembled Monolayers (SAMs) as a Platform for Biosensors	16
1.2.1 Electron Transfer through SAMs	17
1.2.2 Self-Assembled Monolayer	19
1.2.3 Types of Substrates and Characterization of SAMs	21
1.2.4 Nature of the Metal-SAM Interface.....	23
1.2.5 Organization of the Organic Layer	25
1.3 Gold Electrochemical Biosensors	27
1.4 α -Aminoisobutyric Acid 3_{10} -Helices as Adsorbate for SAMs.....	28
1.4.1 Characteristic of the Investigated Aib-Homopeptides	33
1.5 Purposes of the Thesis	36
Chapter 2. Experimental	38
2.1 Chemicals.....	38
2.2 Preparation of HRP Single Electrodes.....	38
2.3 Fabrication of the Microfluidic Device and Preparation of Eight-Electrode Array.....	42

2.4 Gold Preparation and SAM Formation	44
2.5 Instruments	46
2.5.1 Electrochemistry.....	46
2.5.2 IRRAS	46
Chapter 3. Results and Discussion	47
3.1 Electrochemical Immunosensors.....	47
3.1.1 Characterization of AuNP Platform	47
3.1.2 Electrochemistry Immunosensors	50
3.1.3 Analysis of the Immunosensors' Performance.....	53
3.2 IRRAS Characterization of Peptide SAM.....	69
3.2.1 The Metal-Surface Selection Rule	70
3.2.2 Characterization of Aib-Homopeptides	74
3.2.3 Characterization of Aib-Homopeptide SAMs.....	79
3.2.4 Determination of the Orientation of Adsorbed Molecules.....	93
3.2.5 Determination of the Thickness of the Monolayer.....	100
Chapter 4. Conclusions	103
Chapter 5. References	107

1. Introduction

1.1 Biosensors

The IUPAC definition of a chemical sensor is a: “a device that transforms chemical information, ranging from the concentration of a specific sample component to total composition analysis, into an analytically useful signal. The chemical information may originate from a chemical reaction of the analyte or from a physical property of the system investigated. A chemical sensor is an essential component of an analyzer. In addition to the sensor, the analyzer may contain devices that perform the following processing. Chemical sensors contain two basic functional units: a receptor part and a transducer part. In the receptor part of a sensor, the chemical information is transformed into a form of energy that may be measured by the transducer. The transducer part is a device capable of transforming the energy carrying the chemical information about the sample into a useful analytical signal”.¹

“A biosensor is a particular kind of chemical sensor that uses specific biochemical reactions mediated by isolated enzymes, immunosystems, tissues, organelles or whole cells to detect chemical compounds usually by electrical, thermal or optical signal”.¹ Nowadays the interest about biosensors is rapidly increasing especially in the fields of health care, food and environmental quality.

A representative example is provided by the glucose biosensor, which is used by millions diabetic people all over the world. Now people can make by themselves a fast control of their glucose level everywhere and, depending on the output of the sensor, they can inject the exact amount of insulin to bring the glucose to an optimal level.²

For these reasons, economic investments aimed to supporting the biosensor research are increasing. The technology behind biosensors is wide and multidisciplinary, ranging from biology, chemistry, engineering and electronics, all these disciplines being necessary to create a well performing biosensor.^{3,4}

A biosensor is made by two essential components integrated: a bioreceptor and a transducer. The first one is a biological molecule that can specifically interact and recognize the molecules present in the sample analyte, for example proteins, DNA, enzymes, but also a whole cell. The second component is an electrochemical or optical device that converts the recognition event into a measurable signal (Figure 1).

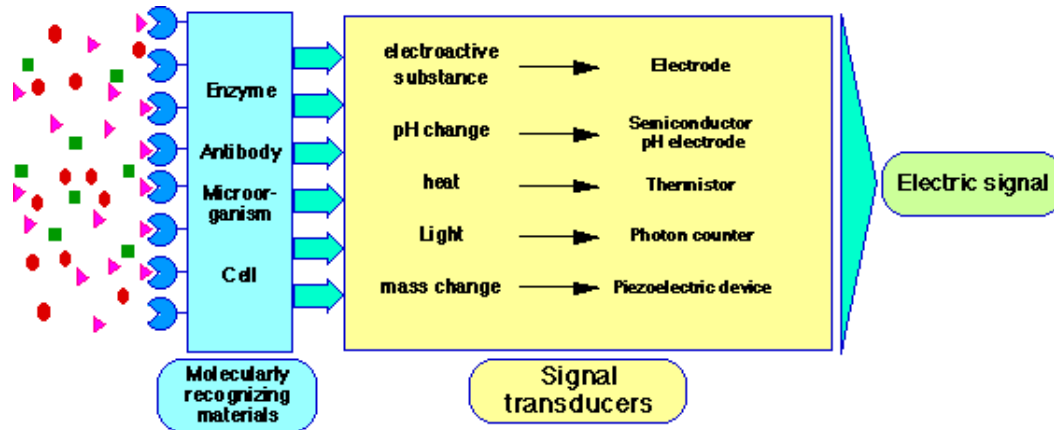


Figure 1. General biosensor scheme.

The outcome is both qualitative and quantitative because while the specificity of the signal is guaranteed by the bioreceptor, the intensity is most often related to the concentration of the analyte. From these considerations, we infer the most important features that a good biosensor should possess:

- I. The bioreceptor must have a very high specificity toward the analyte, a good stability under different experimental conditions, and a good reproducibility;
- II. The transducer must have good properties as either an electron transfer mediator or an optical device, and it should be stable and easily modified or functionalized;
- III. To allow for a fast and easy utilization, the pre-treatment phase should be minimal. It also is important to keep at minimum the number of parameters that could influence the performance of the measurement;
- IV. The output should be accurate, easily understandable, reproducible, free of background noise, and in the range of interest;
- V. It should be cheap and user friendly.

Based on the position of the transducer, there are three main types of biosensors; the products of the reactions diffuse to the transducer causing an electrical signal; the products of the reactions are identified by a mediator that interacts with the transducer to generate the signal; the reaction itself is recognized by the transducer. The transducer can then be classified according to the mechanism of analyte recognition. Electrochemical, optical, and thermal biosensors can be identified based on the type of signal used for gathering information about the analyte.⁵

Electrochemical biosensors can be classified according to the specific electrochemical method employed. A potentiometric biosensor is based on the measurement of variations of the electrode potential with respect to a reference electrode, or the potential difference between two reference electrodes separated by a permeoselective membrane.⁶ An amperometric biosensor measures the current generated by an applied potential between two electrodes.

Optical biosensors are based on surface plasmon resonance, and they have recently received considerable attention owing to their high accuracy and reliability. They measure the different ways by which materials or molecule may interact with the light (absorbance of the light, the reflected light, the light output by a luminescent reaction, etc.). One of the most popular materials used in this field is gold nanoparticles of suitable size.⁷

Thermal (calorimetric) biosensors measure the difference of temperature before and after the reaction. In fact, the majority of the enzymes catalyze exothermic reactions and thus the heat generated can be measured.⁸

1.1.1 Electrochemical Immunosensors

Sensitive quantitative detection of protein biomarkers is critical to many areas of biomedical research and diagnostics, systems biology, and proteomics. Biomarker levels in serum can detect and monitor diseases such as cancer. In this context, sensors need to be simple operationally, capable of rapid multiplexed detection, inexpensive, and must display sufficiently good sensitivity and detection limits to address the levels of the biomarkers in both normal and cancer patient serum.⁹

Conventional ways of measuring proteins include enzyme-linked immunosorbent assays (ELISA), radioimmunoassay (RIA), electrophoretic immunoassay, and mass spectroscopy-based proteomics. These techniques often involve sophisticated instrumentation, significant sample volumes, limited sensitivity and clinically unrealistic expense and time. ELISA-like approaches have been successfully adapted to immunoarrays systems. These ultrasensitive multilayer arrays, relying on optical or electrical detection, have considerable promise for achieving point-of-care measurement.⁹

Immunosensors are biosensors based on the antigen-antibody interaction, which is responsible for eventually generating the actual signal. This type of biosensors has, in principle, high specificity and low limit of detection thanks to the extreme affinity that antibodies have for their antigen. Whereas antibodies are proteins produced by the immune system, antigens can be a variety of different molecules, from protein to DNA, lipids, etc.¹⁰ In the following, we provide a brief description of the structure of antibodies to appreciate better how they work and can be used in biosensors.

Antibodies are heavy globular plasma proteins (150 kDa). They are also called glycoproteins because they are composed by sugar chains and amino acid residues (Figure 2). The basic functional unit of each antibody is an immunoglobulin monomer, but it can be also dimeric, tetrameric or pentameric.¹¹

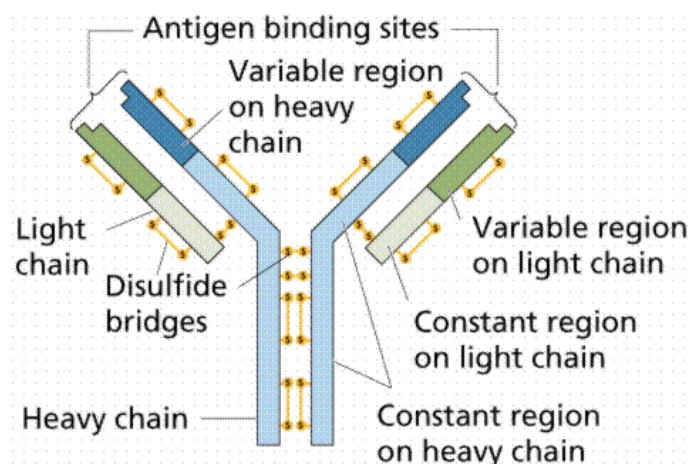


Figure 2. Antibody's structure cell.

The monomer has a “Y” form, which is made of 4 chains: two identical light and two identical heavy chains. These chains are connected by disulfide bonds. Both chains are also divided in two regions: one constant and one variable. The variable regions of both the heavy and of the light chains interact to form the antigen binding site, and thus each monomer has two sites with the same specificity to recognize and link the antigen. The constant region of the heavy chains determines the function of the antibody.¹¹

Immunosensors are most often optical or electrical and therefore antigens and antibodies themselves are not sufficient to generate a sizeable detection signal. For this reason, to permit the transfer of the signal it is necessary to conjugate a label molecule or a material to the first antibody; gold nanoparticles are often used for their particular properties. The chemical groups of the antibody used for conjugations are mainly amine (-NH₂), thiol (-SH), or hydroxyl (-OH) groups.¹²⁻¹³

Of particular relevance to the work carried out during this Laurea Magistrale thesis, which based on electrochemical biosensors, is the presence of a redox enzyme. To increase the electric signal, a secondary antibody (Ab₂) is often added. Its function is to bind both to the analyte protein/s and to the redox enzyme, such as horseradish peroxidase (HRP). Rusling and co-workers found that, there are 14-16 HRP units per secondary antibody.⁹ On the other hand, the same authors found that sensitivity is greatly amplified by using magnetic beads bioconjugated with HRP labels, the number of active HRP per nanoparticle being estimated to be 7500.⁹

1.1.2 Microfluidic Electrochemical Device for High Sensitivity Biosensing

Another aspect relevant to my Thesis concerns microfluidic devices. The latter have the ability to analyze very small quantities of sample, to limit the reagent use, and to carry out analyses at high resolution and sensitivity, low cost, and in short time. Microfluidic devices have applications in biology, chemistry and medicine, including measurement of diffusion coefficient, fluid viscosity, and

binding constant, as well as DNA analysis, cell separation, cell patterning, capillary electrophoresis and immunoassays. Implementing biosensors in microfluidic format provides a potentially more efficient approach to control and automate sample introduction and steps such as washing and reagent addition. By coupling with microfluidics, immunoassay procedures could potentially be made fast enough for point-of-care without sacrificing sensitivity.¹⁴

Microfluidics devices are commonly fabricated in glass, silicon, or polymers, with polymers finding considerable recent attention. Poly(dimethylsiloxane) (PDMS) is used extensively to fabricate these microfluidic devices using photolithography or more simply by polymer deposition onto molds. The work carried out in the Rusling group at the University of Connecticut, and relevant to this Thesis research, relies on an electrochemical sensor constructed by integrating injection-molded electrodes into a polystyrene micro-flow channel.¹⁴ A simple microfluidic device was used for electrochemical biosensing, fabricated by mold deposition and validated by sensitive detection of hydrogen peroxide. The device features a single microfluidic channel made from PDMS coupled to a fixed volume injector, and incorporates a biocatalytic sensing electrode, a reference electrode and a counter-electrode. PDMS was chosen because it is easily moldable, soft and readily integrated with outside components, and effective protocols exist to inhibit biomolecular contamination. Whereas the detection limits of biomarkers in a microfluidic biosensor are usually better than those obtained with a simple rotating-disk electrode in a conventional electrochemical cell, the sensitivity is comparable between the two systems. The improvement of detection limit may be related to a better control of mass transport in the microfluidic system compared to the rotating-disc electrode system, leading to better signal-to-noise.¹⁴

1.1.3 Nanog Protein as Biomarker of Cancer

A few words about the specific biomarker protein used in my Thesis work are necessary. The stem-cell-abundant protein Nanog is highly expressed in undifferentiated embryonic stem (ES) cells and regulates stem-cell differentiation. Nanog is a unique homeobox transcription factor and has a homeodomain with

homology to members of the natural killer gene family; indeed it has a similar critical role in regulating the cell fate of the pluripotent ICM (inner cell mass) during embryonic development, maintaining the pluripotency epiblast and preventing differentiation.¹⁵

This protein may play a role in carcinogenesis of embryonic cancer, gliomas, liver cancer, gastric cancer, and other cancers. The role of Nanog in the transformation of cervical epithelial cells carcinoma, and the occurrence and development of cervical carcinoma have not been investigated in detail. The expression of Nanog in cervical epithelia lesions of varying severity and in cervical carcinoma by immunohistochemical analysis have been addressed.¹⁵ The specimens were obtained from 253 patients: of these 49 had a normal cervical epithelia, 31 had mild dysplasia (CIN I), 77 had moderate-severe-dysplasia (CIN II-III) and 78 had squamous cervical carcinomas (SCC). They found that the expression levels of Nanog were higher in sample from SCC patients than in samples from patients with normal cervical epithelia and CIN; they were also higher in samples from patients with CIN than from those with normal cervical epithelia. Nanog expression levels showed also significant differences according to different tumor sizes (Figure 4).¹⁵

	<i>Nanog</i>					P
	Total N = 235	0 (-) N = 26	1 (+) N = 85	2 (++) N = 76	3 (+++) N = 48	
Normal	49	17	22	8	2	0.000
CIN I	31	2	18	9	2	0.009
CIN II-III	77	4	25	35	13	0.015
SCC	78	3	20	24	31	0.017

Figure 3. Expression of Nanog in cervical epithelial lesions of varying severity:

- 0(-) = < 5% positive cells;
- 1(+) = 5-25% positive cells;
- 2(++) = 26-75% positive cells;
- 3(+++) = more than 76% positive cells.

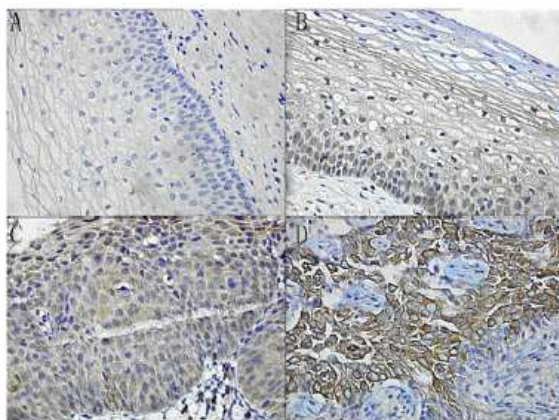


Figure 4. *Nanog* expression and localization in (A) normal cervical epithelial cells; (B) CIN I cells; (C) CIN II-III cells; (D) SCC cells. The distinct brown color indicative of *Nanog* was detected in the cytoplasm of the positive cells.

1.2 Self-Assembled Monolayers (SAMs) as Platforms for Biosensors

The building of biochemical sensors and, particularly, electrochemical biosensors based on the deposition of functionalized layers on solid substrates is gaining increasing importance.¹⁶ Making surfaces that can be used for biosensing involves surface modifications aimed at specifically changing the way they interact with the environment, usually a solution. Biosensors are devised to bind the analyte and transduce the binding event to a sizeable output signal, whether optical or electrochemical, that can be used for quantification. The nature of the surface is of paramount importance to determine the performance of the device or sensor. In electrochemical biosensors, where detection is associated with the onset of a reduction or an oxidation current, the second important ingredient for devising a well-performing system is the efficiency of electron transfer (ET). Understanding and controlling electron conduction through the monolayer (or multilayer) interposed between the underlying conducting substrate and solution species diffusing in proximity of the outer monolayer interphase is indeed essential for transducing the biomolecule recognition into a significantly large

electrochemical current. In recent years, several groups have been studying ET reactions through metal electrode – organic monolayer systems, particularly those based on self-assembled monolayers (SAMs) obtained by spontaneous adsorption of thiolated molecules or disulfides onto gold substrates.^{16b,17} Main factors affecting the ET rate through SAMs are the monolayer thickness, the structure and orbitals of the adsorbed thiols, the presence of ionic or pH-sensitive terminal groups on the solution side, and further factors related to the solution.

1.2.1 Electron Transfer through SAMs

Understanding the mechanisms of ET reactions is a fundamental challenge in a variety of areas of chemistry and biochemistry.¹⁸⁻²¹ Considerable achievements in this direction have been gathered by studying long-range electron or hole transfers in proteins^{20a} and DNA.^{21a} Long-range ET reactions are intrinsically nonadiabatic and may proceed by different mechanisms. One important path for long-range ET is provided by the superexchange mechanism, where the electron tunneling is mediated by the bridge separating the donor and the acceptor but without transient occupation of the bridge electronic states.^{19a,22} The ET rate constant depends on the electronic coupling between the reactant and product states at the transition state and is proportional to $\exp(-\beta d_{DA})$, where d_{DA} is the donor-acceptor distance and β is the exponential factor describing the falloff rate through the specific bridge. Alternatively, the bridge may provide localized or partially delocalized electronic states where electrons may hop by an incoherent mechanism.^{21a,23} Because electron injection into the first bridge unit is the slow step, the ET rate is mildly dependent on the increase of bridge units. Sequential electron hopping may become more efficient than superexchange when the bridge is made sufficiently long. Such a competitive-reaction scheme has received a general consensus for charge transfer across DNA strands,^{21a,23a} but it has not been clearly assessed whether this scheme can be extended to proteins and thus peptides,²⁴ unless suitable amino-acid side-chain groups are present along the peptide chain.²⁵

Long-range ETs have been extensively studied, using freely diffusing donor – molecular bridge – acceptor systems (with either outer-sphere^{19a} or

dissociative-type acceptors²⁶), electrode – molecular bridge – electrode junctions,²⁷ and electrode – SAM – redox moiety, where the latter (e.g., a ferrocenyl group or a redox protein) is covalently or electrostatically bounded to the solution side of the SAM's adsorbate/s.^{17a,17b,17e,28-32} The distance dependence of the ET rate and thus the observed β factor depend on the actual molecule forming the monolayer and thus the nature of the bonds of the bridge separating donor and acceptor. With alkanethiol ferrocene-terminated SAMs, where only saturated C-C bonds are present, the dependence is exponential, in agreement with the superexchange mechanism.²⁸ On the other hand, different outcomes have been reported for peptide SAMs decorated by ferrocene moieties. Whereas some peptide SAMs display a simple exponential dependence, though with β values remarkably smaller than for hydrocarbon chains, there are reports of the observation of very mild distance dependences of the ET rate ($\beta < 0.1 \text{ \AA}^{-1}$) that were interpreted as due to a hopping ET mechanism or to the dynamics of the of α - or β -amino acid peptide chain.^{29,30a,33}

The number of ET studies based on the determination of ET rate constants between SAM-modified electrodes and freely diffusing solution species is more limited^{31a,34-39} and, in fact, no study has been yet reported for peptide SAMs. Indeed, the use of soluble redox probes is often employed to test how tight and blocking is a given SAM. Generally, the use of solution redox probes is affected by problems in assessing and controlling the quality and packing of the SAMs (see below), which implies a possible penetration of the redox species through the SAM defects and thus an apparent increase of the ET rate. The effect of having charges on the SAM periphery or different pH values and electrolytes is solution has been addressed. Electrostatic repulsion between charged head groups in the outer monolayer periphery and charged probes influences the ET rate quite significantly. For example, alkanethiols with positive terminal functionalized groups and self-assembled on gold can block ET between the substrate and a positively charged electroactive species dissolved in the electrolyte solution.⁴⁰ Most studies, however, have been carried out with uncharged monolayers and constant solvent/electrolyte conditions, and thus imply no coulombic corrections in the definition of the ET rate constant.

Beside intrinsic factors directly related to the chemical nature of the molecules forming the SAM, there are important issues concerning the dynamics of the SAM⁴¹ and the quality of the latter. Indeed, although making SAMs involves relatively simple chemistry, the resulting modified surfaces are affected by heterogeneity in coverage and this may affect signal transduction in electrochemical sensors. For example, by using a fluorescence-microscopy electrochemical method, Bizzotto and co-workers studied the potential-dependent desorption of alkanethiolate and DNA SAMs on gold surfaces, and concluded that heterogeneity in surface coverage may be stronger than expected.⁴² Indeed, the main reason why long-range ET through SAMs has been studied mostly by using redox groups linked to the end of the monolayer adsorbate is that this strategy helps minimizing the problem of defects, as the presence of the latter should not affect (at least for sufficiently well-packed SAMs) the main electron tunneling pathway, i.e., through bonds. On the other hand, transduction in sensors involves detection of redox species dissolved in solution and thus a preliminary screening of the ET mediating property of a given SAM needs to be based on the observation of the electrochemical behavior of a freely diffusing redox probe. ET occurs by electron tunneling through the SAM but also through pinholes and other defects. The observed ET rate constant is thus generally the result of a combination of contributions and discerning between them is a difficult task.^{34,43,44}

1.2.2 Self-Assembled Monolayer

SAM form from spontaneous adsorption of a molecular layer onto a substrate. Bare surfaces of metals and metal oxides tend to accidentally adsorb organic materials readily because these adsorbates lower the free energy of the interface between the metal or metal oxide and the environment. These adsorbates also alter interfacial properties and can have a significant influence on the stability of nanostructures of metals and metal oxides. The organic material can act as a physical or electrostatic barrier against aggregation, decreasing the reactivity of the surface atoms, or act as an electrically insulating film. Surfaces coated with these materials, however, are not well defined as do not present specific chemical

functionalities and do not have reproducible physical properties (e.g., conductivity, wettability, or corrosion resistance). Nevertheless, SAMs provide a convenient, flexible, and simple system with which to tailor the interfacial properties of metals, metal oxides, and semiconductors.⁴⁵⁻⁵⁵

SAMs form by the adsorption of molecular constituents from solution or gas phase onto the surface of solids. The adsorbates organize spontaneously into crystalline or semicrystalline structures.⁵⁶ The molecules (or ligands) that form SAMs have a chemical functionality, or “head group”, with a specific affinity for a substrate. There are a number of head groups that bind to specific metals, metal oxides, and semiconductors, but the most extensively studied class of SAMs is derived from the adsorption of alkanthiols on gold. The high affinity of thiols for the surfaces of noble and coinage metals makes it possible to generate well-defined organic surfaces with useful and highly alterable chemical functionalities displayed at the exposed interface. SAMs are therefore nanostructures with a number of useful properties. The composition of the molecular components of the SAM determines the atomic composition of the SAM covering the surface. This characteristic makes it possible to use organic synthesis to tailor organic and organometallic structures at the surface with positional control approaching ~0.1 nm. SAMs can be fabricated into patterns having 10-100 nm scale dimensions parallel to the surface. SAMs are well-suited for studies in nanoscience and technology because of the following characteristics:

- 1) They are easy to prepare, that is, they do not require ultrahigh vacuum (UHV) or other specialized equipment (e.g. Langmuir-Blodgett (LB) troughs) in their preparation.

- 2) They form on objects of all sizes and are critical components for stabilizing and adding function to preformed, nanometer-scale objects (for example, thin films, nanowires, colloids, and other nanostructures, they are also suitable for biomolecules immobilization).

- 3) They can couple the external environment to the electronic (current-voltage responses, electrochemistry) and optical (local refractive index, surface plasmon frequency) properties of metallic structures.

- 4) They link molecular-level structures to macroscopic interfacial phenomena, such as wetting, adhesion, and friction.

5) Flexibility to design the head group of SAM with various functional groups in order to accomplish hydrophobic or hydrophilic surface as per the requirements.

6) Ability to unravel molecular level information about phenomena such as protein adsorption, DNA hybridization, antigen-antibody interaction etc. using surface sensitive techniques such as scanning probe microscopies.⁵

1.2.3 Types of Substrates and Characterization of SAMs

The substrate is the surface on which a SAM forms. Types of substrates range from planar surfaces (glass or silicon wafers supporting thin films of metal, metal foils, single crystals) to highly curved nanostructures (colloids, nanocrystals, nanorods). Planar substrates are widely used for characterizing the structure-property relationships of SAMs because they are easy to prepare and compatible with a number of techniques for surface analysis and physicochemical characterization such as cyclic voltammetry, scanning probe microscopies, infrared reflectance absorption spectroscopy (IRRAS), Raman spectroscopy, X-ray photoelectron spectroscopy (XPS), near edge X-ray absorption fine structure spectroscopy, contact angle goniometry, optical ellipsometry, surface plasmon resonance spectroscopy, and mass spectrometry. Other metallic nanostructures, such as nanoparticles, can also support SAMs, and these systems can be characterized by many other techniques.

The structures of SAMs and the mechanisms by which they assemble are topics that have evolved considerably over the past two decades, particularly because there have been substantial advances made in methods suitable for characterizing them. The development of scanning probe microscopies provided powerful new capacities to study both the structural organization of SAMs and the assembly process at a molecular level. These techniques have greatly extended the initial structural understandings derived mainly from spectroscopic techniques (IRRAS, XPS, ellipsometry, etc.) and physical methods (principally studies of wetting). The extensive literature on SAMs has established a common point of view that SAMs naturally exhibit a high degree of structural order after assembly and, therefore, form well-defined phases of organic groups organized in precisely

understood lateral organizations on the underlying substrate. In fact, SAMs are dynamic materials that include significant forms of structural complexities, especially when immersed in fluids. As a rule, SAMs embed intrinsic and extrinsic defects because they adopt adsorbed structures that are directed by the thermodynamics of a reasonably complex chemisorption process.

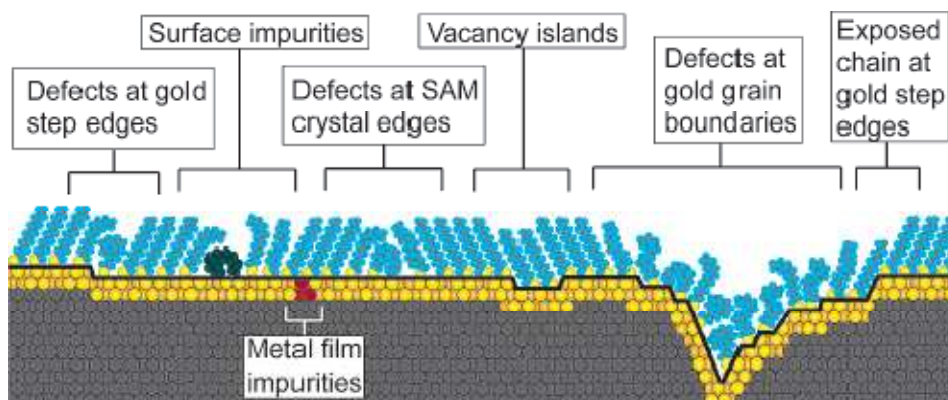


Figure 5. Schematic illustration of some of the intrinsic and extrinsic defects found in SAMs formed on polycrystalline substrates.

The cartoon of Figure 5 shows how SAMs can be substantially more complex than the highly ordered arrangements that are commonly assumed. The causes of defects in SAMs are both intrinsic and extrinsic. Examples of external factors include cleanliness of the substrate, the methods for preparing the substrate and the purity of the solution of adsorbate. On the other hand, these defects can be eliminated by proper control of the experimental conditions. Examples of intrinsic factors are the many structural defects that the substrate has itself and the complex phase behaviors due to the dynamic system of the SAMs. These defects can be minimized but never completely eliminated.

The assembly process involves a thermodynamic equilibrium between adsorbates on the surface and their precursors free in solution. Although these SAMs may be kinetically stable in the absence of a flux of adsorbate, the high coverage of the adsorbate present in the SAM is, in fact, thermodynamically unstable. Only in a case where the rate of desorption is rigorously zero would the SAM be expected to exist for an indeterminate period outside the solution used to prepare it.

1.2.4 Nature of the Metal-SAM Interface

Most SAMs of practical interest are formed at reactive interfaces. The adsorbate and the substrate are both transformed to some degree by the reactions that lead to the formation of the SAM itself. The chemistry involved for the chemisorption of thiols on gold is in principle the most straightforward, but it probably remains as the most enigmatic. Because gold does not form a surface oxide (as, for example, does silver), the formation of SAMs from thiols is not complicated by chemistry that might be required to displace or reduce surface oxides. On the other hand the details regarding the nature of the metal-sulfur bond and the spatial arrangement of the sulfur groups on the underlying gold lattice are still controversial.

The formation of a thiolate requires the chemical activation of the S-H bond of the thiol (or the S-S bond of the disulfide). It is established that the adsorption of dimethyl disulfide on Au(111) occurs dissociatively.⁵⁷ The reaction is reversible, and recombinative desorption of the disulfide is an activated process with a barrier of ca. 30 kcal/mol. This energy suggests that a fairly significant degree of charge transfer to sulfur must occur in the thiolates.⁵⁸ Of particular interest was the estimation that the barrier for the bimolecular recombinative desorption of an alkanethiolate from a SAM on gold in the form of a dialkyl disulfide is ~15 kcal/mol.⁵⁹ This value is approximately a factor of 2 less than that deduced in the gas-phase studies. We note here, though, that the two energies are not directly comparable given that one also contains contributions from the heats of dissolution of the adsorbate as well as the heat of immersion of the substrate in the solvent. In this context, the range of reported values appears to be one that follows directly from the different forms of the measurements used to assess the strength of the Au-S bonding interaction. As the vacuum measurements are most easily interpreted, it is reasonable to conclude that the Au-S bond that anchors the SAM is, in fact, a reasonably strong one (a homolytic Au-S bond strength on the order of ca. -50 kcal/mol) based on the known S-S homolytic bond strength of a typical dialkyl disulfide (~62 kcal/mol).⁶⁰

The fate of the hydrogen of the S-H groups still has not been determined unambiguously. It seems probable that adsorption in a vacuum leads to loss of the

hydrogen in the form of molecular hydrogen. The reductive elimination of H₂ from Au(111) is a weakly activated process. In aqueous solution, another possibility exists. If the thiol hydrogen is not lost in the form of H₂, the presence of oxygen in the reaction medium might also lead to its oxidative conversion to water. In either case, the Au-S bonding interaction in the thiolate is sufficient to retain the chains at the surface in a durable fashion and preclude a recombinative desorption of a disulfide product at room temperature.

The central bonding habit of the high-coverage alkanethiol phases on Au(111) is generally accepted to be based on a $(\sqrt{3}\times\sqrt{3})R30^\circ$ overlayer (R=rotated).⁶¹⁻⁷⁵ Figure 6 shows this structure schematically. The SAMs formed by *n*-alkanethiols are usually described as simple thiolate adlayers (chemisorbed structures formed by the activation of the S-H bond at the gold surface).⁶⁶⁻⁶⁷ Within this model there has been considerable discussion of the surface sites involved in this bonding. Most studies of SAMs on gold have employed substrates presenting a strong (111) texture to support the monolayer. Other studies have been directed at different crystallographic textures, although the structural literature available in these cases is far more limited.^{65,68}

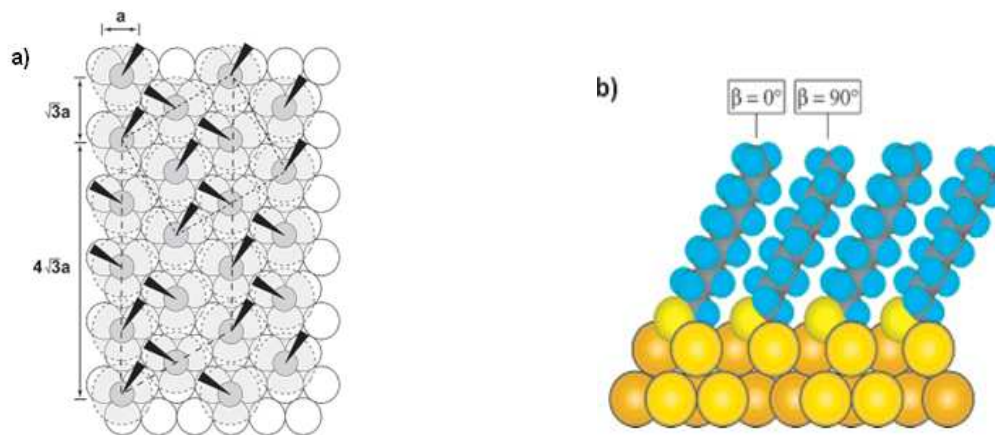


Figure 6. Schematic diagram depicting the arrangement of decanethiolates on Au(111) lattice when maximum coverage of the thiolates is attained. (a) The arrangement shows a $(\sqrt{3}\times\sqrt{3})R30^\circ$ structure where the sulfur atoms (dark gray circles) are positioned in the 3-fold hollows of the gold lattice (white circles). The light gray circles with the dashed lines indicate the approximate projected surface area occupied by each alkane chain; the dark wedges indicate the projection of the CCC plane of the alkane chain onto the surface. The alkane chains tilt in the direction of their next-nearest neighbors; (b) Cross-section of the SAM.

1.2.5 Organization of the Organic Layer

The geometric arrangement of the sulfur moieties on the surface and the nearest-neighbor distances between the metal atoms at the surface are factors that determine the upper limit on the density of molecules on the surface. This two-dimensional density of molecules may not correspond, however, to the density that the same molecules could attain in a crystalline form. The arrangement of molecules that is dictated by the placement of the sulfur moieties on the surface may not maximize the lateral interactions between the organic components of the SAMs. To minimize the free energy of the organic layer, the molecules adopt conformations that allow high degrees of Van der Waals interactions and, for some molecules such as peptides, hydrogen bonds with the neighboring molecules; these arrangements yield a secondary level of organization in the monolayer that is important in determining macroscopic materials properties, such as wetting and conductivity of the SAMs.

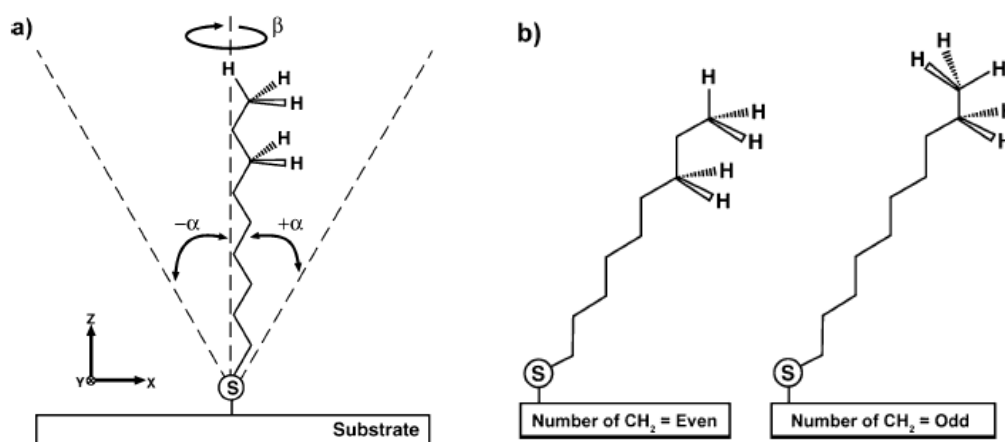


Figure 7. a) Schematic view of an all-trans conformer of a single, long-chain alkanethiolate adsorbed on a surface. The tilt angle (α) is defined with respect to the surface normal direction. The twist angle (β) describes the rotation of the CCC bond plane relative to the plane of the surface normal and the tilted chain; b) Schematic views of single, long-chain alkanethiolates (with even and odd numbers of methylene groups) adsorbed on gold. The conserved value of α for each produces different projections of the terminal methyl group on the surface.

A simple single-chain model is sufficient to facilitate comparisons of the organization adopted by different organosulfur compounds with (mostly) linear conformations on different types of substrates (Figure 7a). Two parameters describe the variations in the orientation of the organic molecules in the SAM: the angle of tilt for the linear backbone of the molecule away from the surface normal (α) and the angle of rotation about the long axis of the molecule (β). As defined in Figure 7, α can assume both positive and negative values; values of β range from 0° to 90° . For SAMs formed from *n*-alkanethiols on gold, palladium, silver, copper, mercury, platinum, and other metals, the alkane chains adopt a quasi-crystalline structure where the chains are fully extended in a nearly all-trans conformation. The tilts of these chains vary for the various metals: the largest tilts (α , with an absolute value near 30°) are found on gold, while the structures most highly oriented along the surface normal direction arise on silver ($\alpha \sim 10^\circ$) and mercury ($\alpha \sim 0^\circ$). The average β for gold lies near 50° , while for other metals, the data, where available, indicates values generally clustered near 45° . These data are consistent with space-filling models involving (at least for the case of gold) chain tilts lying along the direction of the next-nearest neighbor, i.e., an ordered structure involving a hexagonal arrangement of the sulfur atoms. These assumptions have been confirmed by the results of diffraction studies.^{69,70}

Not all thiolated molecules adopt the same orientations as *n*-alkanethiols. For cases where the steric requirements of the adsorbate preclude the ordering found for the *n*-alkanethiolate structures, evidence of other organizations has been detected. The values of α for SAMs formed by *n*-alkanethiols on Au(111) appear to be unique. The tilt of the chain projects an orientation of the average chain in which the sign of the tilt angle is conserved regardless of the number of carbons in the alkane chain. All available data suggest that the structures exhibited by thiolate SAMs on gold adopt a value of $\alpha \sim +30^\circ$. This feature of the assembly leads to very different surface projections of the methyl groups for SAMs with odd and even numbers of methylene groups (Figure 7b) and correlates strongly with the unique wetting behaviors of SAMs on gold; SAMs of thiolates with an odd number of methylene groups produce surfaces whose free energies are systematically slightly larger than those with an even number of methylenes.

1.3 Gold in Electrochemical Biosensors

There are five characteristics of gold that make it a good choice as a substrate for studying SAMs. First, gold is easy to obtain, both as a thin film and as a colloid. It is straightforward to prepare thin films of gold by physical vapor deposition, sputtering, or electrodeposition. Although expensive and not essential to most studies of SAMs, single crystals are available commercially. Second, gold is exceptionally easy to pattern by a combination of lithographic tools (photolithography, micromachining, etc.) and chemical etchants. Third, gold is a reasonably inert metal: it does not oxidize at temperatures below its melting point; it does not react with atmospheric O₂ and it does not react with most chemicals. These properties make it possible to handle and manipulate samples under atmospheric conditions instead of under UHV. Gold binds thiols with high affinity, and it does not undergo any unusual reactions with them. Fourth, thin films of gold are common substrates used for a number of existing spectroscopies and other analytical techniques. This characteristic is particularly useful for applications of SAMs as interfaces for studies in biology. Fifth, gold is compatible with cells. SAMs formed from thiols on gold are stable for periods of days to weeks when in contact with the complex liquid media required for cell studies.

The properties of gold nanoparticles (AuNPs), such as light absorption and their excellent electroactivity, are bringing interesting immunosensing alternatives. Particular emphasis is given to the different optical⁷¹ and electrochemical^{72,73} detection methodologies where NPs show significant impact. In certain cases, assays based on nanomaterials have offered significant advantages over conventional diagnostic systems with regard to assay sensitivity, selectivity, and practicality.⁷⁴ AuNPs are so small that they exhibit characteristics that are often not observed in the bulk materials. This is due to the quantum size effect that leads to unique optical, electronic, and catalytic properties.⁷⁵ AuNPs are also fully compatible with biomolecules, when decorated with thin organic coatings. This has resulted in their use in sensors for DNA, proteins, organic analytes, and metal ion. The use of thiol groups for their functionalization is a good way to control the direction of the bond between the

label and the biomolecule. NPs' involvement in DNA, protein and even cell sensing systems, have recently been the most important topics in nanobiotechnology.⁷⁵

The electroactivity of AuNPs allows the use of both electrical and electrochemical techniques for their detection, which allowed to detect low concentrations of proteins.⁷⁶ NPs can be directly detected due to their own redox properties or indirectly due to their electrocatalytic properties toward other species, such as silver ion reduction.

It is also worth mentioning that their large surface coupled with an easy bioconjugation make NPs excellent carriers of other electroactive labels in immunoassay.⁷⁵ Nanoscale structures of AuNPs on conductive surface combined with high electrical conductivity can facilitate fast ET to and from redox enzymes, for examples horseradish peroxidase, providing a sensitive platform for biosensors. AuNPs have been employed as nanoelectrode relay units transporting electrons efficiently and activating enzyme bioelectrocatalysis.⁹ The introduction of NPs into the traducing platform is commonly achieved by their adsorption onto conventional electrode surfaces in various forms, including that of a composite.⁷⁵

To summarize, modified AuNPs electrodes have very large surface areas, are simple to fabricate and functionalized, retain metallic conductivity, and have facile biomolecule attachment.⁹

1.4 α -Aminoisobutyric Acid 3_{10} -Helices as Adsorbate for SAMs

The nature, stability and, for electrochemical biosensors, the electron transfer properties of the SAM are of paramount importance to determine the performance of a device or sensor. A question now arises: which are the molecules of choice to make robust and performing SAM-based electrochemical devices? SAMs should be sufficiently chemically and electrochemically stable, well organized, and based on easily tunable molecules. The latter aspect includes the ease by which the length (which implies modulating the SAM thickness) and functionalization (with suitable groups on the molecule end facing the solution) of

the thiolated molecule can be controlled. The presence of further specific structural features is also useful, such as the presence of intermolecular hydrogen bonds between adsorbate molecules (such as C=O...H-N hydrogen-bonds between embedded amide groups) which increases the SAM robustness. The molecules that conveniently collect all these features, including their particular compatibility with biomolecules, are peptides. The following question now is: among all possible systems, which peptides are likely to provide particularly suitable systems?

In this Thesis research, we also describe some self-assembly features of thiolated α -aminoisobutyric (Aib) acid homooligomers on activated Au surfaces. There are several reasons for considering these peptides as good candidates. Aib is characterized by marked hindrance at the α -carbon and restricted torsional freedom (Figure 8).^{77,78}

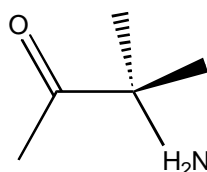


Figure 8. α -Aminoisobutyric Acid.

Owing to these features and differently from peptides based on coded α -amino acids which form stable helices only for rather long oligomers,⁷⁹

Aib peptides adopt a 3_{10} -helical structure and are rigid even when short.⁸⁰ Rigidity is ensured by a strong framework of intramolecular C=O...H-N hydrogen bonds that causes C=O and N-H groups to align significantly along the peptide axis⁸¹ and, therefore, a strong oriented dipole moment arises.

In 3_{10} -helices, each intramolecular C=O...H-N hydrogen bond involves residues i and $i + 3$, a single helical turn requires 3.24 amino acid residues, the peptide length increases by 1.94 Å/residue and thus addition of a single coil increases the peptide length by 6.29 Å.⁷⁸ The 3_{10} -helix is thus more elongated and thinner than the α -helix, which typically involves 3.63 residue/coil and a vertical pitch of 1.56 Å/residue. In Figure 9 and in Table 1 we compare different properties of the two helices. As opposed to simple alkanethiols where an increase in the number of units increases molecular flexibility, Aib peptides become even

stiffer as the number of residues, and thus of intramolecular hydrogen bonds, increases. 3_{10} -helices become more tightly wound as they become longer due to the shortening of the H-bonds that accompanies the stronger cooperative interactions.^{81c}

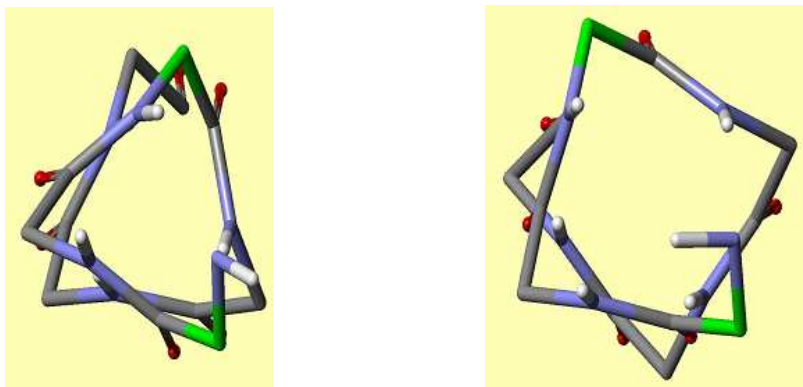


Figure 9. Section of 3_{10} -helix (on the left) and section of α -helix (on the right).

Table 1: Average parameters for right-handed 3_{10} and α -helices.

Parameters:	3_{10} -Helix	α -Helix
Φ	57°	63°
Ψ	30°	42°
N \cdots O=C H-bond angle	128°	156°
Rotation (per residue)	111°	99°
Axial translation (per residue)	1.94Å	1.56Å
Residues per turn	3.24	3.63
Pitch	6.29Å	5.67Å

In addition and as opposed to simple alkanethiols for which the increase in the number of methylene groups increases the flexibility of ligands, the key motif of Aib peptides is the increase of the peptide stiffness with the number of residues and thus of hydrogen bonds. This feature and the unique rigidity of short Aib homopeptides are being successfully exploited as spacers or templates in electrochemical and spectroscopic investigations, also because of the excellent electronic communication provided by the peculiar backbone stiffness. Since 2D (and 3D SAM, such as in monolayer protected clusters (MPCs)) formation already

causes the conformational freedom of alkanethiols to decrease dramatically, Aib peptides are expected to behave as even more rigid adsorbates.

The 3_{10} -helix helical structure is stable both in the solid state and in solution.^{78,80,82} It is also kept unaltered when thiolated Aib peptides are self-assembled on 1-2 nm gold nanoclusters.⁸³ With nanoparticles, compelling evidence showed that these peptides also form interchain hydrogen bonds, resulting in the formation of strong molecular networks. Insights into this experimental observation were obtained by a multilevel molecular modeling study.⁸⁴ A previous analysis of the amide I and amide II regions of IRRAS spectra of thiolated Aib hexapeptide SAMs on extended gold surfaces also pointed to the presence of helices.⁸⁵

The Maran group has previously studied ET reactions across Aib homooligopeptides using donor-peptide-acceptor systems in solution.⁸⁶ Evidence was obtained for a mild distance dependence of the ET rate and even an increase of the rate at a certain peptide length. This outcome was rationalized by considering that while addition of a new α -amino acid unit increases the donor-acceptor distance, it also introduces new intramolecular hydrogen bonds that act as efficient ET shortcuts, thereby counteracting the usually observed exponential drop of the ET rate with distance. Theoretical studies supported the general features of this experimental finding.⁸⁷ These results suggested us that Aib peptides may indeed furnish ideal molecular bridges for making robust SAMs (molecular rigidity, interchain network) for electrochemical biosensing and other nanobiotechnological applications. Based on the outcome of the solution studies, efficient electron conduction through Aib-peptide SAMs was conceivably expected, with useful consequences for detection of analytes through observation of high redox currents when the SAM is the central part of a transducing electrochemical platform. Very recently some thiolated Aib-peptides on mercury electrodes and found that tight SAMs form.⁸⁸ Although the main target of that study was to estimate the surface dipole potential of the Aib-peptide SAMs, it was also observed that the kinetics of the voltammetric reduction of Eu(III) was not severely slowed by the presence of the peptide film: this also concurred to suggest that Aib chains may mediate electron tunneling very efficiently. For peptides thiolated on the nitrogen terminus, where the negative pole of the peptide dipole is

located, it was observed that the negatively polarized electrode produces an interfacial electric field liable of orienting the peptide dipole even against its “natural” dipole moment.

Very recently, a study coupled to this Thesis work specifically addressed the issue of determining the ET rate-constant falloff with distance using a series of Aib-peptide SAMs on gold surfaces.⁸⁹ The peptides were devised to give rise from zero to five C=O•••H-N intramolecular hydrogen bonds. The peptides were thiolated on the positive end of the molecular dipole. The standard heterogeneous ET rate constants for the chemically-reversible reduction of a soluble redox probe, Ru(NH₃)₆Cl₃, were determined by CV in 0.5 M KCl aqueous solution. It was shown that once experimental procedures and surface packing are controlled it is indeed possible to carry out accurate studies of the distance dependence of ET through SAMs even when using soluble redox probes. Figure 10 shows the distance dependence of the ET rate. The values show that the ET rate constant initially decreases as the peptide length increases but then displays a remarkably shallow dependence for sufficiently long peptides, the exponential-decay factor (from 3+ to 5+) being of only 0.08 Å⁻¹. These results show that Aib peptides are indeed very good mediators of electron tunneling and thus emerge as remarkably good candidates to make SAMs for electrochemical biosensors.

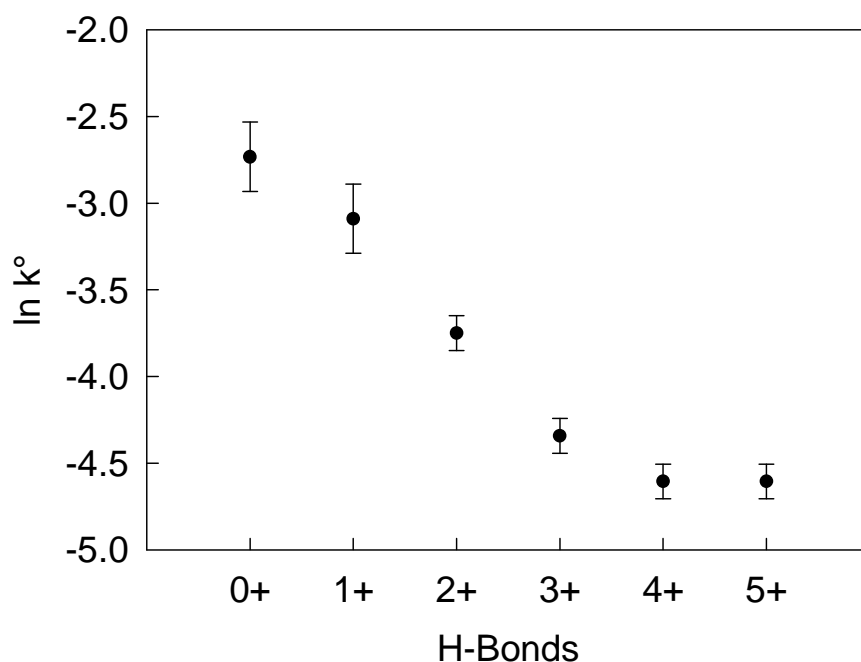


Figure 10. Calculated values of k° against the number of hydrogen bonds.

1.4.1 Characteristics of the Investigated Aib-Homopeptides

Two series of peptides were synthesized, differing in the direction of the dipole moment: a *plus* series with the positive pole of the dipole moment oriented toward sulfur and a *minus* series where the dipole moment is reversed. The name of each peptide is given as composed by a number, which refers to the number of intramolecular hydrogen bonds, and a plus or minus sign, which refers to the orientation of the dipole moment.

Figure 11 shows the primary and secondary structure of peptide **5+**. This peptide is used in the following discussion to explain the general design of our systems. The head of our system is represented by the –SH. This group allows the peptide to be attached to the gold surface. Between sulfur and the α -amino acid chain there is a –CH₂–CH₂– spacer meant to facilitate the coordination to the surface, which otherwise would be hindered by the strong steric hindrance of the 3_{10} -helix. On the other terminus, there is a *t*-butyl group. Figures 11a and 11b help to understand better the orientation of the dipole. The helicity of the system infers a particular orientation to the Aib residues, orienting all C=O groups toward the C terminus and all N-H groups toward sulfur. Accordingly, the dipole moment (in the *plus* series) has the plus pole by the thiol group. Table 2 shows the primary structures for all the peptides belonging to the *plus* series.

For the *minus* series three peptides were synthesized (**1-**, **3-** and **5-**), to investigate the effect of reversing the dipole moment and to compare the results with the *plus* series, which is our reference series. In the *minus* series the characteristics of the design are the same, but while the SH group is now attached to the C terminus that now becomes the head of the peptide, the *t*-butyl group is on the other terminus that becomes the tail. Figure 12 shows the primary (a) and secondary structure (b) of **5-**. From the 3D structure we can notice that the C=O groups are now oriented toward SH, while the NH groups are oriented toward the tail of the peptide. Consequently, the negative pole of the dipole moment is by the thiol group. Table 3 shows the primary structures for all the peptides belonging to the *minus* series.

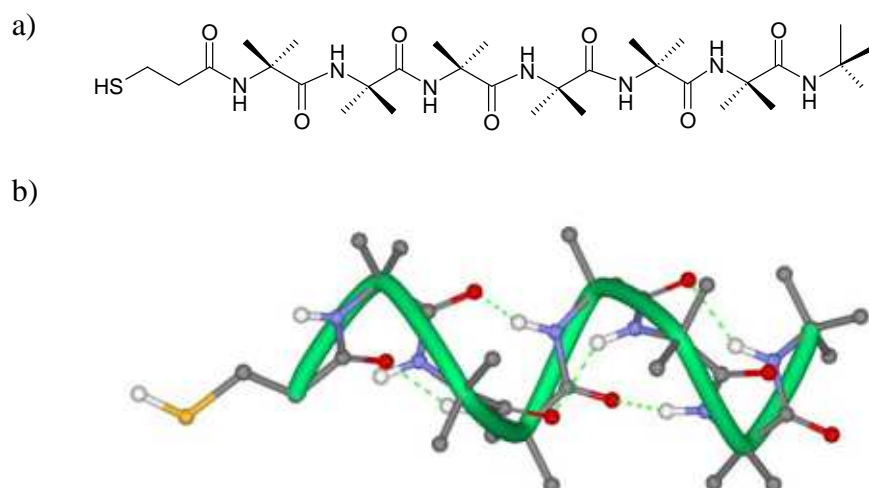


Figure 11. a) Primary structure of the peptide. b) Secondary structure of the peptide.

Table 2: Primary structure of the investigated peptides for the plus series.

<i>Plus Series</i>	
Primary structure	Name
	0+
	1+
	2+
	3+
	4+
	5+

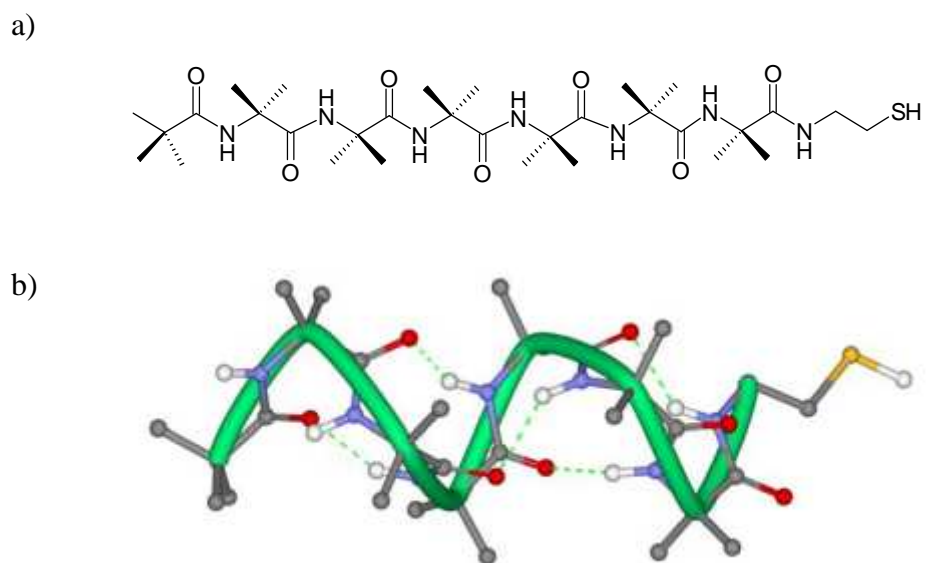
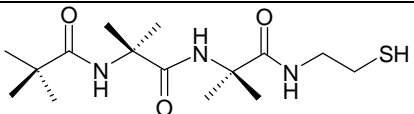
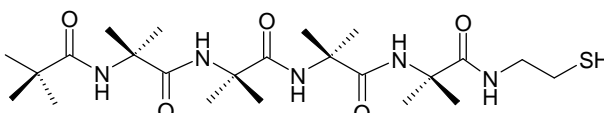
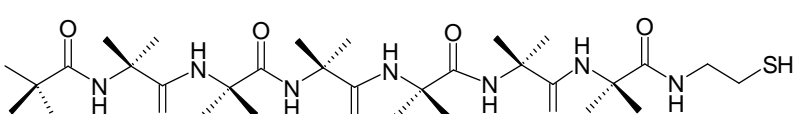


Figure 12. a) Primary structure of the peptide. b) Secondary structure of the peptide.

Table 3: Primary structure of the investigated peptides for the minus series.

<i>Minus Series</i>	
Primary structure	Name
	1-
	3-
	5-

1.5 Purposes of the Thesis

This Thesis concerns the development of a very efficient immunosensor electrochemical device for detecting cancer biomarker proteins, and possible ways to improve its efficiency by modifying parts of the system that are relevant to improve stability and ET through the modified electrode surface.

For the part concerning the study of the ultrasensitive electrochemical immunosensor (Figure 13) for early cancer biomarkers detection, I worked with the research group of Prof. James F. Rusling (Department of Chemistry, University of Connecticut, Storrs, CT, USA). The research associated with the study of the stability and structure of Aib-peptide self-assembled monolayers to be used for improving the sensor performance was carried out in the group of Prof. Flavio Maran. The two topics are related because these peptides will be used to anchor the antibody onto AuNPs. This, however, is an aspect that for time limitations could not be covered during my Thesis work. Details on the Thesis scope and structure are as follows.

We focused our attention on Nanog detection. Nanog is a protein that may be involved in carcinogenesis of cervix and progression of cervical carcinoma. Nowadays, the researchers still do not know the detection limit of this biomarker and the difference of concentration between healthy individuals and patients with cancer. Therefore, we aimed at making an electrochemical sensor capable of displaying very high-sensitivity immunoarrays and low detection limit. Sensors were prepared and, particularly, several conditions to make Nanog-based electrodes were essayed. Eventually, we could optimize the conditions and obtain a nice calibration plot (Amperometric current versus Nanog concentration). Most of the initial work was carried out using the sample handling technology, but then we integrated the system into a microfluidic device, the goal being to automate the method as much as possible.

To improve the efficiency, we are about to further optimize the immunosensor by changing some elements of the transducer, particularly by using a SAM formed by peptides allowing very fast ET (see below) and by increasing

the active superficial area thanks to nanostructured gold electrodes as an alternative to a bed of AuNPs.

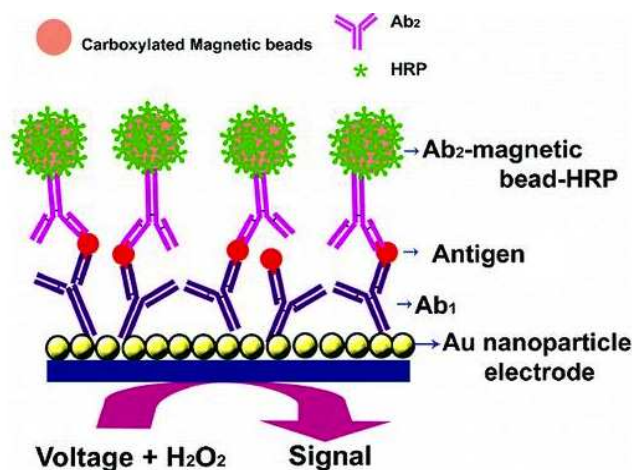


Figure 13. AuNP immunosensor with Ab_1 attached that has captured an antigen from a sample after treating with Ab_2 -magnetic-bead-HRP providing multiple enzyme labels for each Nanog. The detection step involves immersing the sensor into buffer containing mediator, applying voltage, and injecting H_2O_2 .

We carried out an investigation of related issues by using SAMs formed with thiolated Aib peptides of different lengths. The effect of the orientation of the peptide dipole moment was studied by attaching the thiolated moiety to either the nitrogen or carbon terminus. The stability and conformational properties of such SAMs were assessed by an extensive IRRAS investigation, in comparison with the IR absorption spectroscopy of the free peptides. This study showed that in these SAMs Aib peptides form 3_{10} -helices, form interchain $C=O \cdots H-N$ hydrogen bonds, and pack tightly, the surface coverage depending on both the peptide length and orientation. We also found that short peptides may undergo helix disruption, with formation of structures where the number of inter-chain interactions increases. The results nicely supported what recently found concerning the chemical and electrochemical stability of these SAMs as well as the efficiency of ET through them. Main outcome of this study is that we now know which peptides should provide the best transducer substrate supporting the actual Nanog-sensor architecture.

2. Experimental

2.1 Chemicals

Immunosensor. Polydiallyldimethylammonium chloride (PDDA), L-gluthathione reduced (99%), gold (III) chloride trihydrate (99.9%), 2,2'-azino-bis(3-ethylbenzthiazoline-6-sulfonic acid), horseradish peroxidase (HRP, MW 44000), 1-ethyl-3-(3-dimethylaminopropyl) carbodiimide (EDC), N-hydroxysulfosuccinimide ester (NHSS) and Lyophilized 99% bovine serum albumin (BSA), and $\text{Ru}(\text{NH}_3)_6\text{Cl}_3$ (98%) were purchased from Sigma-Aldrich. The primary antibody (Ab_1), the secondary antibody (Biotin- Ab_2), and the Nanog antigen were obtained from Dr. Dharamainder Chaudary UCONN Health Center (Farmington, CT). Immunoreagents were dissolved in a pH 7.0 phosphate saline (PBS) buffer (0.01 M in phosphate, 0.14M NaCl, 2.7mM KCl). Carboxyl functionalized magnetic beads were obtain from Polysciences, Inc. The poly(dimethoxy)silane (PDMS) kit was from Dow Corning. Hydroquinone (HQ) and hydrogen peroxidase (H_2O_2 , 30%) were from Fisher. Water was deionized.

SAMs. Ethanol (HPLC grade, $\geq 99.8\%$), hydrogen peroxide 30%, and sodium hydroxide monohydrate ($\geq 99.9995\%$) were purchased from Fluka. Sulfuric acid 98% (Aristar Grade) was purchased from BDH. Low conductivity water was Water pro analysis obtained from Merck.

2.2 Preparation of HRP single electrodes

The steps to fabricate the immunosensor platform on a single electrode are:

1. Absorption of a layer of cationic polydiallyldimethylammonium (PDDA) from aqueous solution onto a pyrolytic graphite (PG) disk electrode. We used a 20 μL solution of PDDA, for 25 min.



2. The electrode was washed with H₂O and the water removed by shaking the electrodes.

3. 20 μL of a diluted (1:5) solution of 2 mg/mL glutathione-decorated gold nanoparticles [GSH-AuNP] in HPES buffer (pH = 8), were poured onto the PDDA-modified electrode, utilizing the standard layer-by-layer alternate electrostatic adsorption approach⁹⁰ to form a dense layer with organic functionality for capture antibody attachment. Incubation required 25 min.



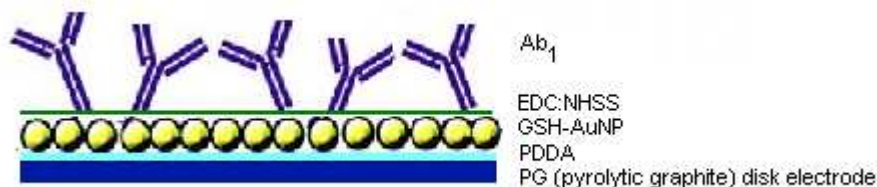
4. The sensor was washed with H₂O.

5. To activate the carboxylic acid groups of the gold platform, an aqueous solution of 400 mM EDC [1-ethyl-3-(3-dimethylaminopropyl) carbodiimide] and 100 mM NHSS [N-hydroxysulfosuccinimide ester] was prepared. The electrode was covered with 30 μL of this solution.



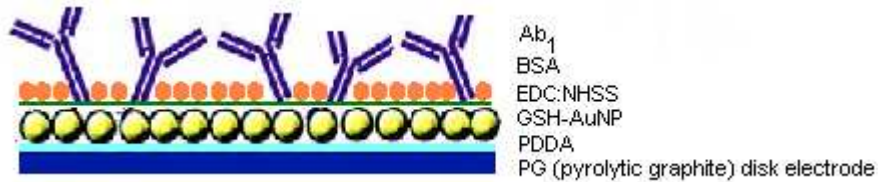
6. After 10 min, the excess reagent was removed by washing the electrode with H₂O.

7. The EDC-activated particles were reacted with amine groups of the primary antibody Ab₁. It is known⁵ that immobilization of Ab₁ does not diminish its bioactivity. For this step, 20 μL of a 25 μg/mL solution was drop casted on the sensor. The electrode, covered with a wet Vial, was then put in an oven at 37 °C for 2.5 h.



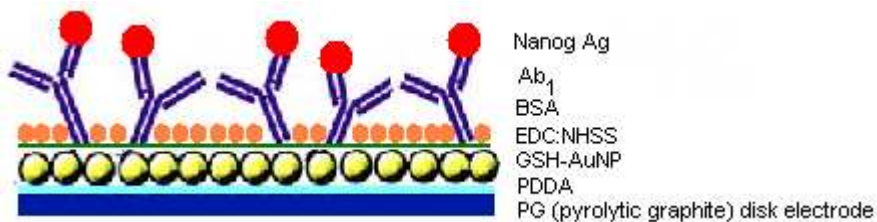
8. To remove all not-binding elements, the electrode was washed for 3 min with PBS buffer with 0.05% Tween-20 surfactant, and then for 3 min with PBS buffer (0.01M pH=7.0). The electrode was shaken to remove excess water buffer.

9. The inhibition of nonspecific binding of labeled detection antibodies is crucial to achieve high sensitivity and low detection limits. To optimize this step, the surface was treated with 20 μL of a 0.2% BSA solution [Bovine Serum Albumin] in PBS. The electrode was then put in an oven at 37 $^{\circ}\text{C}$ for 45 min.



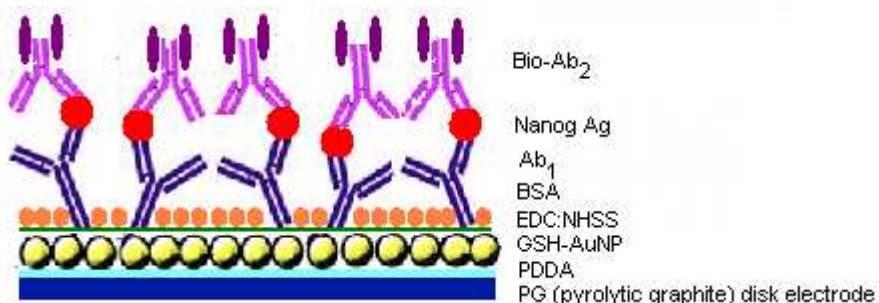
10. Step 8 was repeated.

11. 10 μL of the given test solution of Nanog Antigen (NA) were incubated onto the surface. We used various concentrations; for example, if the procedure involved activation of 9 electrodes, three were used for the control (0 pg/mL NA), three for the first concentration (e.g., 25 pg/mL NA), and three for a higher concentration (e.g., 50 pg/mL NA). The electrodes were put in an oven at 37 $^{\circ}\text{C}$ for 1 h.



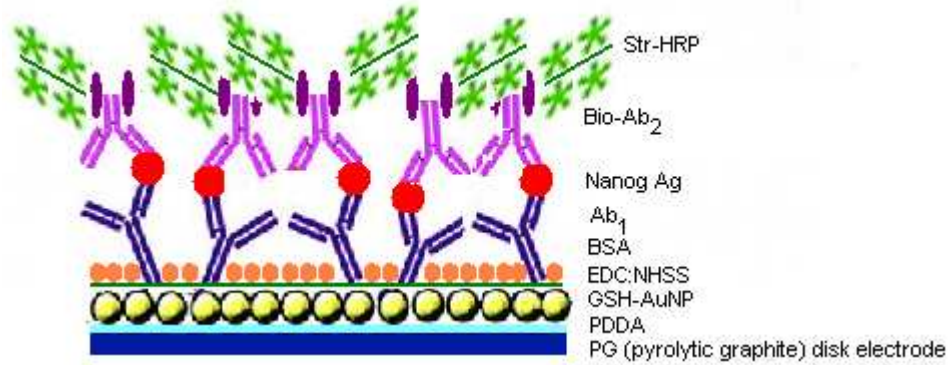
12. Step 8 was repeated.

13. The sensors with bound Nanog were then incubated using 10 μL of a 1 $\mu\text{g}/\text{mL}$ solution of the secondary antibody Biotin-Ab₂. The electrodes were put in an oven at 37 $^{\circ}\text{C}$ for 45 min.



14. Step 8 was repeated.

15. The final incubation step consisted in labeling Ab_2 with 10 μL of a 5 $\mu\text{g}/\text{mL}$ solution of Srt-HRP (horseradish peroxidase enzyme, functionalized with Streptavidin). The electrodes were put in an oven at 37 °C for 30 min.

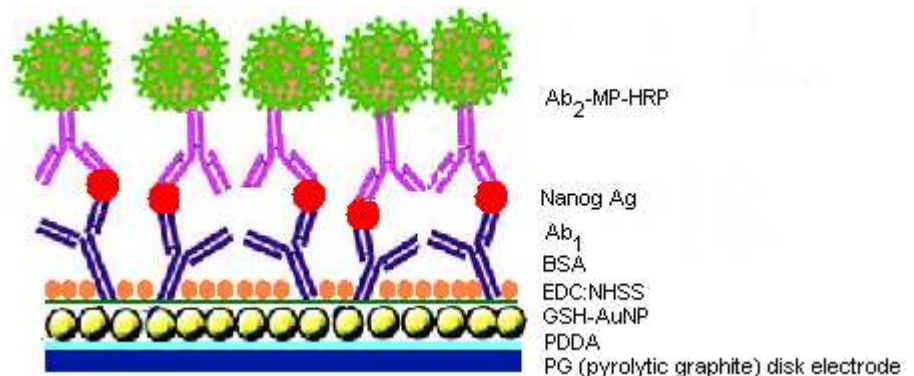


16. The electrodes were washed for 3 min with PBS-T20 buffer, and then for 3 min with PBS buffer (0.01M pH = 7.0). The electrodes were covered with wet Vials and put in a refrigerator.

To amplify sensitivity and improve the detection limit, a different procedure was also applied, starting from step 13.

13'. In a separated eppendorf we prepared 100 μL of a solution composed by 0.2 % BSA PBS buffer (pH = 7.0) solutions: 50 μL of 5 $\mu\text{g}/\text{mL}$ solution of multiple HRP labels; 30 μL of 2.5 $\mu\text{g}/\text{mL}$ solution of magnetic beads (FeO_2 , with a diameter of $\sim 1 \mu$); 20 μL of 2500 $\mu\text{g}/\text{mL}$ solution of Ab_2 . 10 μL of a dilute solution of this mixture was used for incubating the electrodes.

14' The electrodes were washed for 3 min with PBS-T20 buffer, and then for 3 min with PBS buffer (0.01M pH = 7.0). The electrodes were covered with wet Vials and put in a refrigerator.



2.3 Fabrication of the Microfluidic Device and Preparation of Eight-Electrode Array

To prepare the microfluidic channel, the PDMS kit was used: the PDMS base and curing agent were mixed in 10:1 ratio, stirred vigorously for 5 min, and then degassed for 30 min under dynamic vacuum to remove all air bubbles. The clear solution was poured onto a negative mold and heated at 85°C for 2.5 h.¹⁴

After cooling, the linear-shape PDMS was peeled off the mold, then placed between two flat and machined poly(methylmethacrylate) (PMMA) plates to provide a microfluidic channel (Figure 14).¹⁴

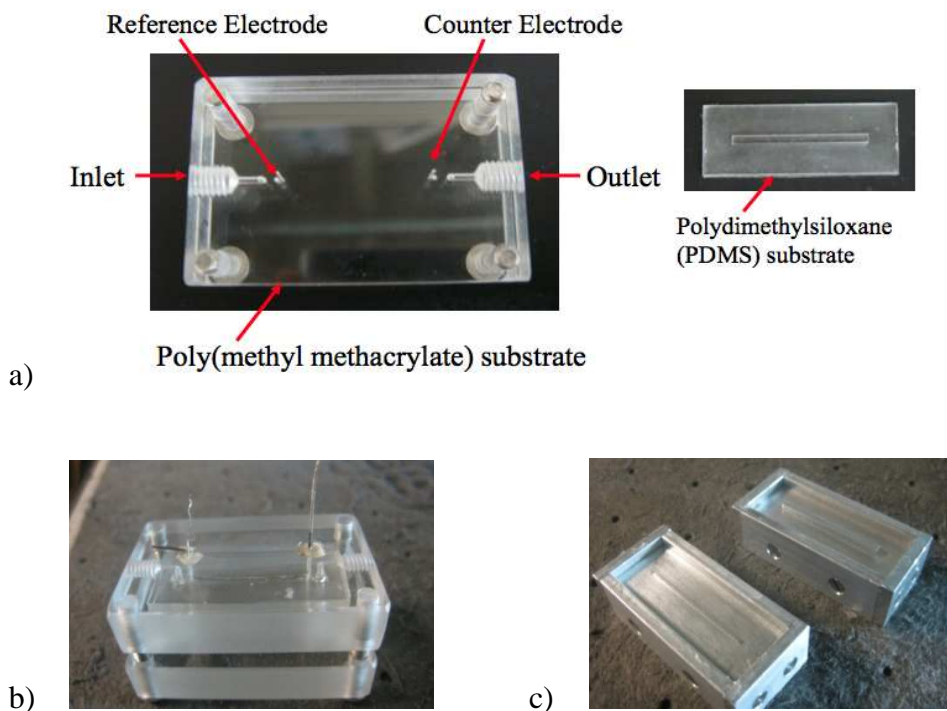


Figure 14. a) Photographs of the PMMA device and the PDMS channel; b) photograph of the entire microfluidic device; c) photograph of the molds for the PDMS channel.

The channel is ~1 mm wide, ~2 mm thick, 27 mm long and carries ~54 μ L volume. The top PMMA plate was machined with one inlets and one outlet and equipped with female ports (4 mm diameter) for screwing in standard plastic

fittings (1.5 mm i.d., Upchurch) to hold connecting 0.2 mm i.d. tubing (PEEK). Samples were injected by a syringe pump (Harvard, no. 55-3333) connected to one inlet via an injector valve (Rheodyne, no. 9725i) via 0.2 mm i.d. tubing (Figure 15). The top PMMA substrate is equipped with four holes (0.5 and 0.2 mm diameter) directly above the microfluidic channel; two for inserting Ag/AgCl wire used as a reference and two for inserting Pt wire as counter electrode.¹⁴

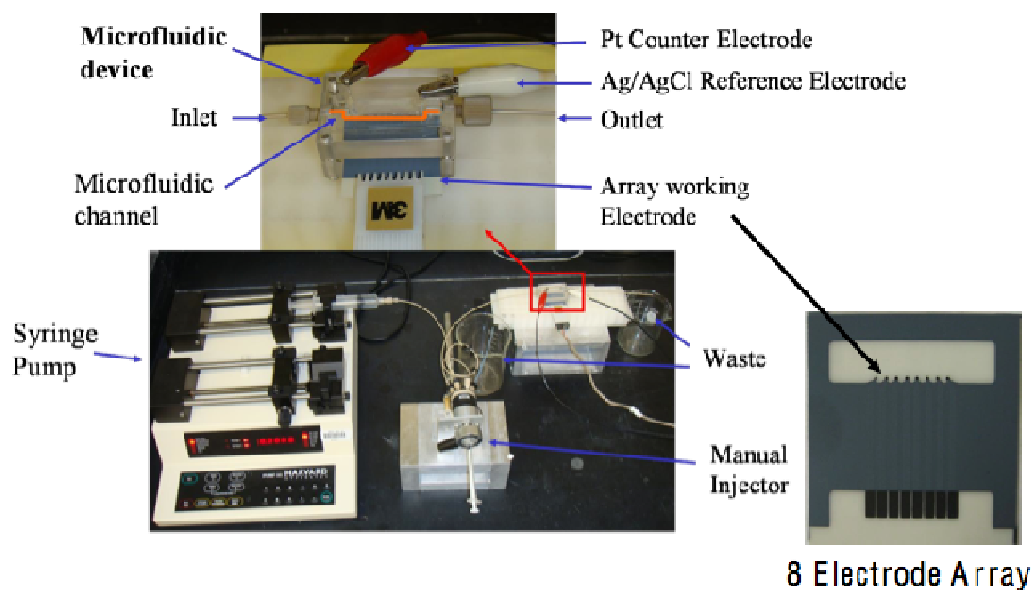


Figure 15. Photograph of the entire microfluidic system.

For the eight-electrode array system (arrays of eight graphite electrodes were manufactured by Kanichi Research Ltd, Manchester, UK), we essentially followed the same functionalization procedure used for the single rotating disk electrode (section 2.2). The difference was that while the PDDA, the AuNPs and Ab₁ were put manually, the BSA 0.2%, the Nanog and the Ab₂-MP-HRP mixture were injected by using the syringe pump. For this purpose, the syringe of the Harvard pump was filled up with the PBS buffer and the flow rate set to 50 $\mu\text{L}/\text{min}$.

~50 s after injection of the BSA solution with the injection valve, the fluid could reach the channel and cover completely all electrodes. At this point the flow was blocked to permit the incubation. For this step is very important to avoid any bubble, otherwise the sensor is compromised. The procedure was repeated for NA and Ab₂-MP-HRP. After every incubation, the sensor was washed with PBS and PBS-T20.

2.4 Gold Preparation and SAM formation

Formation of reproducible and well-packed Aib-based peptide SAMs is very sensitive to the cleaning – activation procedure. After trying different procedures, SAM formation was optimized by careful application of the following protocol leading to very reproducible results. For all experiments we used 11 x 11 mm ArrandeeTM gold plates, which consist of a borosilicate glass substrate (thickness 0.7 ± 0.1 mm), a thin chromium interlayer (2.5 ± 1.5 nm), and a gold layer (250 ± 50 nm). We used a new Au plate for each experiment.

The plates were first immersed in ethanol for 5 min, dried in vacuum for 30 min, immersed for 5 min in a freshly prepared but already cold piranha solution (3:1 v/v solution of concentrated sulfuric acid and hydrogen peroxide. *Extreme caution must be exercised when using piranha solution, as it is a very strong oxidant and reacts violently with organic matter*), and then carefully washed with a stream of water (deionized and then distilled from potassium permanganate). After washing, the plates were immersed in water for 5 min, and the procedure repeated three times. The plates were then dipped into ethanol for 5 min and dried in a desiccator under vacuum for 30 min. Annealing was carried out using a butane torch for soldering electronics, in a slightly darkened room. The flame was set for conical blue (reducing flame) and first allowed to touch obliquely the borders of the gold surface, and then moved steadily inward in a square fashion: annealing eventually caused appearance of a dark red glow on the gold surface. After waiting a few seconds to allow the surface to cool down, the same sequence step was repeated for an overall 3 min. The plates were left to cool down for 30 min, under a protecting glass cap. The annealing/cooling procedure was repeated three times. The plates were then immersed in water, ethanol, and finally either immersed into the peptide-containing ethanol solution or dried under vacuum.

Some experiments were specifically carried out to analyze the condition of the gold surface. Thus, after annealing and washing, the plates were dried in a desiccator under argon for 1 h and then either studied by scanning tunneling microscopy (STM: PicoSPM, Molecular Imaging) or cyclic voltammetry (CV). STM analysis of the so-prepared plates were carried out at room temperature

under ambient conditions using Pt/Ir (80:20, 0.25 mm diameter, Veeco) tips. The images were recorded in constant current mode and the typical conditions for the imaging of Au(111) terraces were $V_T = 200$ mV, $i_T = 100$ pA. This technique revealed that the Au surface displayed a preferred (111) orientation with terraces as large as ~ 100 nm that were atomically flat and separated by monoatomic steps (0.24 nm). To further test the outcome of the annealing procedure, we carried out CV experiments in 0.5 M H_2SO_4 and potential cycling was performed to include both the double-layer and the oxide regions of gold. The CV curves largely showed the pattern expected for the underpotential deposition of oxygen onto a clean Au electrode, mostly Au(111), in a contaminant-free solution,⁹¹ thereby confirming both the quality and dominant orientation of the annealed surface.

We also calculated the roughness factor of the so-obtained Au plates. The roughness factor is the ratio between the electrochemical and the geometrical areas. For these electrochemical experiments, the Au plates were clamped to a small gold alligator and most of the electrode surface was wrapped with a very thin Teflon tape. The geometrical areas were calculated by integration, using pictures of the exposed electrode surface in comparison with area standards. The determination of the electrochemical area was carried out on the (naked) Au plates obtained after full reductive desorption of the peptide SAM.⁸⁹

CV experiments were run at $0.1 - 1$ V s^{-1} in 0.5 M KCl containing $Ru(NH_3)_6Cl_3$, whose diffusion coefficient is $6.84 \pm 0.06 \times 10^{-6}$ $cm^2 s^{-1}$.⁸⁹ The electrochemical (= active) area could be calculated from the peak current values, using the equation valid for a reversible ET.⁹² The average roughness factor was found to be 1.16 ± 0.08 .

After annealing and washing, the freshly prepared gold plates were immersed for 48 h in a 0.5 mM ethanol solution of the peptide of choice. To carefully remove any trace of the incubation solution and loose molecules adsorbed on the monolayer, the gold plates were washed with a stream of ethanol and then immersed in ethanol for 5 min; these washing steps were repeated three times. The plates were finally dried under vacuum for 30 min. The cleaning/activation/incubation procedure was applied just before carrying out the IRRAS measurements.

2.5 Instrumentation and procedures

2.5.1 Electrochemistry

Rotating-Disk Electrode Approach. A CHI 660 electrochemical workstation was used for cyclic voltammetry and amperometry at ambient temperature ($22 \pm 2^\circ\text{C}$) in a three-electrode cell. Amperometry was carried out at -0.3 V against the standard saturated calomel electrode (SCE), using a pyrolytic graphite (PG) working electrode (rotated at 3000 rpm for optimum sensitivity), and a platinum wire counter-electrode.

Microfluidic Setup. The experiments were performed using a CHI 1010A eight-channel potentiostat allowing to simultaneously measuring the current flowing at the eight electrodes inserted in the microfluidic channel. Amperometry was carried out at -0.2 V vs the Ag/AgCl reference electrode, and using a platinum wire as the counter-electrode. For cyclic voltammetry experiments, the flow rate was set a zero, while for the amperometric detection the flow rate was $100 \mu\text{L}/\text{min}$ using $100 \mu\text{L}$ injector sample loop. Buffer and hydrogen peroxide solutions were deoxygenized with nitrogen.

2.5.2 IRRAS

FT-IR reflection absorption spectroscopy measurements were carried out using a Nicolet Nexus Fourier Transform Infrared Spectrometer equipped with a liquid nitrogen cooled mercury-cadmium-tellurium (MCT) detector. The measurements were carried out with the grazing angle set at 80° , with a resolution of 2 cm^{-1} , and each spectrum was the result of an average of 1000 scans. The optical path was purged with nitrogen before and during the measurements. To keep the measuring chamber constantly under an inert atmosphere, we set up a little dry-box containing the entire optical path. The sample and the blank (an otherwise identical Arrandee gold plate, but with no SAM) were inserted in the dry-box. Before measurements, the system was purged for 1 h with nitrogen dried by flowing through a column filled with CaCl_2 and silica gel.

3. Results and Discussion

3.1 Electrochemical Immunosensors

Electrochemical detection combined with nanoparticle amplification offers potentially low-cost, high-throughput solutions for detection of clinically significant proteins that have yet to be fully realized. Amperometric sensors, field effect transistors, and impedance methods are among the approaches being explored. The sensitivity of an electrochemical sensor can be improved by using nanostructured electrodes, such as those based on carbon nanotubes or gold nanoparticles. In the electrochemical detection of proteins on these specific electrode surfaces by immunoassay protocols, appropriate functional groups on the nanoparticle facilitate high concentrations of chemically linked capture antibodies. In this approach, antibodies on the electrode capture analyte proteins from the sample, the surface is then treated with an enzyme-labeled secondary antibody, and the enzyme label is detected electrochemically.

3.1.1 Characterization of AuNP platform

Glutathione-protected gold nanoparticles (GHS-AuNP) were prepared by a reported method⁹ and characterized by Transmission Electron Microscopy (TEM), UV-Vis and Infrared Spectroscopy.

The glutathione protected gold nanoparticle dispersion was analyzed for core dimensions and size distribution by TEM. Figure 16a shows that all particles are spherical and are well separated from each other. The size histogram obtained from analysis of the TEM images revealed that the average diameter of GHS-AuNP was 5.1 ± 1.4 nm, a relatively narrow size distribution.

Particle size was confirmed by visible absorption spectroscopy band for the GHS-AuNP dispersion at 508 nm indicating diameter ~ 5 nm (Figure 16c).

This absorption peak corresponds to gold plasmon band, confirming that the solution contained isolated nanometric sized gold particles.

The presence of glutathione on the AuNPs was confirmed by observation of characteristic carbonyl and amide bands at 1538, 1628, and 1713 cm^{-1} by IR Spectroscopy (Figure 16c).

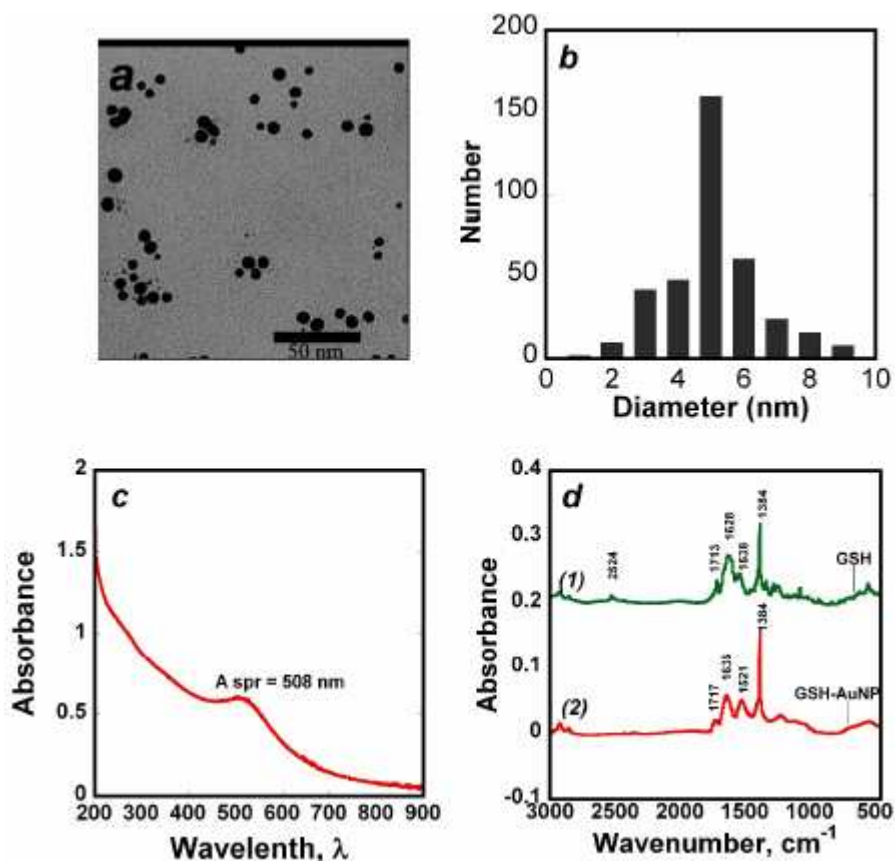


Figure 16. Characterization of glutathione protected gold nanoparticles: a) TEM image of GHS-AuNPs; b) corresponding size distribution histogram of GHS-AuNPs showing average size 5.1 ± 1.4 nm; c) UV-Vis absorption spectra of glutathione protected gold nanoparticle dispersion in HEPES buffer; d) IR spectra of (1) pure glutathione and (2) glutathione protected gold nanoparticles.

The surface was also characterized by tapping-mode atomic force microscopy (Figure 17). The initial thin layer of PDDA (0.5 ± 0.2 nm) adsorbed was relatively smooth with mean surface roughness of 0.13 ± 0.08 nm, almost twice that of the bare mica. Figure 17 panels b, c shows an AFM image that changed topography after AuNPs were adsorbed onto the PDDA layer. The AFM

data suggest that there is a densely packed nanoparticulate layer, which can be associated with the AuNPs. A nearly complete coverage on the underlying surface is achieved with a mean surface roughness, as the arithmetic average deviation of the surface valleys and peaks, of 1.99 ± 0.11 nm, corresponding to about a 24-fold increase in surface area with respect to bare mica. Figure 17 d shows an AFM image obtained after the capture antibody was covalently linked onto the carboxylated of the AuNP layer using EDC/NHSS chemistry. The densely packed AuNP layer disappeared and a rolling hill-like appearance, generally characteristic of any globular protein coated on a rough surface, was observed.⁹

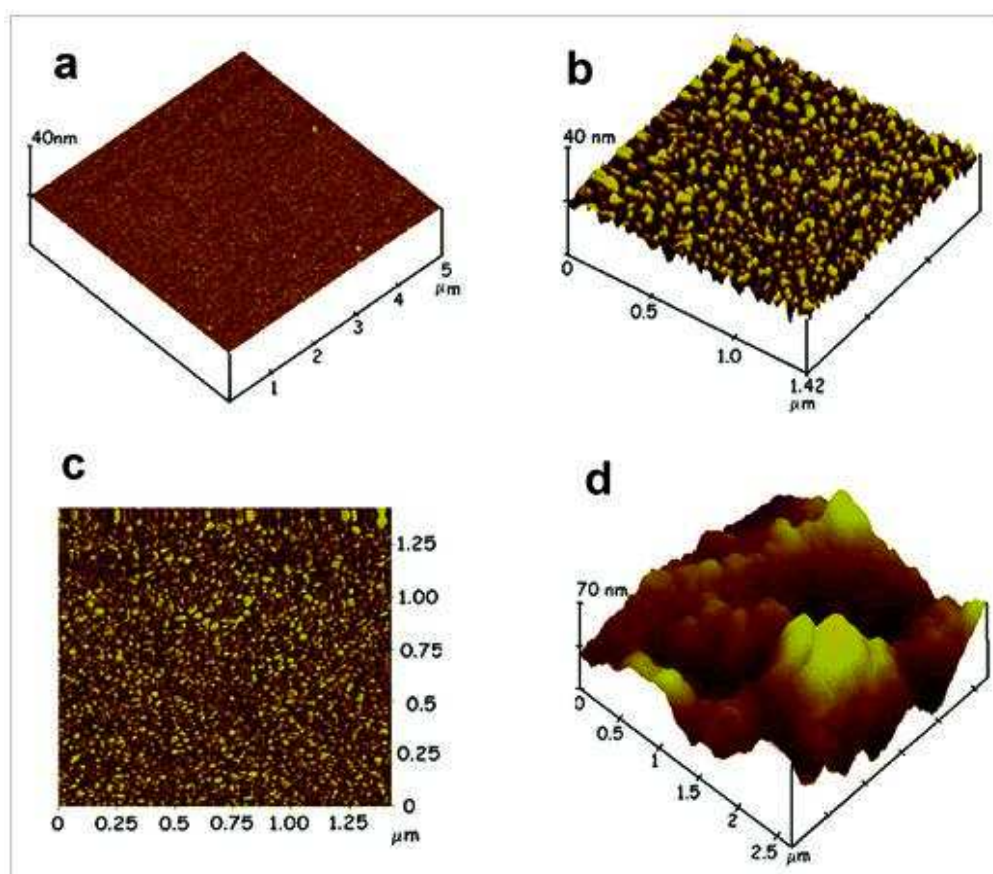


Figure 17. Tapping-mode atomic force microscope images of (a) layer of PDDA on smooth mica surface; (b) PDDA/AuNP bilayer; (c) phase contrast image of PDDA/AuNP bilayer; (d) AuNP platform after covalent linkage of primary antibodies (Ab_1) onto the glutathione carboxylate groups of AuNP.

3.1.2 Electrochemistry of immunosensors

The AuNP/Ab₁/Ag/Ab₂/MP/HRP electrode, assembled as described in the Experimental Section, was transferred in an electrochemical cell or in the microfluidic channel filled with of pH 7.0 buffer and 1mM hydroquinone (HQ). In both cases, the cyclic voltammetry (CV) was carried out in quiescent solution to confirm that the electrode was performing well: with the rotating-disk electrode the angular speed was set to zero and with the microfluidic channel the flow of the PBS buffer with the HQ was stopped. Usually, a well-defined, nearly reversible HQ reduction-oxidation peak pair vs Ag/AgCl (Figure 18, 19) was obtained, due to the oxidation (+0.35 V) and reduction (-0.15 V) of HQ. A possible increase of the peak current at negative potentials indicated that oxygen was still present in the cell, and thus the solution had to be further purged before carrying out the actual CV measurements.

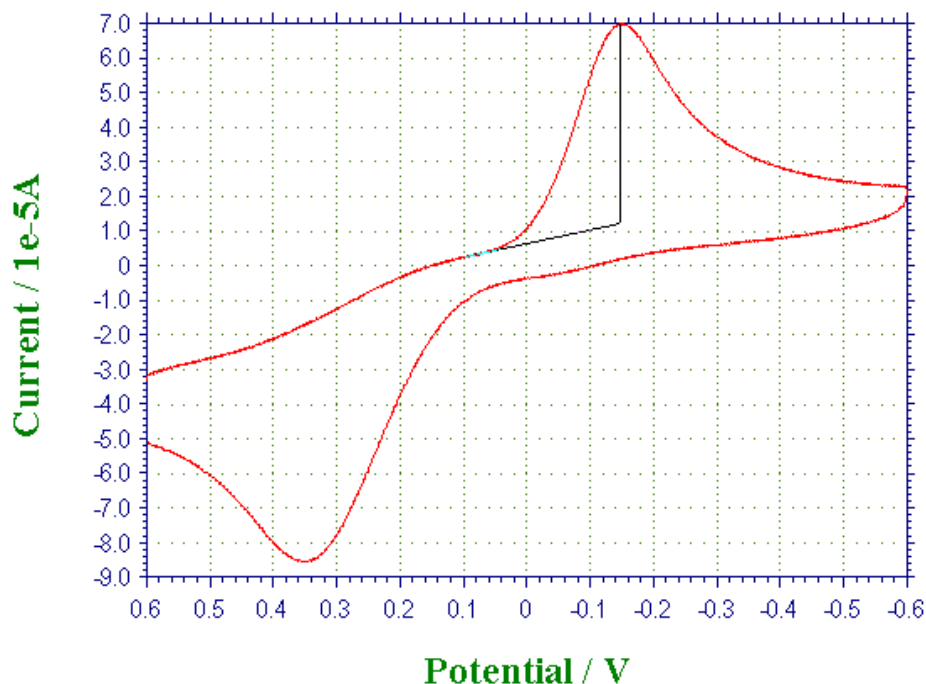
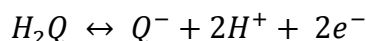


Figure 18. Typical cyclic voltammetry of 1 mM HQ in pH 7.0 phosphate buffer using an AuNP/Ab₁/Ag/Ab₂/MP/HRP (steady: see text) rotating-disk electrode. Scan rate = 0.2 Vs⁻¹.

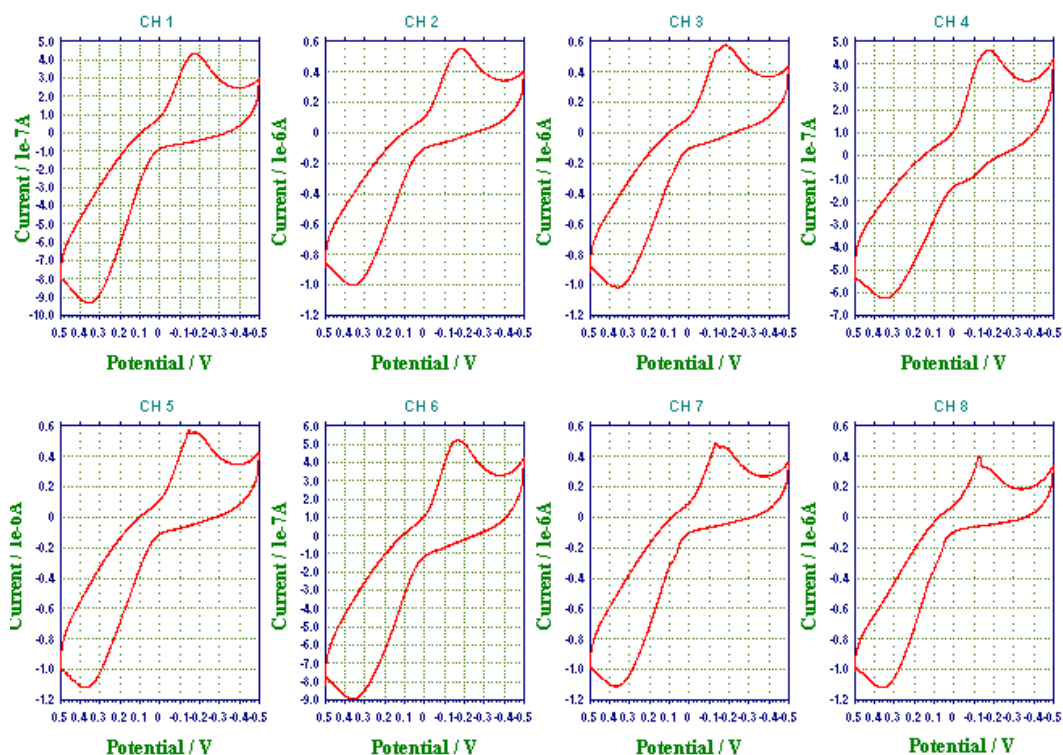


Figure 19. Typical cyclic voltammetry of 1 mM HQ in pH 7.0 phosphate buffer using an AuNP/Ab₁/Ag/Ab₂/MP/HRP eight-electrode array in the microfluidic channel.

The best experimental conditions allowing us to obtain the lowest detection limit of the biomarker Nanog were assessed with a single rotating-disk electrode approach (Figure 20). Afterwards, the method was automated by using microfluidics.

Rotating-disk electrodes are extensively employed in electroanalytical research. Advantages of these electrodes over those having different shapes are the reproducibility of the results, the precise control of the rates at which the electroactive substances are transported to the electrode (forced convection), and a practically even current distribution on the surface during the course of the electrochemical reaction.⁹³

The movement of a liquid caused by a disc rotating around an axis perpendicular to its plane has been described.^{94,95} It is assumed that the volume of the solution in which the disk is present is infinite, the disk is large, and the liquid flow is laminar. Figure 20 shows the model of movement of the liquid. At large

distances from the disk, the liquid moves perpendicularly to the surface. Near the disk, in the thin layer adhering to the surface of the electrode, the liquid also gains a centrifugal velocity. At very short distances, a layer of quiescent solution is present, whose thickness does not change in time. In this layer, mass transport effects the electroactive species only by diffusion.⁹³

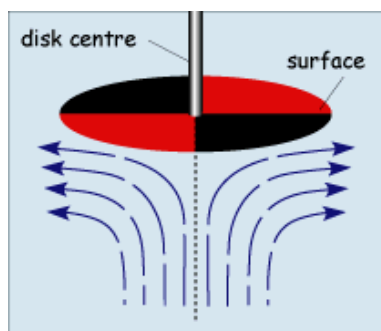


Figure 20. Flow profile that is developed when a circular object is rotated in solution and how this brings fresh reactant to the surface.

Providing the rotation speed is kept within the limits that laminar flow is maintained, the mass transport equation is given by:

$$\frac{dC}{dx} = -\frac{C}{\delta} - \frac{v_r}{D} \frac{dC}{dx}$$

where the x dimension is the distance normal to the electrode surface. The mass transport equation is determined by both diffusion (first term of the right-hand side member) and forced convection (second term), and both these terms effect the concentration of the reagent close to the electrode surface. At a potential sufficiently negative (positive) to make the reduction (oxidation) process controlled solely by mass transport, a limiting current (constant in time) arises. The full and correct equation, describing the limiting current in the case of rotating disk electrode, was obtained by Levich^{96,97}:

$$i_L = 0.627 n F A D^{1/2} \omega^{1/2} C$$

where i_l is the limiting current, n is the number of electron transferred, F is the Faraday constant, A is the electrode area, D is the diffusion coefficient, ω is the angular velocity of the rotating disk electrode, c^0 is the bulk concentration, and ν is the kinematic viscosity of the solution.

3.1.3 Analysis of the Immunosensors' Performance

In our sensor assembly, the working electrode was placed into an electrochemical cell containing 10 mL of a 1 mM HQ PBS buffer solution, which was purged with purified Nitrogen for at least 1 h before the measurements. We used a normal electrochemical cell with 5 holes: one for the working rotating-disk electrode, one for the reference electrode (SCE), one for the counter-electrode (Pt), one for the inert gas, and one for the injection of hydrogen peroxide.



Figure 21. In the upper image, there are the electrodes during the incubation of Ab_1 . On the right, the rotating disk electrode system is represented entirely, and in the last image there is a zoom of the electrochemical 5 holes cell that we used for the measurements.

For the sake of better reproducibility, we used 9 electrodes at the same time: 3 for the control, 3 for one specific concentration of antigen (for example 25 pg/mL) and 3 for another concentration (for example 50 pg/mL). The electrochemical measurements were carried out using a solution of 1mM of HQ. The latter is used as the ET mediator to ward hydrogen peroxide reduction, which is added successfully at 0.4 mM concentration. For the catalytic measurements, we applied a potential of -0.3 V vs SCE and a rotation rate of 3000 rpm.

Concerning the electrode reaction, it is useful making a few comments about HRP oxidation by H_2O_2 . The horseradish peroxidase is a protein that contains a single protoporphyrin IX heme group, and thus the addition of H_2O_2 converts the iron heme peroxidase enzyme to a ferryl-oxo species (Figure 21). The latter can be electrochemically reduced by the electrode.

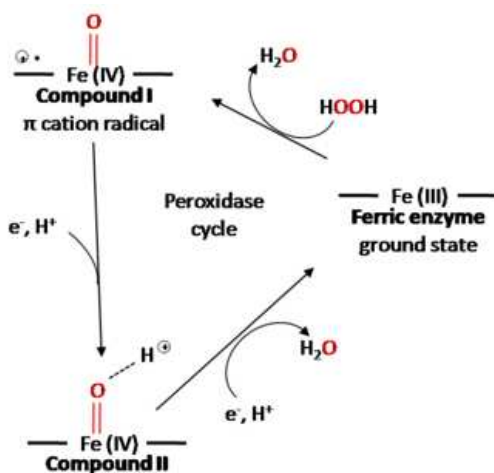


Figure 22. Oxidation cycle of Horseradish peroxidase.

The immunosensors have a complex sandwich structure. To optimize the experimental conditions and the value of the detection limit, we changed several parameters, one at a time, because every biomarker has a specific characteristic behavior.

At the beginning, we had no information about this protein and thus we tried almost randomly different concentrations in order to find the best range to work. This is particularly important also because, beyond a specific concentration, saturation of the immunosensor occurs and the current does not change with a further increase of the concentration of the Nanog Antigen (NA). The various approaches were as described in the following.

First approach:

Ab ₁	25 µg/mL	in PBS buffer pH = 7.0
BSA	0.1%	in PBS buffer pH = 7.0
NA	Several concentrations	in PBS buffer pH = 7.0
Biotin-Ab ₂	1 µg/mL	in PBS buffer pH = 7.0
Streptavidin-HRP	5 µg/mL (1:200)	in PBS buffer pH = 7.0

As Figure 23 shows, with this method the sensitivity of our immunosensor is really poor and the signal is not proportional to the concentration of the biomarker. Thus, we decided to change the conditions by increasing the concentration of Biotin-Ab₂ from 1 µg/mL to 5 µg/mL. We expected an enhancement of the number of HRP attached to the surface thanks to a larger number of Ab₂ molecules.

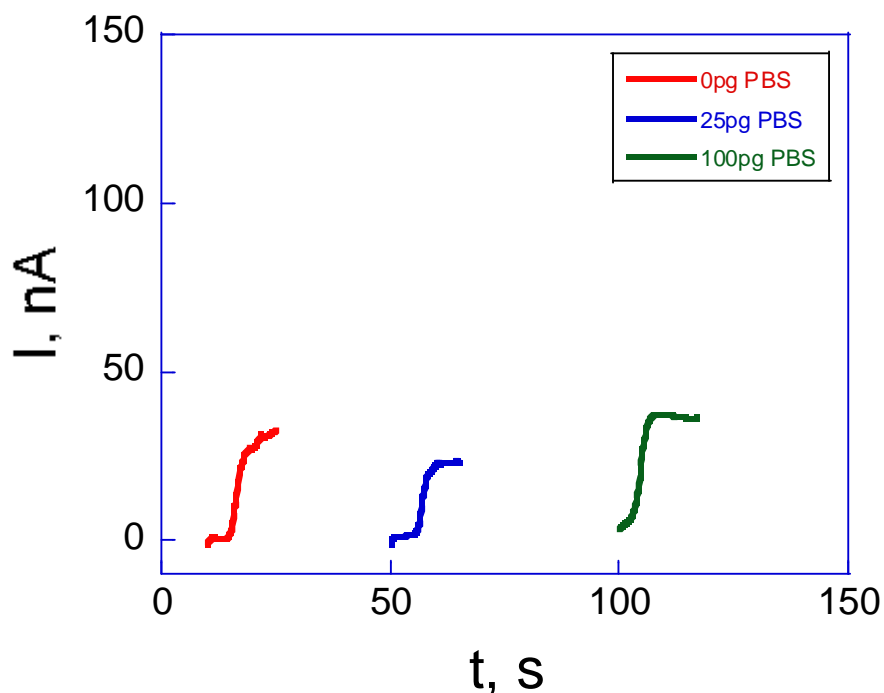


Figure 23. Amperometric results of the first approach (for the sake of better comparison the curves have been arbitrarily shifted).

Second approach:

Ab ₁	25 µg/mL	in PBS buffer pH = 7.0
BSA	0.1%	in PBS buffer pH = 7.0
NA	Several concentrations	in PBS buffer pH = 7.0
Biotin-Ab ₂	5 µg/mL	in PBS buffer pH = 7.0
Streptavidin-HRP	5 µg/mL (1:200)	in PBS buffer pH = 7.0

In this approach, we tried a few concentrations but we did not detect any particular increase of the signals. Thus, we decided to go back to the concentration of Ab₂ used in the first approach but changed the composition of the solution for both Biotin-Ab₂ and Str-HRP.

Third approach:

Ab ₁	25 µg/mL	in PBS buffer pH = 7.0
BSA	0.1%	in PBS buffer pH = 7.0
NA	Several concentrations	in PBS buffer pH = 7.0
Biotin-Ab ₂	1 µg/mL	in 2% BSA PBS T-20 buffer pH=7.0
Streptavidin-HRP	5 µg/mL (1:200)	in 2% BSA PBS T-20 buffer pH=7.0

As Figure 24 shows, the response for the lowest concentrations was good and the detection limit was particularly low, being 10 pg/mL. On the other hand, beyond 50 pg/mL, the current did not increase proportionally to the concentration. We did not know if this was due to the saturation of the sensor or to the presence of BSA, which acts as a blocking agent not only for the AuNPs platform but also for Ab₁. To address this issue, we repeated this approach while increasing the concentration of Ab₂.

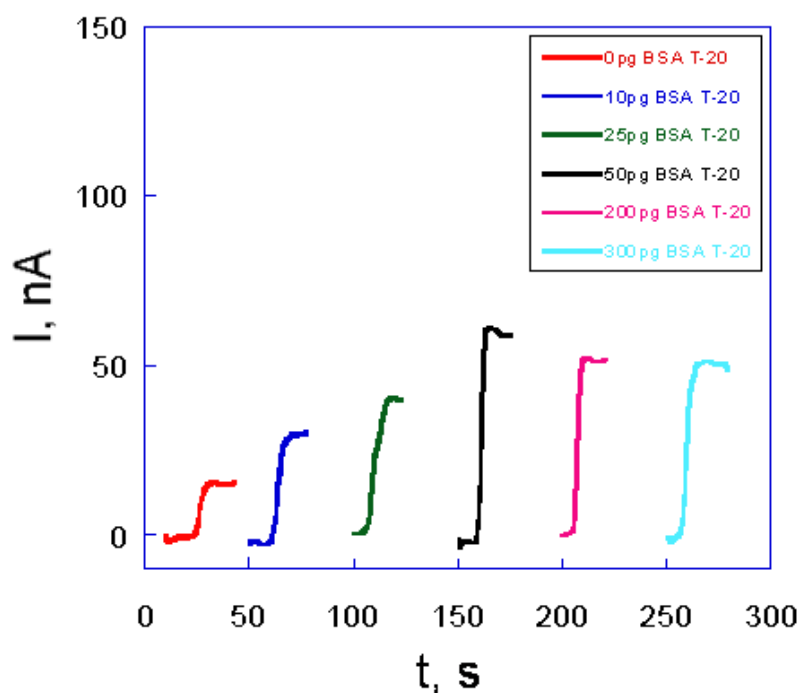


Figure 24. Amperometric results of the third approach (for the sake of better comparison the curves have been arbitrarily shifted).

Fourth approach:

Ab ₁	25 µg/mL	in PBS buffer pH=7.0
BSA	0.1%	in PBS buffer pH=7.0
NA	Several concentrations	in PBS buffer pH=7.0
Biotin-Ab ₂	5 µg/mL	in 2% BSA PBS T-20 buffer pH=7.0
Streptavidin-HRP	5 µg/mL (1:200)	in 2% BSA PBS T-20 buffer pH=7.0

As Figure 25 shows, the presence of BSA did not allow observing any difference between the control (0 pg/mL) and the two concentrations employed (50 and 100 pg/mL). This confirmed that BSA completely blocked Ab₁, thereby prohibiting its interactions with the Nanog biomarker.

Therefore, we decided to change the composition of the solution for both Biotin-Ab₂ and Str-HRP, using PBS T-20.

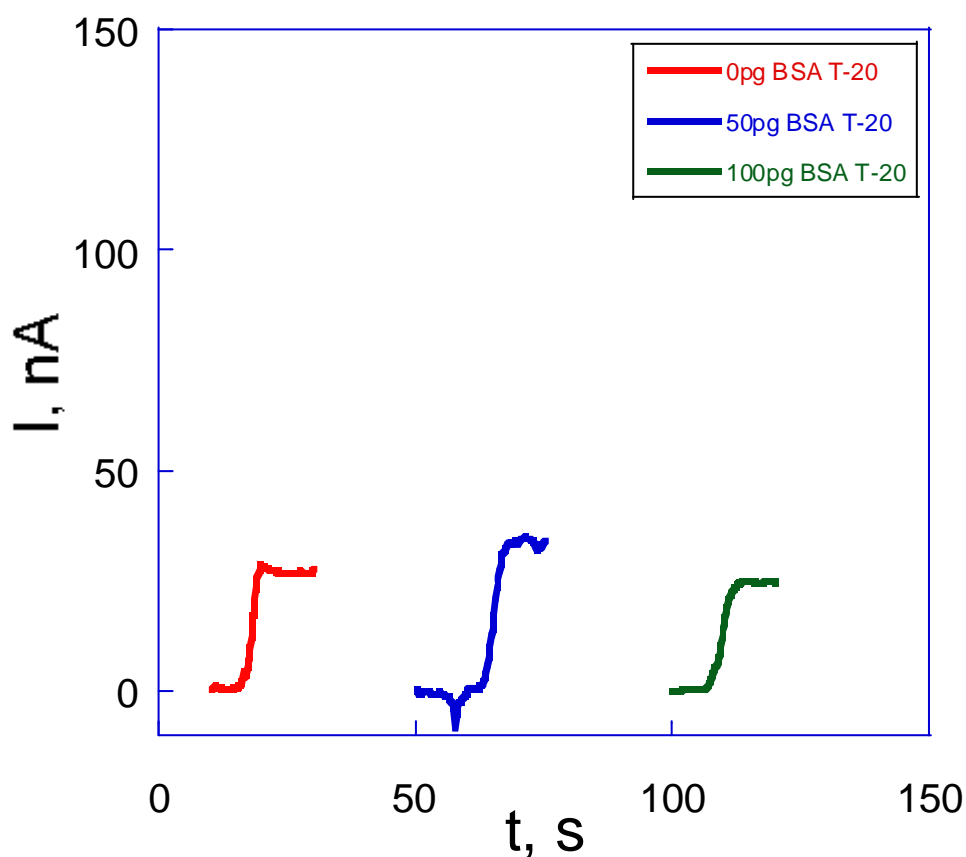


Figure 25. Amperometric results of the fourth approach (for the sake of better comparison the curves have been arbitrarily shifted).

Fifth approach:

Ab ₁	25 µg/mL	in PBS buffer pH=7.0
BSA	0.1%	in PBS buffer pH=7.0
NA	Several concentrations	in PBS buffer pH=7.0
Biotin-Ab ₂	5 µg/mL	in PBS T-20 buffer pH=7.0
Streptavidin-HRP	5 µg/mL (1:200)	in PBS T-20 buffer pH=7.0

As Figure 26 shows, this method seemed to work quite well, but after the first experiment we could not obtain a similarly low current control; in fact, it was usually very high, more than the detection limit. This was probably due to HRP also functionalizing the gold platform, not just Ab₂.

Therefore, to better protect the gold platform, we decided to increase the concentration of BSA during the second step of the procedure, and we prepared a Str-HRP solution in 0.2 % BSA PBS T-20 buffer pH=7.0.

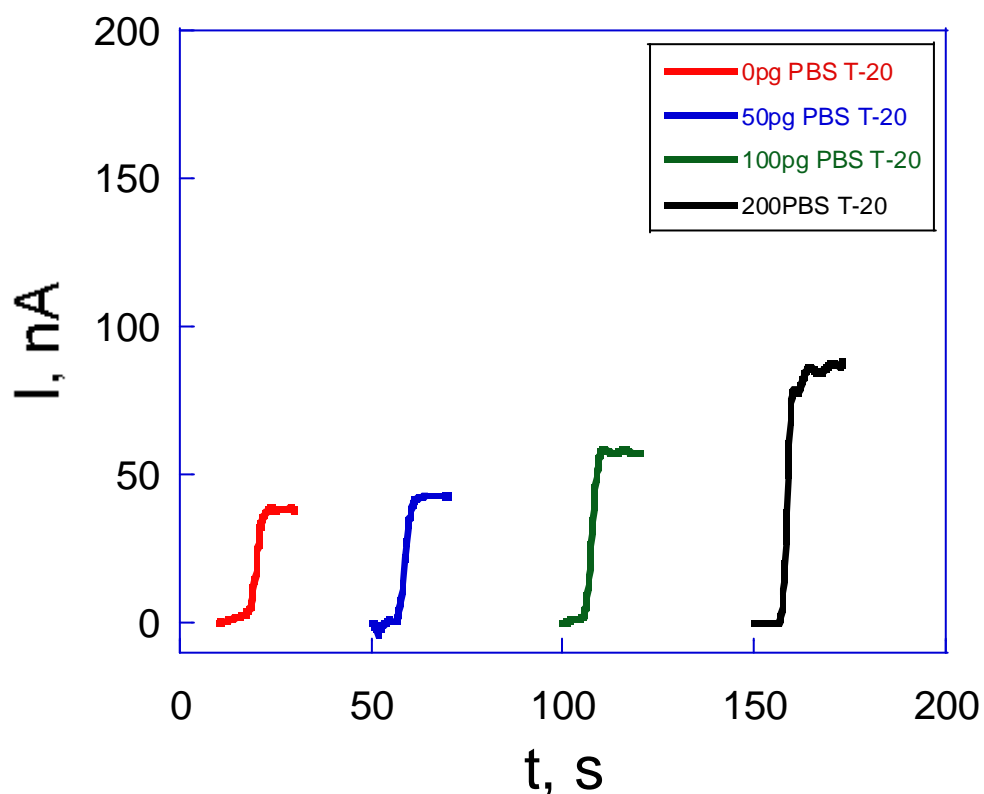


Figure 26. Amperometric results of the fifth approach (for the sake of better comparison the curves have been arbitrarily shifted).

Sixth approach:

Ab ₁	25 µg/mL	in PBS buffer pH=7.0
BSA	2%	in PBS T-20 buffer pH=7.0
NA	Several concentrations	in PBS buffer pH=7.0
Biotin-Ab ₂	5 µg/mL	in PBS buffer pH=7.0
Streptavidin-HRP	5 µg/mL (1:200)	in 0.2 % BSA PBS T-20 buffer pH=7.0

As Figure 27 shows, however, in this approach the detection limit was particularly high, larger than 50 pg/mL.

Since after testing the above approaches we could not establish any particular method allowing to provide sensitive and reproducible signals, with a low detection limit, we resorted to modify the preparation of the immunoassay by introducing magnetic particles. As a matter of fact, Rusling and coworkers nicely demonstrated that magnetic beads are very helpful to increase the sensitivity of similar biosensors.⁹

We also decreased the concentration of BSA in the second step, and we used 0.1% BSA PBS buffer (pH = 7.0) as the solution for BioAb₂-MPs-StrHRP.

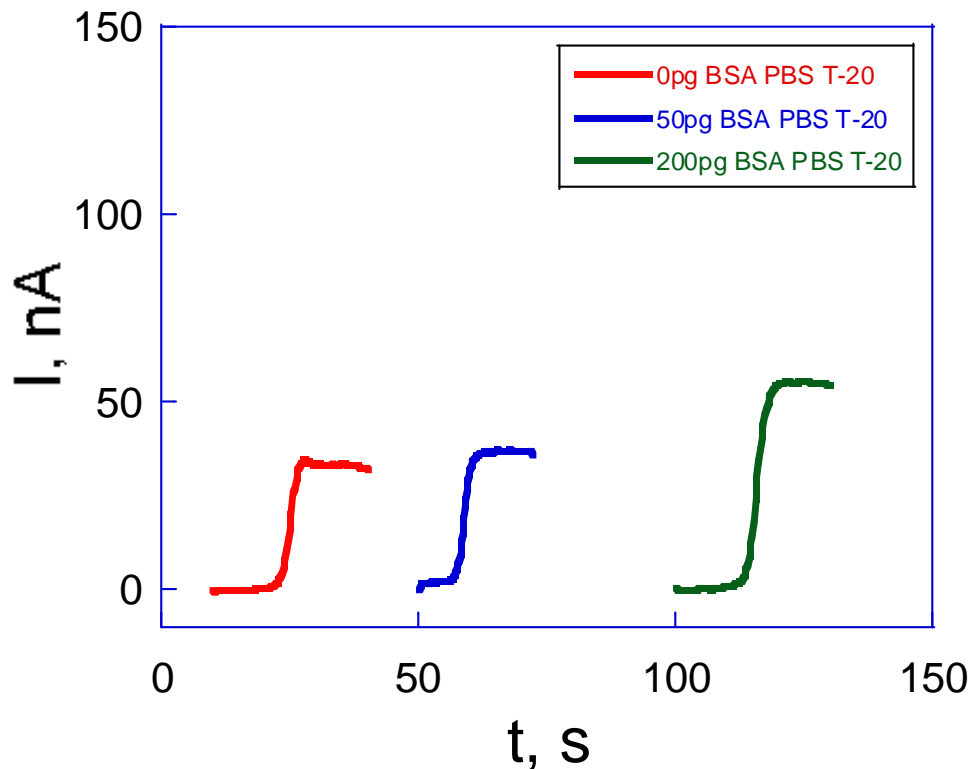


Figure 27. Amperometric results of the sixth approach (for the sake of better comparison the curves have been arbitrarily shifted).

Seventh approach:

Ab ₁	25 µg/mL	in PBS buffer pH=7.0
BSA	0.2%	in PBS T-20 buffer pH=7.0
NA	Several concentrations	in PBS buffer pH=7.0
BioAb ₂ -MPs-StrHRP	5 µg/mL per 50µL 2.5 µg/mL per 30µL 2500 µg/mL per 20µL 1:10 dilution	in 0.1% BSA PBS buffer pH = 7.0

To amplify the sensitivity and improve the detection limit, we thus attached multiple HRP labels to carboxylic group on magnetic bead surfaces. HRP and Ab₂ at a 120/1 HRP/Ab₂ molar ratio was reached with the carboxylated magnetic bead using the EDC amidization protocol. Carboxylic acid groups were first activated using EDC, excess reagent was removed by washing with water, and the activated particles were then reacted with amine groups on the proteins. Magnetic beads of diameter ~1 µm provided a very high number of labels on the surface. After the bioconjugation of HRP and Ab₂, the free antibodies and HRP were easily separated from the Ab₂-magnetic-bead-HRP by using a magnet to localize the beads at one side of an eppendorf and washing to remove unreacted protein. The amount of active HRP per unit weight of magnetic beads was determined by reacting the BioAb₂-magnetic-bead-StrHRP dispersion with HRP substrate 2,2'-azino-bis-(3-ethylbenz-thiazoline-6-sulfonic acid) and H₂O₂. The total number of magnetic beads, of ~1µm diameter, was 4 x 10⁹ in the dispersion, provided by Polyscience, and the number of active HRP per magnetic bead was estimated at 7500.⁹

As Figure 28 shows, the sensitivity improved very significantly with respect to the conventional Ab₂-HRP AuNPs immunosensor. The current values of Figure 28 were actually even too high because we wanted to analyze a significant range of concentrations with no risk of experimental limits. Therefore, we diluted the initial mixture of BioAb₂-MPs-StrHRP.

Figure 29 shows a simple graph in which we compare the slope of the concentration dependence of the amperometric intensities as obtained with a single label BioAb₂-StrHRP immunosensor with those recorded with the new immunoassay, based on magnetic particles and BioAb₂-MPs-StrHRP.

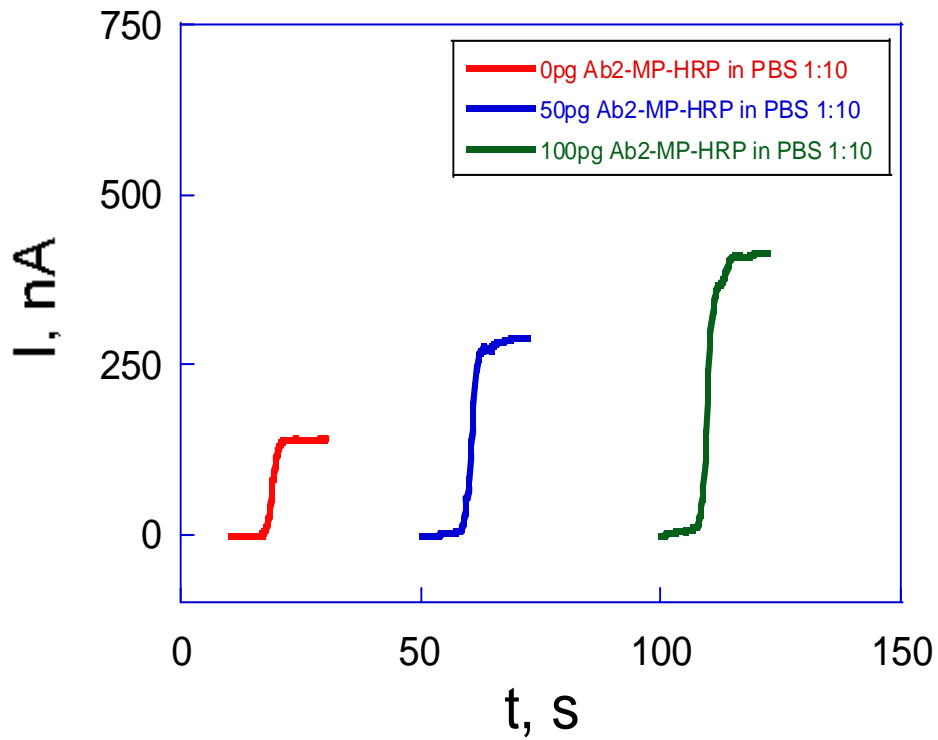


Figure 28. Amperometric results of the sixth approach (for the sake of better comparison the curves have been arbitrarily shifted).

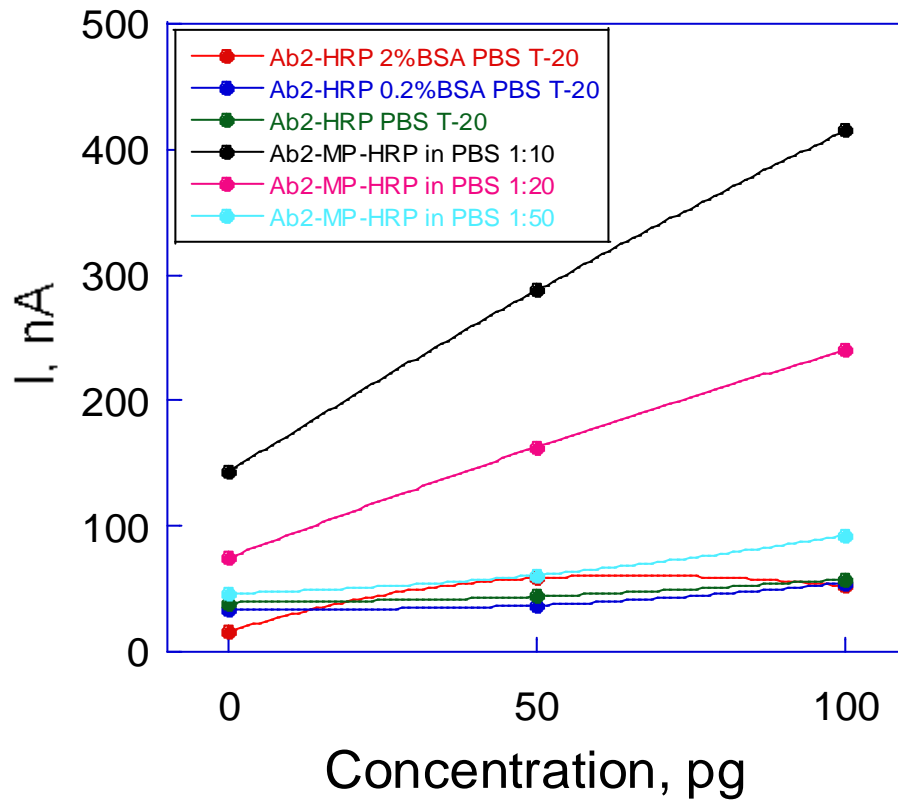


Figure 29. Calibration curves for various approaches, in the two different immunoarrays.

Eighth approach:

Ab ₁	25 µg/mL	in PBS buffer pH=7.0
BSA	0.2%	in PBS T-20 buffer pH=7.0
NA	Several concentrations	in PBS buffer pH=7.0
BioAb ₂ -MPs-StrHRP	5 µg/mL per 50µL 2.5 µg/mL per 30µL 2500 µg/mL per 20µL 1:20 dilution	in 0.1% BSA PBS buffer pH = 7.0

As Figure 30 shows, the intensities of signals were still high but less than before, while the slope was equal. Therefore, we diluted the mixture further.

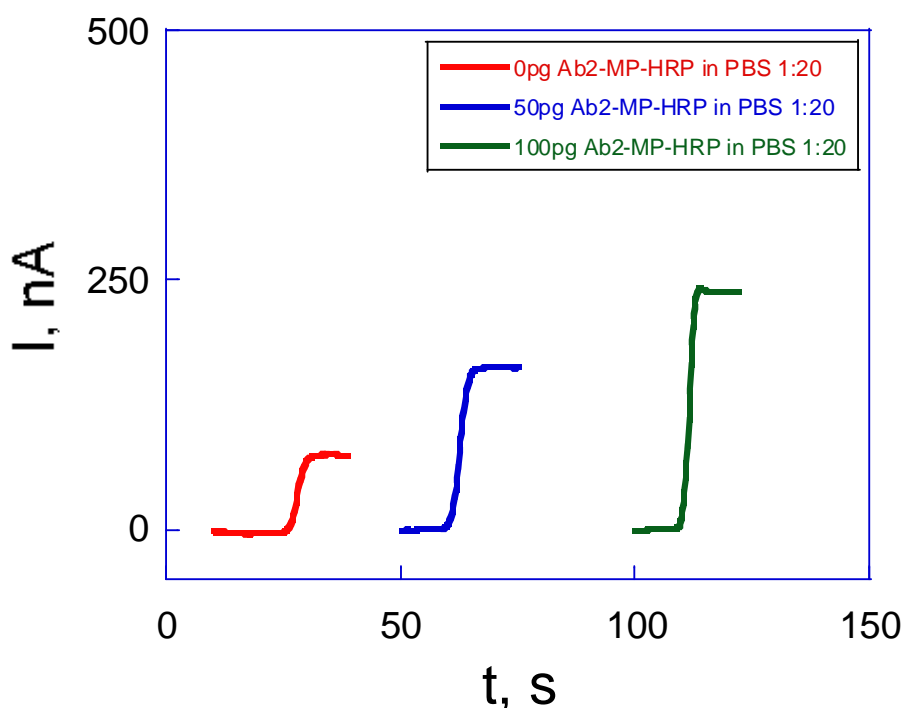


Figure 30. Amperometric results of the sixth approach (for the sake of better comparison the curves have been arbitrarily shifted).

Ninth approach:

Ab ₁	25 µg/mL	in PBS buffer pH=7.0
BSA	0.2%	in PBS T-20 buffer pH=7.0
NA	Several concentrations	in PBS buffer pH=7.0
BioAb ₂ -MPs-StrHRP	5 µg/mL per 50µL 2.5 µg/mL per 30µL 2500 µg/mL per 20µL 1:25 dilution	in 0.1% BSA PBS buffer pH = 7.0

Tenth approach:

Ab ₁	25 µg/mL	in PBS buffer pH=7.0
BSA	0.2%	in PBS T-20 buffer pH=7.0
NA	Several concentrations	in PBS buffer pH=7.0
BioAb ₂ -MPs-StrHRP	5 µg/mL per 50µL 2.5 µg/mL per 30µL 2500 µg/mL per 20µL 1:50 dilution	in 0.1% BSA PBS buffer pH = 7.0

In the ninth approach, the dilution was not sufficient, and thus we now make comments directly for the tenth approach in which we observed good values of current intensity, as Figure 31 shows. The detection limit was 10 pg/mL.

This approach, however, did not display a good reproducibility and thus we tried to optimize the biological conditions of our immunosensor by employing solutions with the same pH that was used during the synthesis of Nanog (pH = 7.4). To verify the improvement, we decided to go back to the conventional biosensor, and we also increased the concentration of BSA in the second step.

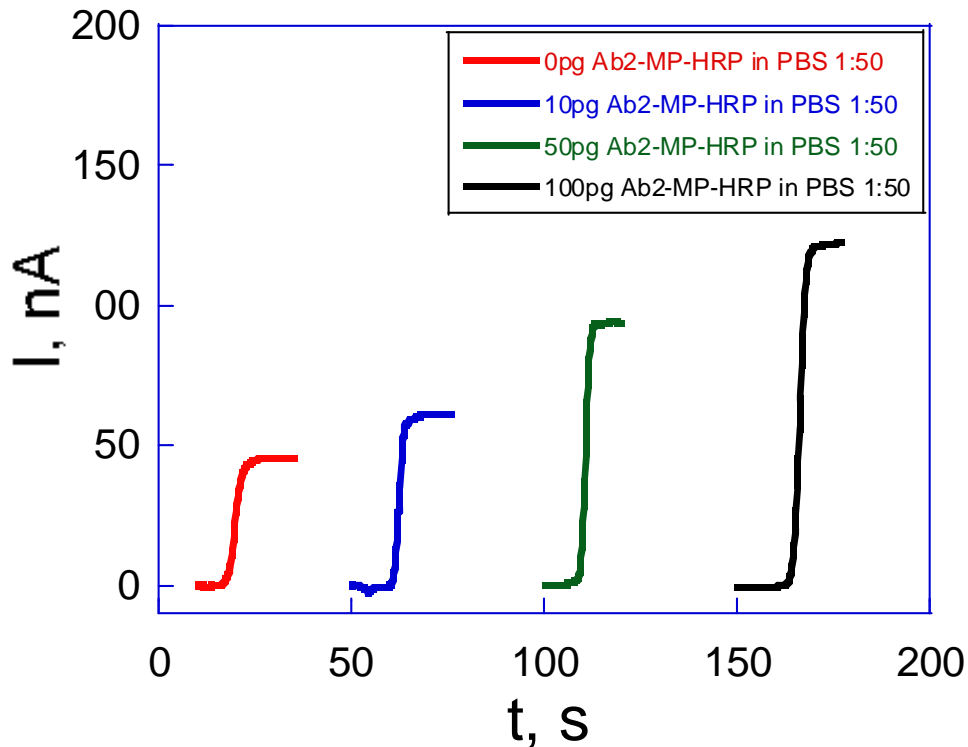


Figure 31. Amperometric results of the tenth approach (for the sake of better comparison the curves have been arbitrarily shifted).

Eleventh approach:

Ab ₁	25 µg/mL	in PBS buffer pH=7.0
BSA	2%	in PBS T-20 buffer pH=7.4
NA	Several concentrations	in PBS buffer pH=7.4
Biotin-Ab ₂	1 µg/mL	in 0.1% BSA PBS buffer pH=7.4
Streptavidin-HRP	5 µg/mL (1:200)	in 0.1% BSA PBS buffer pH=7.4

As Figure 32 shows, with this approach we obtained very good results for sensibility, reproducibility and reliability toward Nanog. In fact, the detection limit is 25 pg/mL, the sensitivity, calculated as the slope of the calibration plot (see Figure 33), is 0.639 nA·mL pg⁻¹, and the small error bars illustrate the excellent sensor-to-sensor reproducibility (see Figure 33).

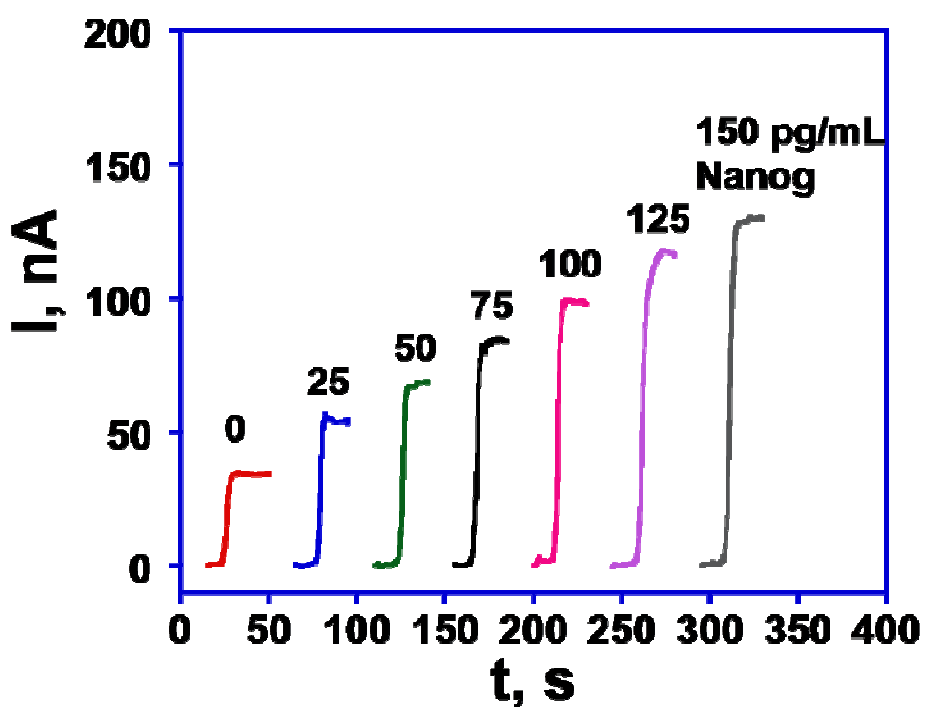


Figure 32. Amperometric results of the eleventh approach (for the sake of better comparison the curves have been arbitrarily shifted).

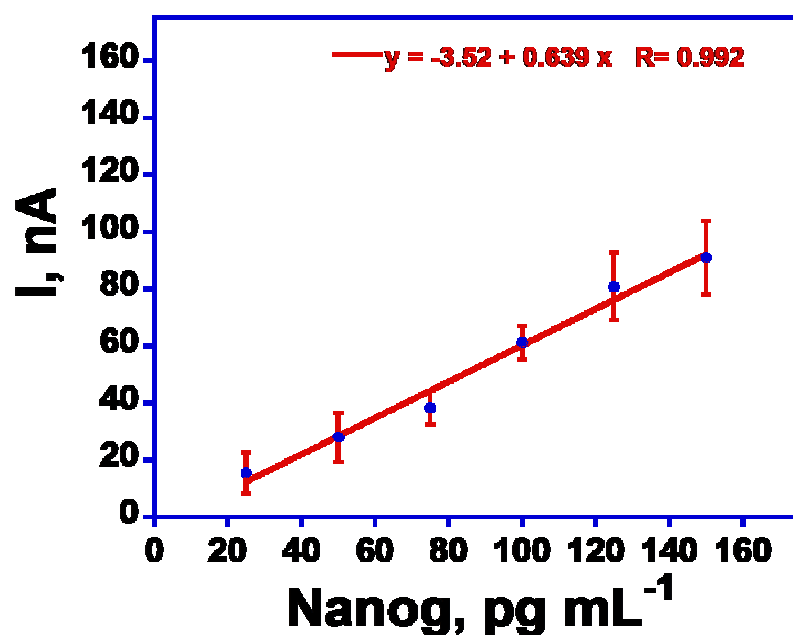


Figure 33. Immunosensor calibration plot for Nanog using the eleventh approach.

On the other hand, we wanted to obtain a detection limit low enough to have a sensor capable of measuring both normal cancer-free patients and patients with elevated levels of cancer. As we described above, this is possible by using magnetic beads and thus in the last step we used a 0.1% BSA PBS buffer (pH = 7.4) solution of StrMPs-BioAb₂-BioHRP.

Twelfth approach:

Ab ₁	25 µg/mL	in PBS buffer pH=7.0
BSA	0.1%	in PBS buffer pH=7.4
NA	Several concentrations	in PBS buffer pH=7.4
StrMPs-bioAb ₂ -bioHRP	20 µL 5 µg/mL 50 µL 30 µL of 2.5 mg/mL 10µL is diluted 1:50	in 0.1% BSA PBS buffer pH = 7.4 (incubated for 30 min)

As Figure 34 shows, this approach increases the detection limit and the sensitivity of the sensor very significantly. From the calibration plot (Figure 35) we obtained a sensitivity equal to 1.98 nA-mL pg⁻¹, i.e., ~3 times larger than using the conventional immunosensor; the detection limit was 0.1 pg/mL, i.e., ~250-fold better than the value of 25 pg/mL using the conventional immunosensor.

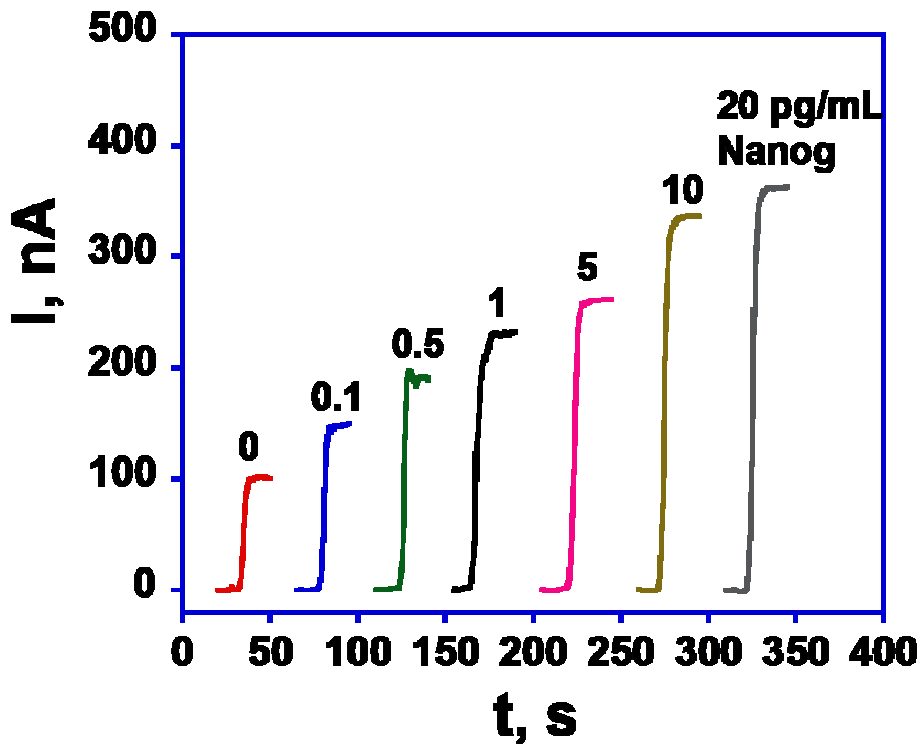


Figure 34. Amperometric results of the twelfth approach (for the sake of better comparison the curves have been arbitrarily shifted).

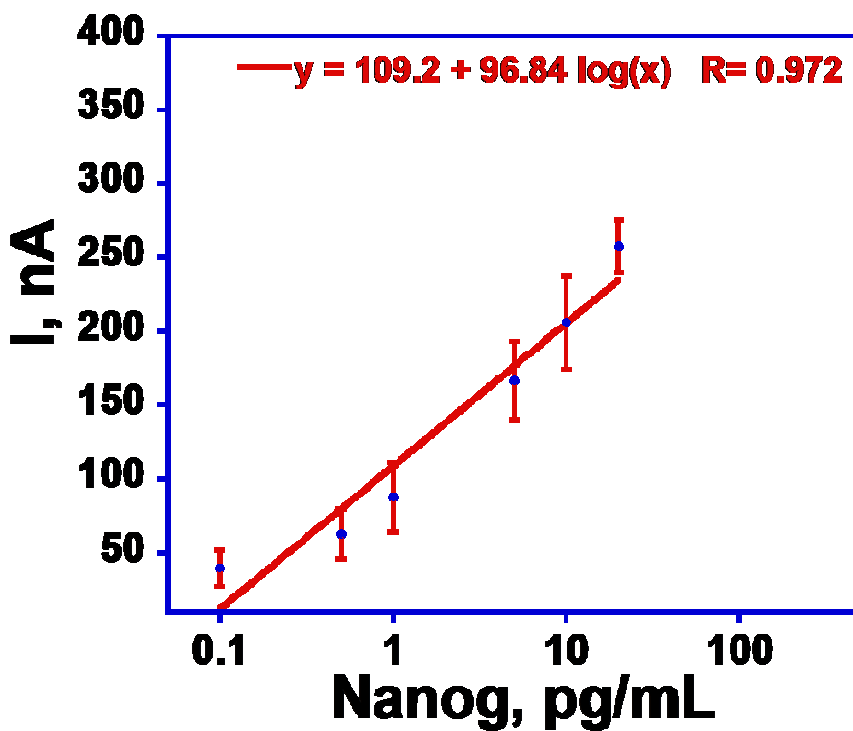


Figure 35. Immunosensor calibration plot for Nanog using the twelfth approach.

At this point, to better control and automate sample introduction, as well as steps such as washing, reagent addition, and the amount of H_2O_2 injected, we decided to take the sensor experiment to the microfluidic system.

In microfluidics, the mechanism is similar to that of the rotating-disk electrode, the main difference being that in this case the eight-electrode array is stationary while the HQ solution continuously flows into the microfluidic channel at a determinate speed rate (100 $\mu L/min$). By taking advantage of this mass transport regime, H_2O_2 , once injected, can reach the sensor array and oxidize the enzyme peroxidase. Figure 36 shows a schematic representation of the microfluidic system.

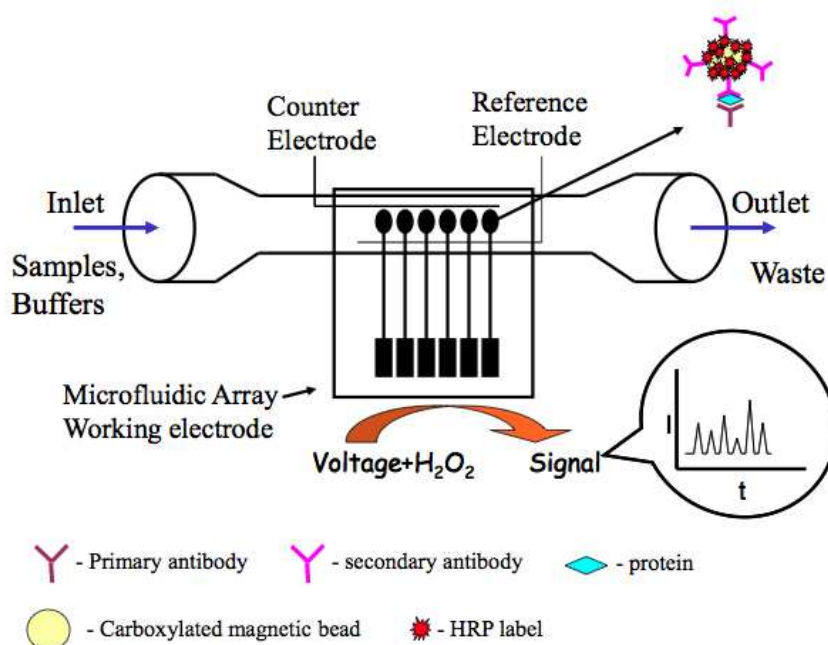


Figure 36. Schematic representation of microfluidic system

The intensity of the amperometric current is proportional to the concentration of NA, and the width of the peak is proportional to the speed rate of the flux. Figure 37 shows one representative example of measurement employing an eight-electrode array. The Nanog concentration was 1 pg/mL. As we can see, the current does not reach a steady state, as with the rotating-disk electrode method, but increases until reaching a maximum value and then decreases in time because the concentration of hydrogen peroxide decreases due to the constant flux of the fluid.

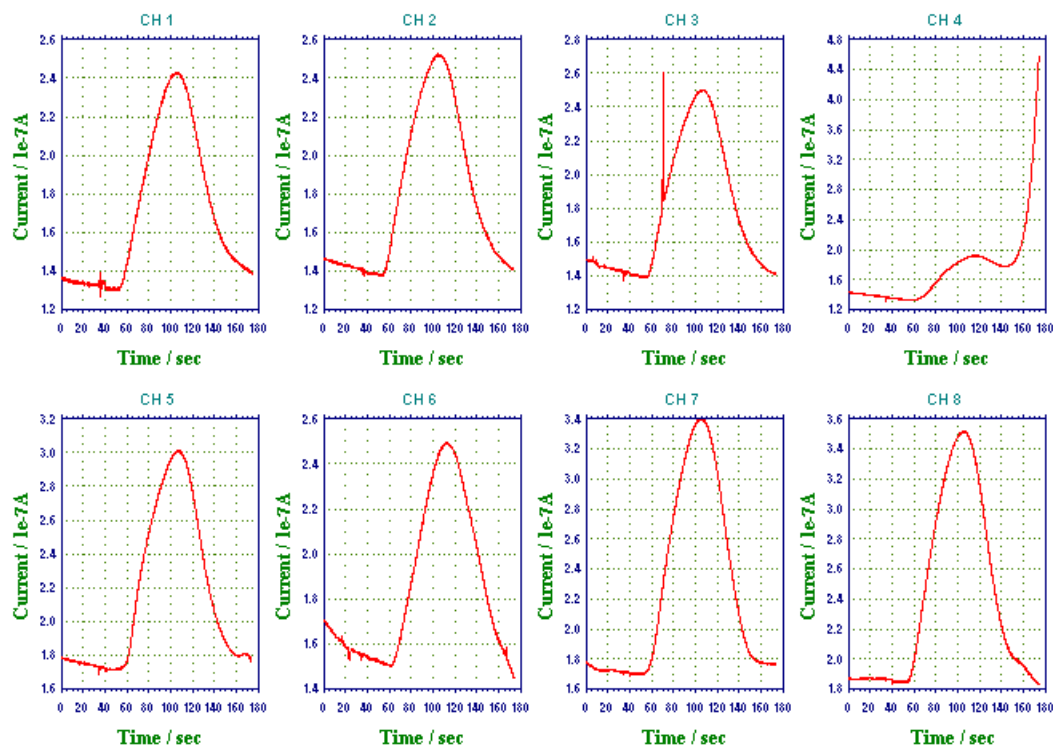


Figure 37. Amperometric results of 1 pg/mL eight-electrode array using the twelfth approach.

This was the last result obtained concerning this optimization process. Further measurements are currently being carried out at the University of Connecticut. Among them, to obtain a “microfluidic” calibration curve similar to that of Figure 35 and the use of different NA concentrations in the eight electrodes.

The results described above demonstrate the utility of gold nanoparticle-based immunosensors combined with amplified multilabel detection using magnetic beads for ultrasensitive detection of protein biomarkers. Since a significant number of biomarkers have normal levels in the low pg/mL range, we here wished to demonstrate how to improve the detection limit in this range in order to optimize a sensor capable of measuring both normal (=low) concentrations representative of cancer-free patients and elevated levels indicative of cancer. The approach utilizing StrMPs-bioAb₂-bioHRP conferred the best sensitivity and the best detection limit due to the high number of labels on each magnetic bead. Other advantages of the magnetic beads for multiple labeling

include a more narrow and reproducible size distribution than other methods and ease of preparation of the labeled bioconjugates, featuring magnetic separation of MPs-Ab₂-HRP from unbound proteins by using a magnet.

The increased density of the conductive AuNPs greatly increases the active surface area for capture antibody attachment to flexible glutathione tethers and may also be an important factor explaining the improved sensitivity. The key advantages for higher amperometric signal include densely packed, patternable conductive nanoparticles resulting in a high surface area, highly conductive platform with protruding functional groups that allow simple bioconjugation to large amounts of primary antibodies. The immunosensors required mediation for the best sensitivity and this is most likely related to the distance between the HRP labels and the AuNPs, which limits the efficiency of direct ET.

The improvement in detection limit may be also related to better control of mass transport in the microfluidic system compared to the rotating-disk electrode approach, leading to better signal-to-noise. The microfluidic biosensor also showed good stability and reproducibility.⁹ In general, the advantages of microfluidics are: i) small volume required [μL , nL] (very important for expensive reagents and to reduce waste); ii) faster response (reaction time is fast, shorter diffusion distances); iii) high sensitivity and detection limits; iv) inexpensive method; v) less energy consumption; vi) capability of rapid multiplexed protein detection; vi) portable and user friendly; vii) operationally simple; viii) ideal for point of care diagnostics.

To conclude, this method should be readily adaptable to measure cancer biomarkers having very low normal levels in serum and tissue, for point-of-care early detection and monitoring of this disease.

3.2 IRRAS Characterization of Peptide SAM

Infrared reflection absorption spectroscopy (IRRAS) is a useful technique for studying thin films on reflective substrates. A study of the infrared absorption spectra of adsorbed molecules may provide detailed information about the

structure of the adsorbed species, the nature of the interaction with the surface, and the strength of the adsorption forces.

3.2.1 The metal-surface selection rule

The IRRAS technique differs from normal IR spectroscopy for a particular effect given by the reflection of the beam on a surface. Infrared radiation is a transverse, electromagnetic wave characterized by the orthogonal electric and magnetic fields oscillating in directions perpendicular to the direction of the wave propagation. Figure 38 shows a graphical representation of an electromagnetic wave with the electric field oriented along the y axis. Such a wave, with a well-defined orientation of the electric and magnetic fields, describes a linearly polarized radiation and shows that a non-polarized radiation can be regarded as composed of two orthogonal, linearly-polarized components. The energy of the magnetic field is equal to the energy of the electric field of an electromagnetic wave and thus it is convenient to consider only one field, usually the electric one. When the electromagnetic radiation is incident at a boundary between two phases, part of the beam is reflected and part of it is refracted into the second medium. The reflected light combines with the incident light to produce a standing-wave electric field at the metal surface, where the adsorbing monolayer is present.

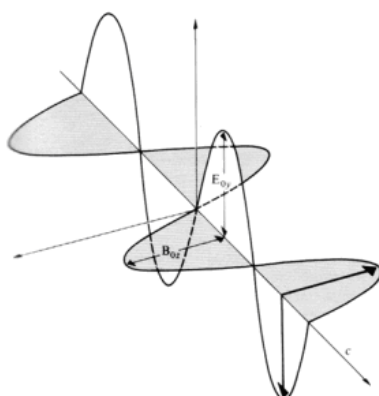


Figure 38. Direction of electric and magnetic fields with respect to the propagation direction of an electromagnetic wave.

This interaction between the incident and reflected light causes a phase change in the electromagnetic radiation that depends upon both the angle of incidence and the state of polarization of the light. Figure 39 shows the typical reflection phase shifts expected for a metal. The phase shift for the component polarized perpendicular to the plane of incidence (s-polarized electromagnetic radiation) is close to 180° for all angles of incidence, while the phase shift for the component polarized parallel to the plane of incidence (p-polarized electromagnetic radiation) changes rapidly at high angles of incidence. The plane of incidence is defined as the plane that contains the incident and reflected beams.

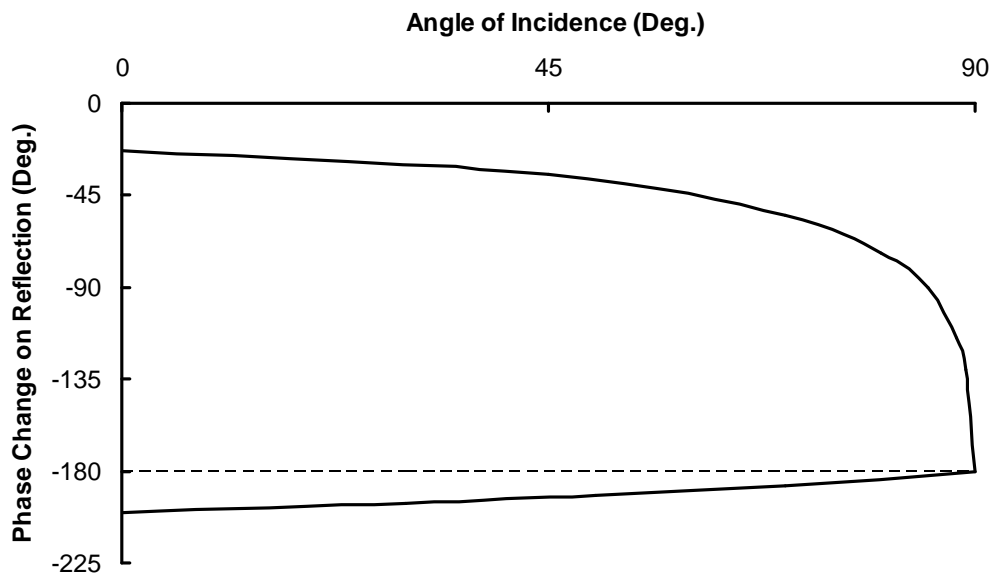


Figure 39. Phase shift for light reflected from a metal surface. $\delta_{||}$ is the phase shift for light polarized parallel to the plane of incidence; δ_{\perp} for light polarized perpendicular to the plane of incidence.

Figure 40 shows the plane of incidence profile of a boundary formed by a transparent and an absorbing phase. The coordinate system has the x and z axes in the plane of incidence and the y axis normal to the plane of incidence. The propagation directions of the electromagnetic radiation are indicated by dashed lines. The figure shows that the incident beam can be envisaged as composed of the two linearly polarized orthogonal components: s and p.

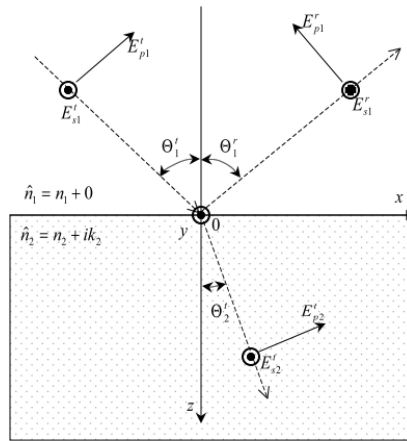
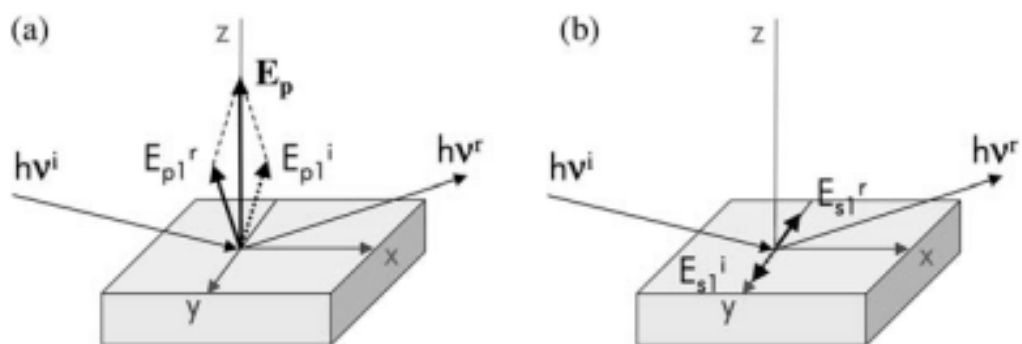


Figure 40. Reflection and refraction of electromagnetic radiation at the boundary between a transparent and an absorbing medium. Dashed lines denote the direction of propagation of radiation. Arrows indicate the electric field vector of p-polarized light, which lies in the plane of incidence. Symbols \odot and \ominus indicate the advancing and retreating electric field vectors of s-polarized radiation (which is perpendicular to the plane of incidence). In addition, symbol \odot shows the (advancing) direction of the y coordinate axis.

Figure 41, instead, underlines the orientation of the electric field vectors of s- and p-polarized beams with respect to the metal surface for a high angle of incidence where the phase shift upon reflection is 90° . Due to destructive interference of the incident and reflected radiation near the metal surface, the electric field of the s-polarized infrared beam almost vanishes at the metal surface for all angles of incidence, while the electric field of the p-polarized beam is enhanced at the metal surface as result of the constructive interference. Note that at grazing incidence the phase shift is 180° even for the p-polarized component and, consequently, its incident and reflected electric vectors would cancel at the metal surface. In other words, a thin layer on a metal reflecting surface should show some absorption only for the light polarized parallel to the plane of incidence and for a sufficiently high value of the angle of incidence, but not too high, otherwise even the p-polarized component undergoes to a destructive interference.

By considering these issues, the IR spectrum for a chemisorbed molecule may substantially change from that of the same molecule in solution or gas phase. Because of the reflection, only those modes that have vibrational dipole moments with components perpendicular to the metal surface will have measurable intensities. Whereas these normal modes are IR active, the normal modes whose dipole moment is parallel to the metal surface are IR inactive. This selection rule characteristic of the reflection adsorption spectroscopy is called “metal-surface selection rule”. Finally, differences in the IR spectra are also expected for a substantial change in the degrees of freedom of the chemisorbed species due to the bond between the molecule and the metal surface. It is well known that an N-atomic molecule in the gas phase has $3N$ kinetic degrees of freedom, for a nonlinear molecule 3 of these are translational, 3 are rotational and $(3N-6)$ are vibrational modes; for linear molecules there are 3 translational, 2 rotational and $(3N-5)$ vibrational modes.



p - polarized radiation:

electric field oscillates in the plane of incidence
 phase shift after reflection = 90°
 constructive interference
 enhancement of electric field at the metal surface

s - polarized radiation:

electric field oscillates perpendicular to the plane of incidence
 phase shift after reflection = 180°
 destructive interference
 vanishing of electric field at the metal surface

Figure 41. Diagrams of reflection of linearly polarized electromagnetic radiation by a metal mirror for a grazing angle, showing the interaction of s- and p-polarized beams with the metal surface.⁹⁸

For each non-degenerate vibrational degree of freedom, there is a normal mode in which all atoms vibrate with the same frequency. However when an N-atomic molecule is chemisorbed on a solid a new chemical bond is formed between the molecule and the surface and the adsorbed species is held with a greater extent of rigidity. This leads simultaneously to a substantial rearrangements of the bonding pattern between the atoms of the original adsorbed molecule and, hence, to a changed of the $(3N-6)$ "internal" vibrational frequencies. In addition, the three translational and the three rotational motions of the free molecules are usually converted to vibrational modes arising from the presence of the new chemical bonds. These new modes may become substantially mixed with the modified internal vibrations of the adsorbed molecule. Therefore, it is generally strictly meaningful to speak of a total of $3N$ new modes associated with the system of adsorbate plus adsorbent. In some cases, the torsional mode of the chemisorbed species may be approximate to a free rotation of the molecule around the new bond formed; then, there will be $(3N-1)$ new vibrational modes. In addition to changes in the degree of freedom of the molecule, new modes of vibration can arise from the coupling between the vibrations of the chemisorbed species and the lattice modes of the surface. This particular coupling can add other $3N$ vibrational degrees of freedom.⁹⁹

3.2.2 Characterization of Aib-Homopeptides

Before addressing the actual IRRAS measurements carried out on the peptide SAMs prepared on well activated and characterized gold surfaces (see Experimental), it is important to assess and comment the IR spectroscopy features of the free peptides in solution.

The FT-IR absorption spectra of the thiolated Aib-peptides, S-protected by the trityl (Trt) group, were obtained in CH_2Cl_2 , which is a solvent of low polarity having no propensity to behave as a hydrogen-bond acceptor. The analysis was focused on the N-H and amide stretch modes.

The N-H stretch region (Amide A region, ranging from 3500 to 3200 cm^{-1}) is composed by a high-energy region corresponding to the NH groups that are not involved in hydrogen bonds and a low-energy region pertaining to NH groups

involved in intra- and inter-molecular hydrogen bonds (Figure 42 and 43). The amide region ranges from 1700 to 1500 cm^{-1} and contains two main signals: the one higher in energy is called Amide I and is principally related to the stretch of the C=O groups. The other, lower in energy, is called Amide II and is more complex with an important contribution from N-H bending and C-N stretching vibrations (Figures 44 and 45).¹⁰⁰⁻¹⁰¹

As we can see in Figures 40 and 41, for both the plus and minus series there is a red-shift of the Amide I signal, as the peptide chain is made longer, as previously reported for similar peptide series by Toniolo et al.¹⁰⁰

In particular, these authors found that this red-shift is optimized with the octamer because of formation of a fully developed, stable intramolecular H-bond network. Interestingly, we can observe a shoulder in the amide I of *I-* at high energy. It thus appears that while for the *I+* the H-bond is more stable and the signal is prevalently related to the H-bonded C=O stretch, in the minus series the H-bond is weaker and the C=O component not involved in such interaction is more evident.

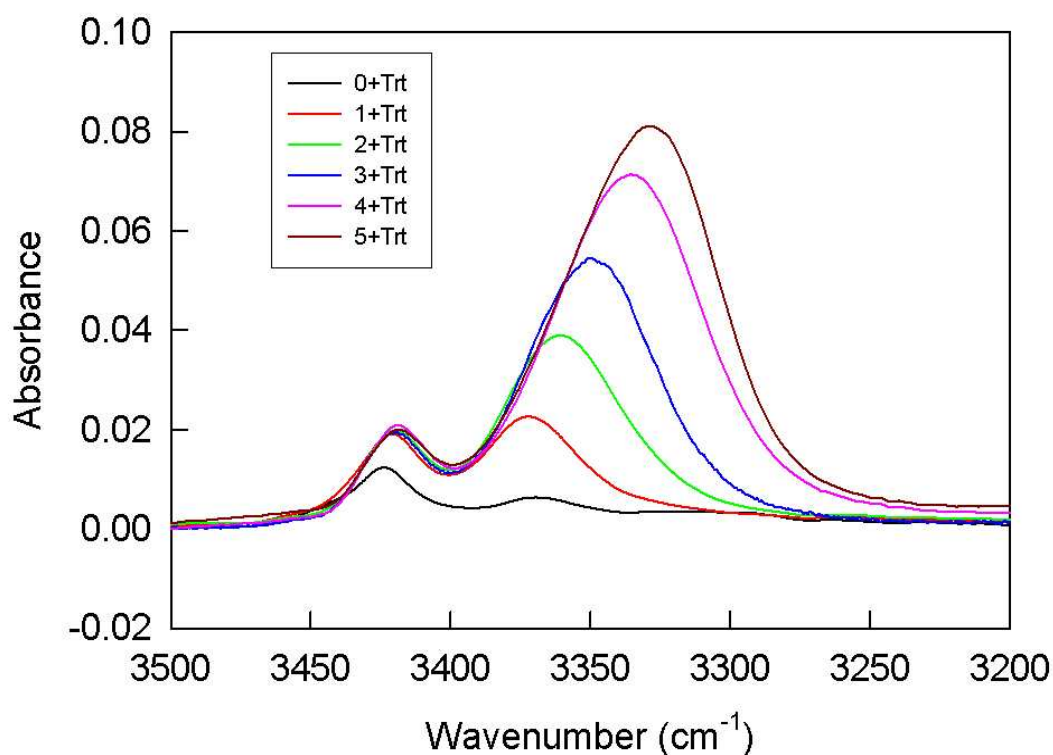


Figure 42. The amide A region for the plus series.

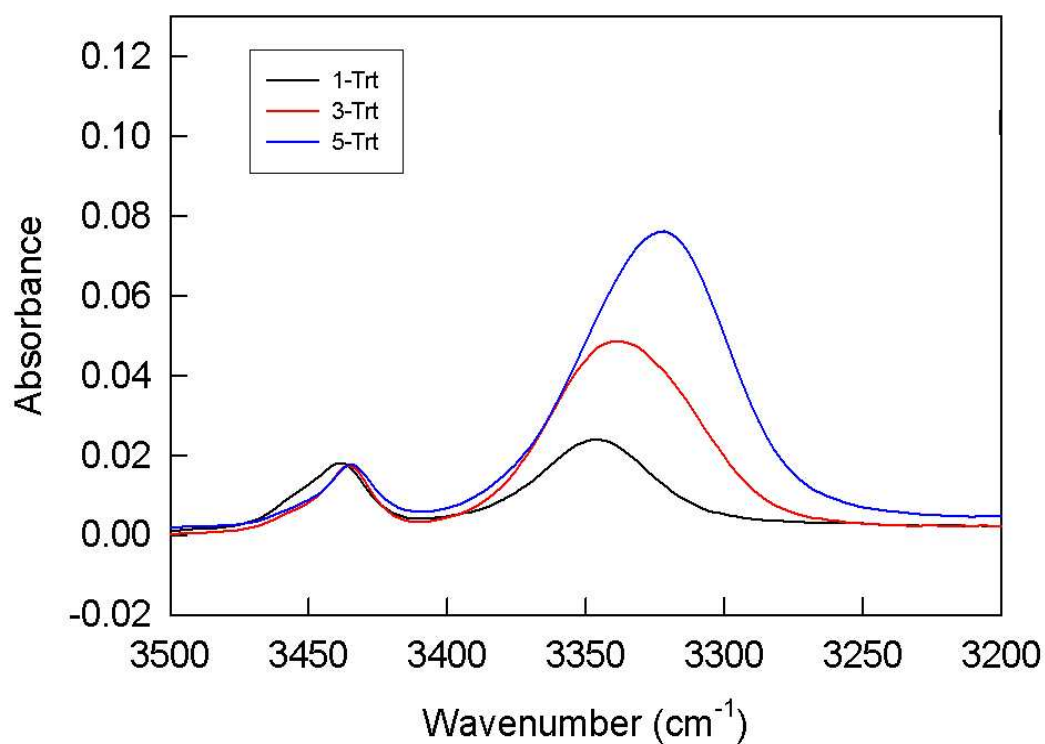


Figure 43. The amide A region for the minus series.

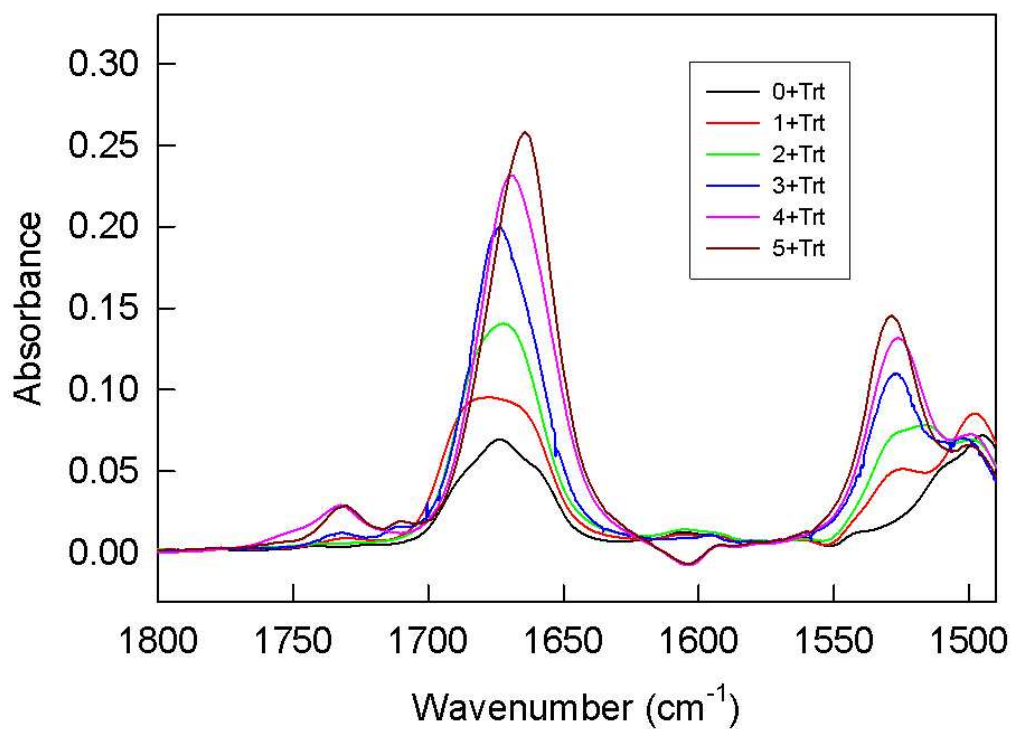


Figure 44. Amide I and amide II regions for the plus series.

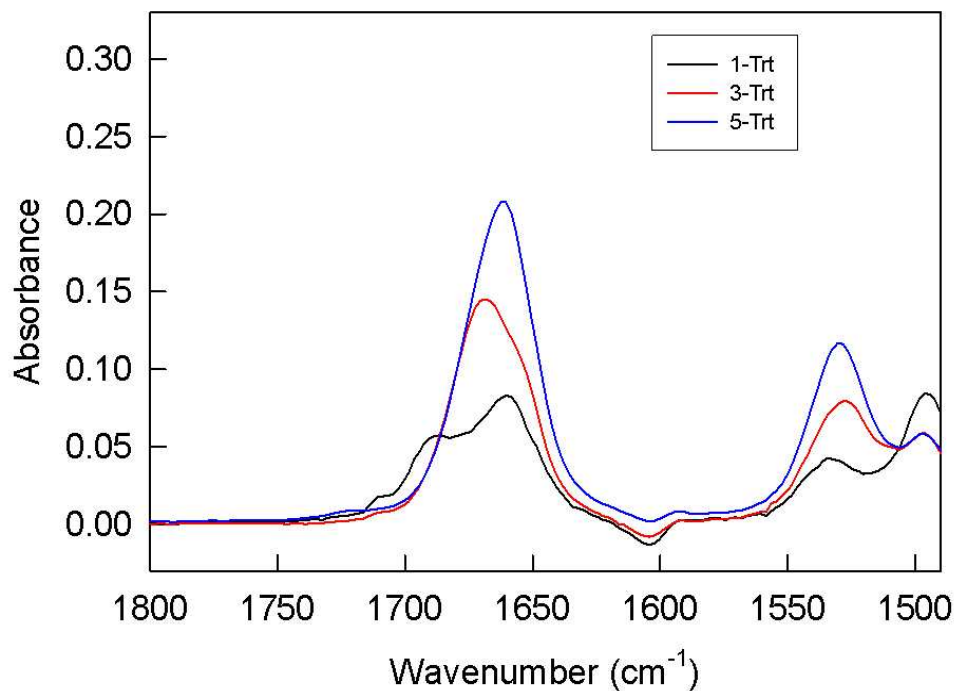


Figure 45. Amide I and amide II regions for the minus series.

Concerning the amide A region (Figure 42 and 43), there are two signals: a less intense signal at higher frequency and a more intense one between 3350 and 3300 cm^{-1} . The first is related to free N-H groups. According to the 3_{10} -helix features, two N-H and two C=O groups are not involved in intramolecular H-bonds, as highlighted in Figure 46. As reported by Toniolo et al.¹⁰⁰, the intensity of the band related to the stretch of the N-H bonds involved in intramolecular H-bonds increases as the peptide is made longer. The red-shift of the band tends to become independent of the peptide length for sufficiently long peptides, meaning that the 3_{10} -helix is fully formed and stable. With our systems, we observed the same intensity increase and red shift. The intensity of the band related to the free N-H groups does not change because the number of those groups (two) does not vary with the peptide length.

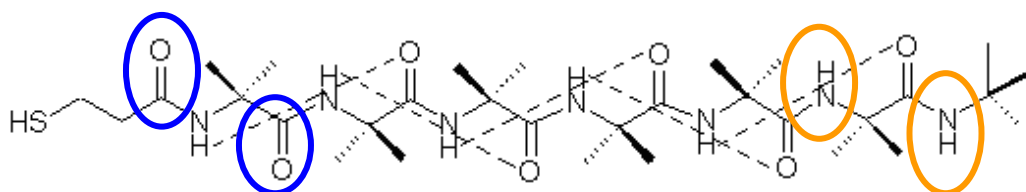


Figure 46. The C=O and the N-H not involved in the intramolecular H-bonds (plus series) are circled in blue and orange, respectively.

To verify the extent of stability of the 3_{10} -helices formed by the peptides of the plus and minus series, we applied the same analysis previously described for these systems. The ratio between the integrated intensity of the band of H-bonded N-H groups to free N-H groups, divided by the number of actual H-binds, should display a dependence of on the number of intramolecular H-bonds that tends to level off for sufficiently long peptides: this is an indication of formation of stable and stiff 3_{10} -helices.¹⁰⁰

Figure 47 compares the results obtained with the plus and minus series in comparison with the data previously reported for $Z\text{-(Aib)}_n\text{-OtBu}$ ($Z =$ (benzyloxy)carbonyl, OtBu = tert-butoxy, $n = 3\text{-}11$).¹⁰⁰ If the values at large H-bond values are taken as a reference, one can estimate how the percentage of intramolecular H-bonds changes as the peptide is made longer. This is illustrated in Figure 48. The shorter oligomers, as expected, display less stability but for longer peptides of the investigated series we can conclude that the helices are essentially fully formed, which implies stiffer peptides.

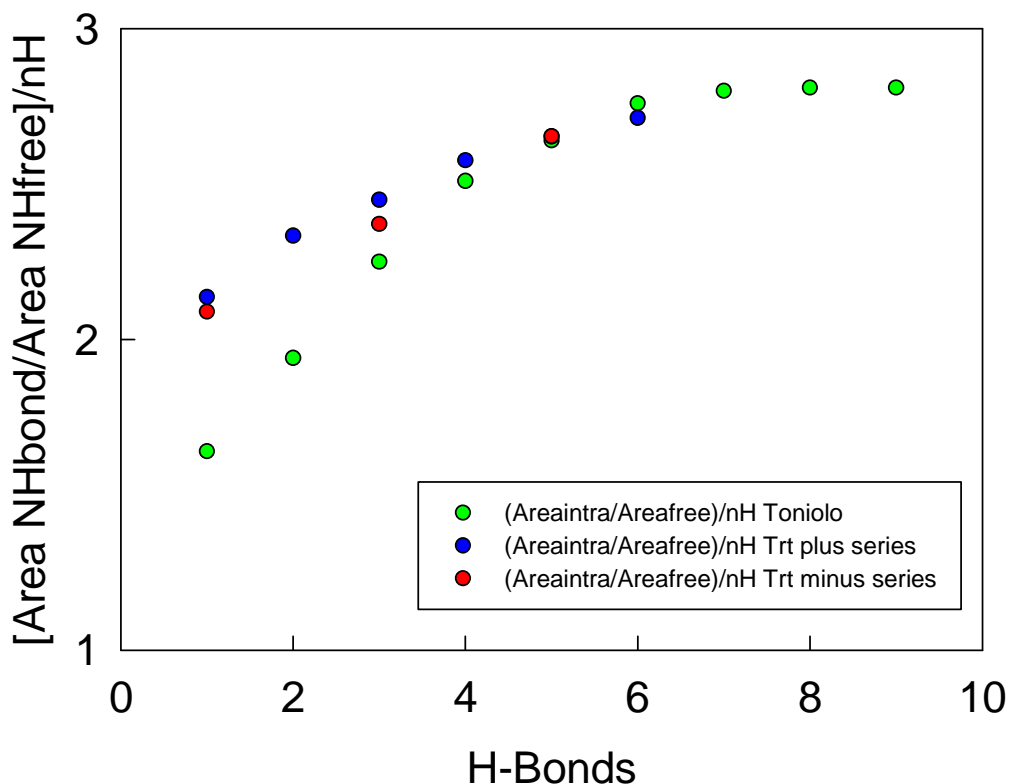


Figure 47. Dependence of the normalized ratio between the integrated intensity of free and intramolecularly bonded N-H groups on the number of H-bonds (for explanations, see text).

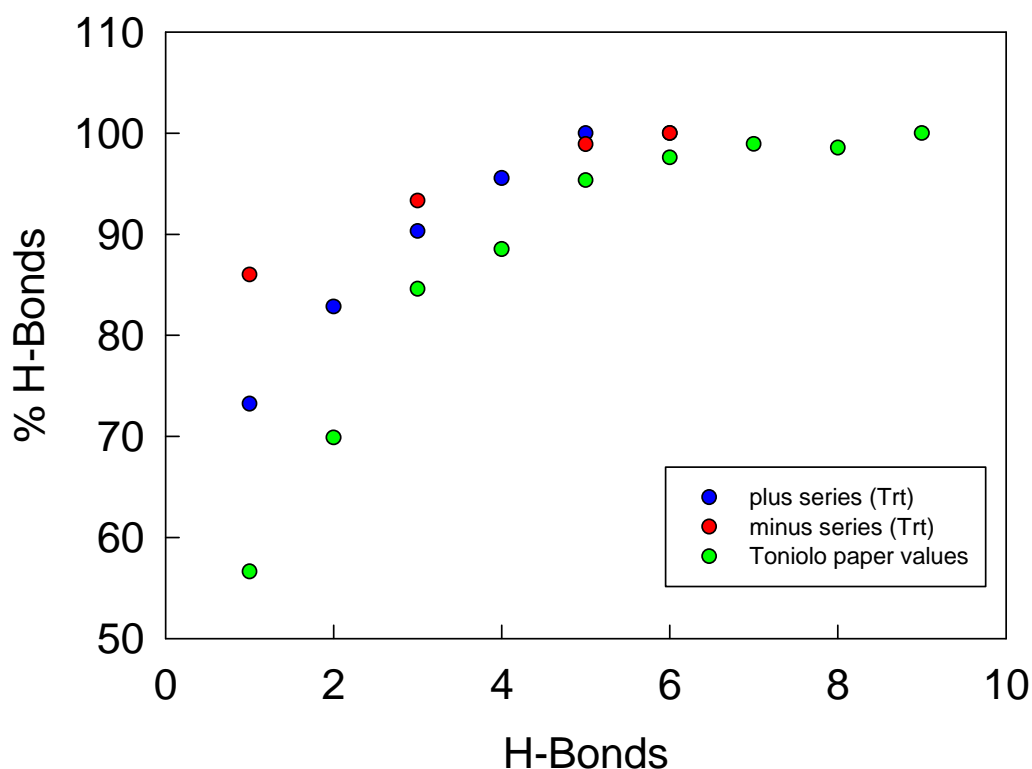


Figure 48. *Dependence of the peptide stiffness on the number of H-bonds.*

We should finally note, however, that the FT-IR technique alone does not allow one to unequivocally establish the specific helical structure adopted by the peptides. Full assessment also requires extensive characterization by NMR spectroscopy. For the peptides here investigated, this aspect was previously dealt with, and will not be discussed further.⁸³ Here, it suffices to stress that the presence of the 3_{10} -helical structure was fully confirmed for most of the peptides here investigated.

3.2.3 Characterization of Aib-Homopeptides SAMs

Vibrational spectroscopy is a powerful technique for studying peptide structures and interactions. In the previous section, we discussed the IR absorption behavior of the free (protected) thiolated peptides and, particularly, how the N-H stretch region (amide A) allows us to distinguish between the N-H groups that are involved in intramolecular hydrogen bonds and those not involved in such interactions. We also saw that other important information on the 3_{10} -helix

structure and stability can be obtained from the amide I (and amide II) region. IRRAS spectroscopy was utilized to obtain information on the structure of the peptide SAMs and to further investigate their stability. In fact, the same information provided from FTIR of free ligands can be obtained from the position and intensity of the IRRAS peaks. In addition, information on the organization of the monolayer can be gathered by taking advantage of the metal-surface selection rule.

The two series of peptides, self-assembled onto carefully annealed gold surfaces (see Experimental) were thus studied by IRRAS; the spectrum of $0+$, however, could not be satisfactorily analyzed because of its weak signals. Figure 48 shows the full spectrum of the SAMs formed from the peptides of the plus series. The presence of bands that clearly increase as the peptide length increases is evident. We will first comment the Amide A region, and then the Amide I and II regions.

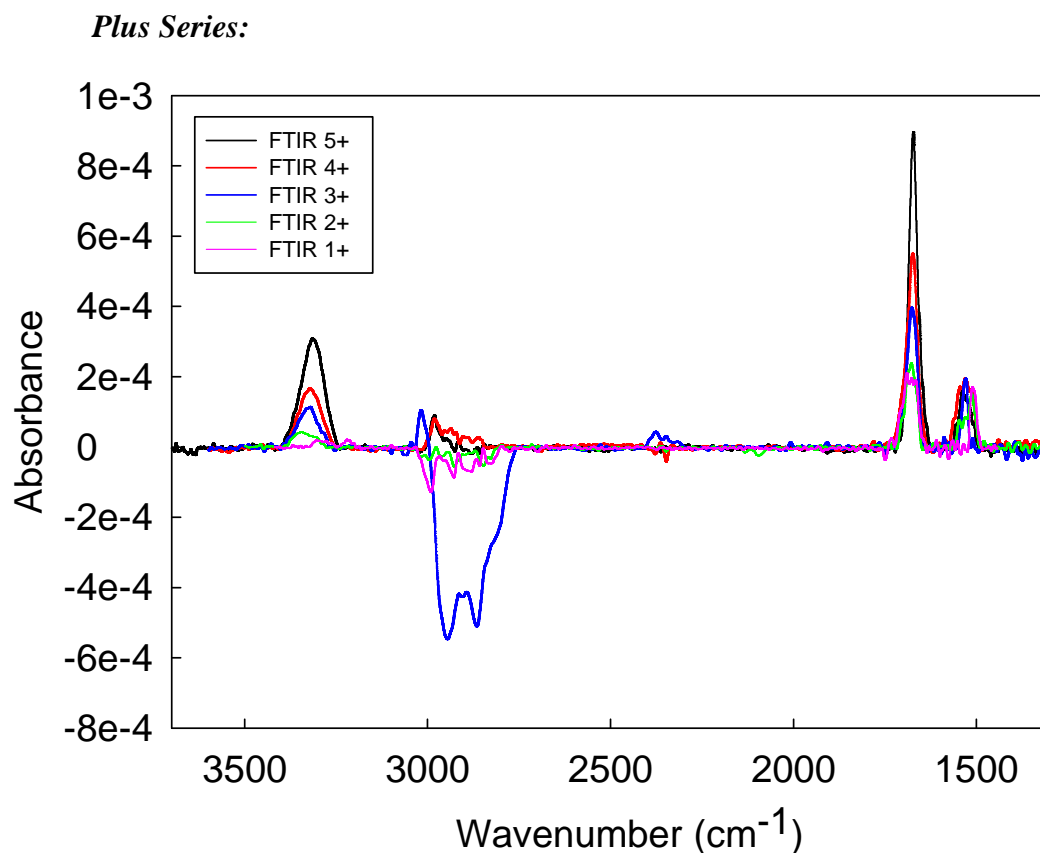


Figure 49. The FTIR-RAS spectra for the plus series correspond (bottom to top) to 1+ (pink), 2+ (green), 3+ (blue), 4+ (red), and 5+ (black).

Hydrogen bonding and the coupling between transition dipoles are among the most important factors governing conformational sensitivity of the amide bands.¹⁰⁰

The N-H stretch region, from 3200 cm⁻¹ to 3500 cm⁻¹, clearly shows (Figure 50), that compared to the free molecules the band corresponding to the two free N-H groups disappears, which means that all the N-H groups are bonded either intra- or inter-molecularly. In fact, we should consider that while in the SAMs the peptides are forced to organize close to each other. In this way, the free N-H are conceivably involved in intermolecular interactions and thus the high-frequency band disappears. This conclusion also implies that neighbor peptide adsorbates should provide C=O groups that are already involved in intrachain C=O...H-N hydrogen bonds. These three-center hydrogen bonds allow formation of a strong interchain bonding network and, since for the *plus* series they are embedded inside of the monolayer, they are largely unaffected by an increase of the peptide length, as already observed for the corresponding 3D SAMs formed on gold nanoclusters.⁸³

The Amide A region also shows that as the peptide chain length increases the frequency of the N-H stretch band of intramolecularly H-bonded peptides decreases, which is a marker of the increase of peptide stiffness (see Figure 51). As we discussed in the previous section, based on the work of Toniolo and coworkers one can relate the percentage of intramolecular H-bonds of the 3₁₀-helix type to the number of residues.¹⁰⁰

We applied the same treatment to the trityl-protected thiolated peptides of the *plus* series and could estimate that even with *I+* helicity is more than 70%, eventually becoming 100% for the longest peptide. These data highlight the outstanding efficiency of the Aib unit in stabilizing folded and helical species even in very short peptides, but also explain the broadness of the IR bands, which result from a combination of contributions from multiple conformations.⁸³

Since the helicity percentage requires to compute a factor including the integrated absorbance of the free N-H groups, this calculation cannot be applied to the peptides in the SAM. On the other hand, the very fact that the peptide is inside the monolayer implies less freedom degrees and thus the helix is expected to be even stiffer than in solution. This is also known for simple alkanethiols, where the

all-trans conformation is stabilized by Van der Waals interactions with neighbor molecules in the SAM.⁵⁶ We are thus confident that not only the 3_{10} -helix forms, as already inferred from the IR spectra of the free molecules in solution, but also that it is probably even stiffer.

From the comparison between the amide A band of the free peptides and those self-assembled on the gold surface, another interesting aspect emerges (see Figure 51). In general, we notice that the peptide-length dependence of the band maximum for the free (trityl-protected) peptides in solution and that for the self-assembled peptides is approximately similar. Figure 48 shows that the wavenumber of the amide A band for the *plus* series linearly decreases with an increase of the number of H-bonds. The main difference between the two series is an almost constant shift: the *plus* series of chemisorbed peptides is shifted toward lower wavenumbers by $\sim 4\text{ cm}^{-1}$. This is probably related to what said before: while in the SAM, the peptides are stiffer.

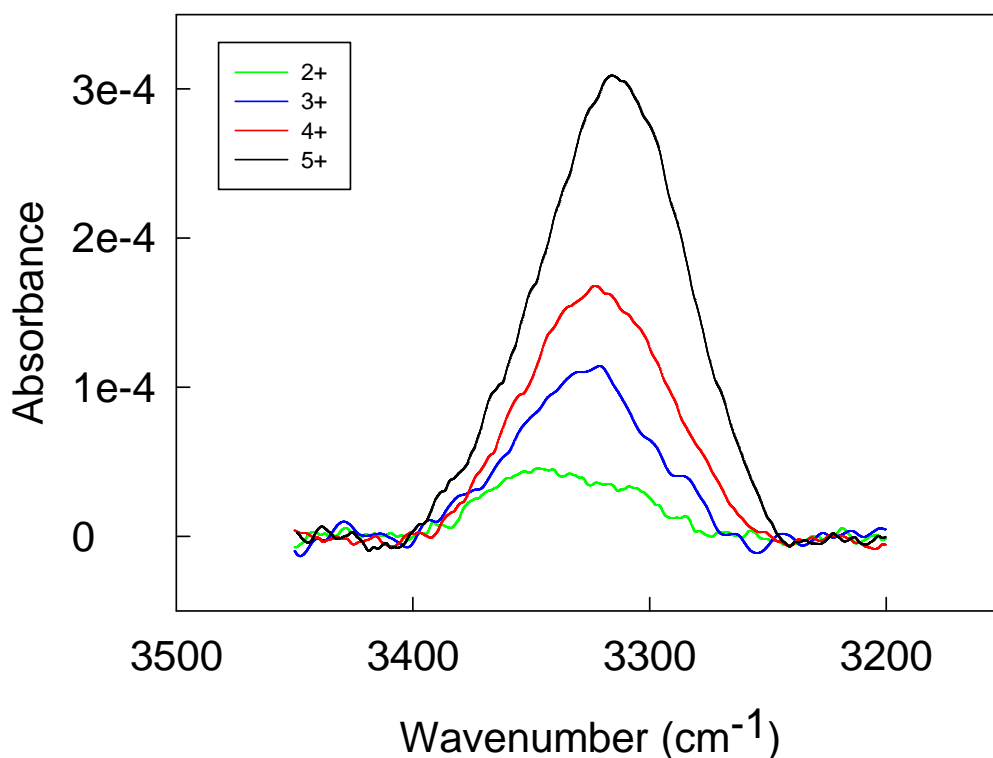


Figure 50. Amide A band for the peptide SAM of the *plus* series, with the only exception of *1+* because it had a different behavior, so it was treated later.

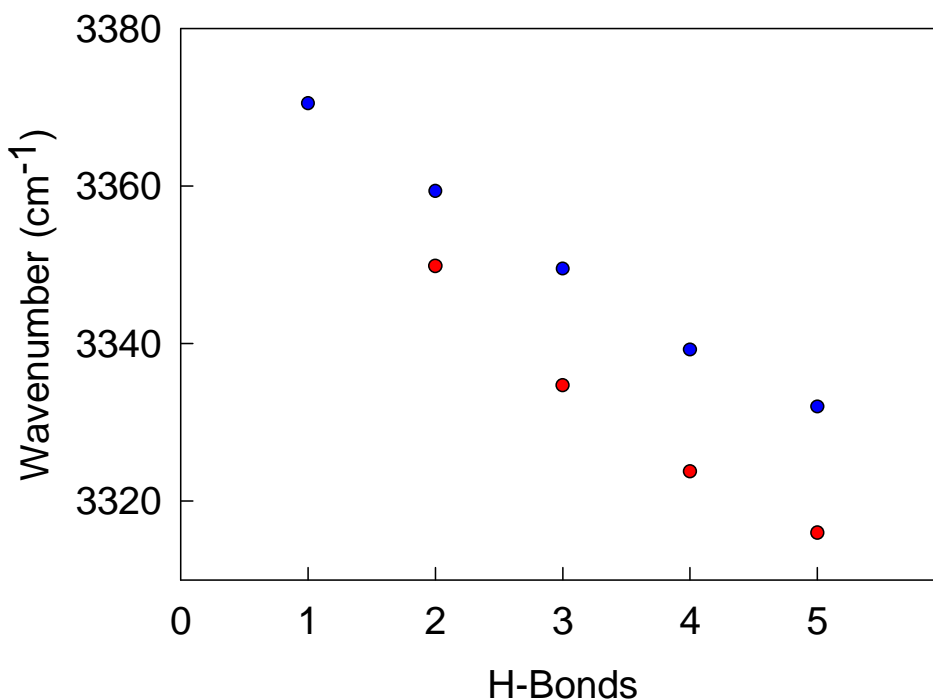


Figure 51. Comparison between the wavenumbers of the amide A band for the plus series of the free protected peptides (blue color) and for the plus series of the self assembled peptides (red color).

The band of 2+ shows the presence of two components. The low-frequency component appears to be present also when the peptide is made longer (the overall band is very broad), but the red shift of the main band prevents its detection for 4+ and 5+. The low-frequency component is typical of intermolecular H-bonds, as already found and discussed in detail with Aib-peptide protected gold nanoclusters.⁸³ We here made the assumption that the low-frequency component of 2+ is present for all peptides.

To better appreciate the relative similarities and differences, also in terms of absorbance maxima, we thus normalized the N-H stretch region (Figure 53) by taking into account the number of molecules per cm² (Table 4). These data were calculated using the average of the charge (μC) per cm² obtained in reductive desorption measurements.⁸⁹ By this approach, one can take into account the actual difference between the surface concentrations. In other words, the low-frequency band of 2+ could be normalized for the concentration and this value was subtracted from the normalized broad band of the other peptides. The contribution

of the N-H band of intermolecularly H-bonded peptides was obtained by deconvolution^{89b} of the spectrum of **2+**, as illustrated in Figure 52.

Table 4: Values of Surface Coverage.

H-Bonds	Plus Series (mol cm ⁻²)	Minus Series (mol cm ⁻²)
0	$4.15 \pm 0.25 \cdot 10^{-10}$	-
1	$4.03 \pm 0.24 \cdot 10^{-10}$	$6.40 \pm 0.70 \cdot 10^{-10}$
2	$3.84 \pm 0.20 \cdot 10^{-10}$	-
3	$4.99 \pm 0.43 \cdot 10^{-10}$	$3.70 \pm 0.05 \cdot 10^{-10}$
4	$4.59 \pm 0.34 \cdot 10^{-10}$	-
5	$4.31 \pm 0.26 \cdot 10^{-10}$	$3.14 \pm 0.12 \cdot 10^{-10}$

This deconvolution clearly shows that the signal can be deconvoluted as the sum of two non-linear least square Gaussian fits, one due to the intramolecular bonds at 3349 cm⁻¹ and the other due to the intermolecular bonds at 3308 cm⁻¹. The latter frequency is as found with Aib-peptides protecting gold nanoclusters⁸⁹: in the end, we are comparing very similar systems, the main difference being that small Au clusters tend to be roughly spherical (3D SAM).

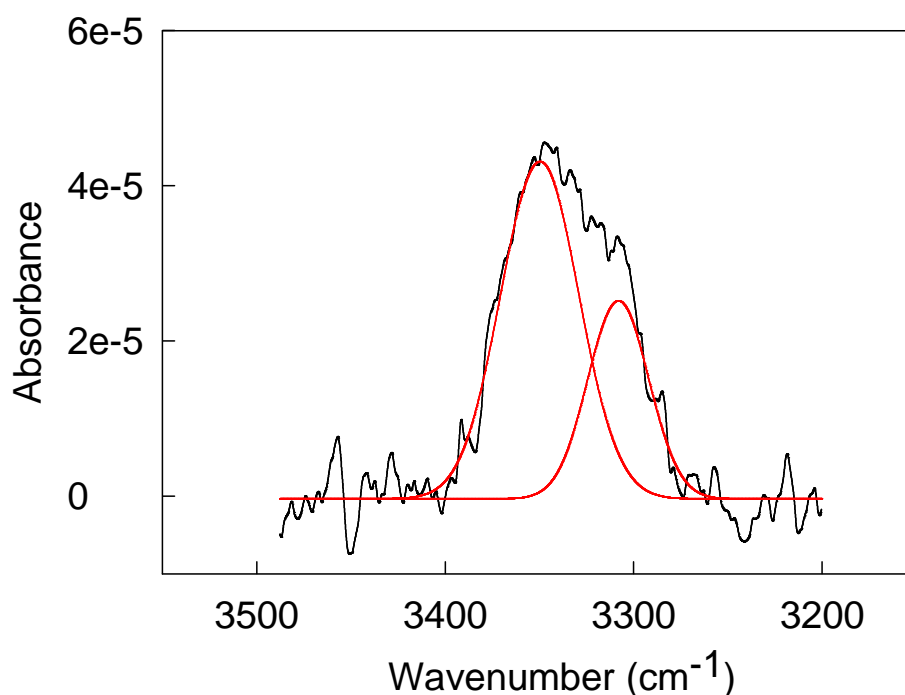


Figure 52. Deconvolution of amide A region of **2+**.

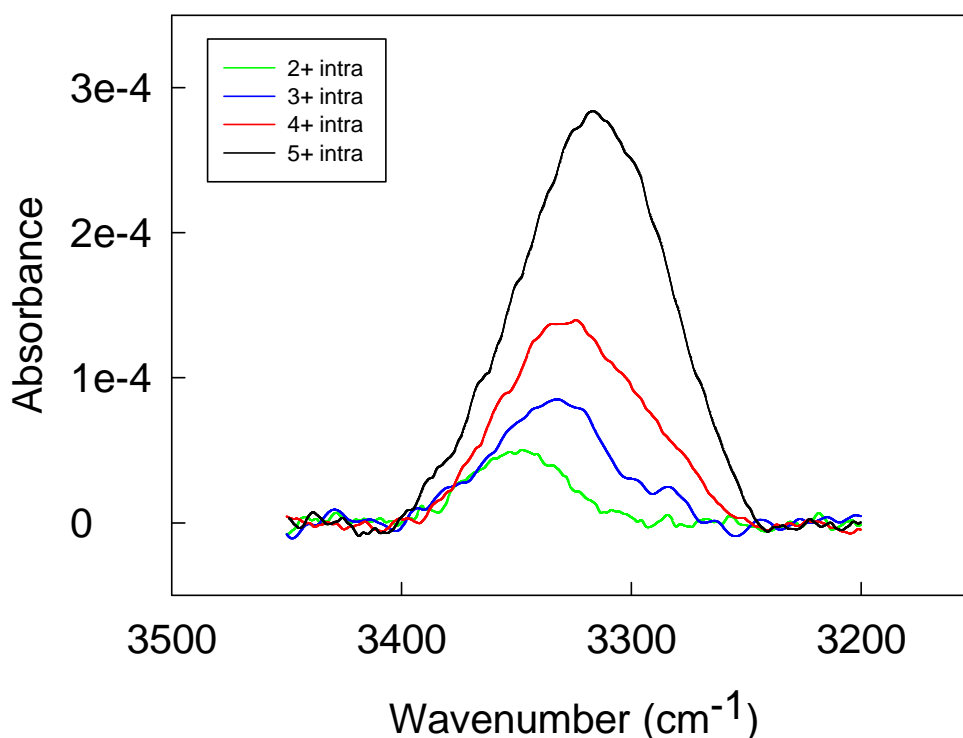


Figure 53. FTIR-RAS spectra for the amide A normalized by taking into account the concentration and the presence of the N-H band of intermolecularly H-bonded peptides.

As already noted, shorter oligomers exhibit in solution a small percentage of intramolecular H-bonds. In SAMs, on the other hand, the presence of neighbor molecules reduces the freedom degrees of each molecule and should thus make the helix more stable and stiffer. This is true for most Aib peptides. Notably, however, Figure 51 shows that the amide A band of *I+* does not have the classical signal related to an intramolecular H-bond (according to Figure 48, a band at $\sim 3360\text{ cm}^{-1}$ was predicted). Although weak, the only detectable bands are at lower energies. These frequencies are typical of intermolecular H-bonds, as already discussed. It appears, therefore, that when *I+* is self-assembled on a gold surface it undergoes a significant change of its secondary structure. The free energy of the system would thus be lowered when the intramolecular (3_{10} -helix like) H-bond is broken in favor of intermolecular H-bond(s).

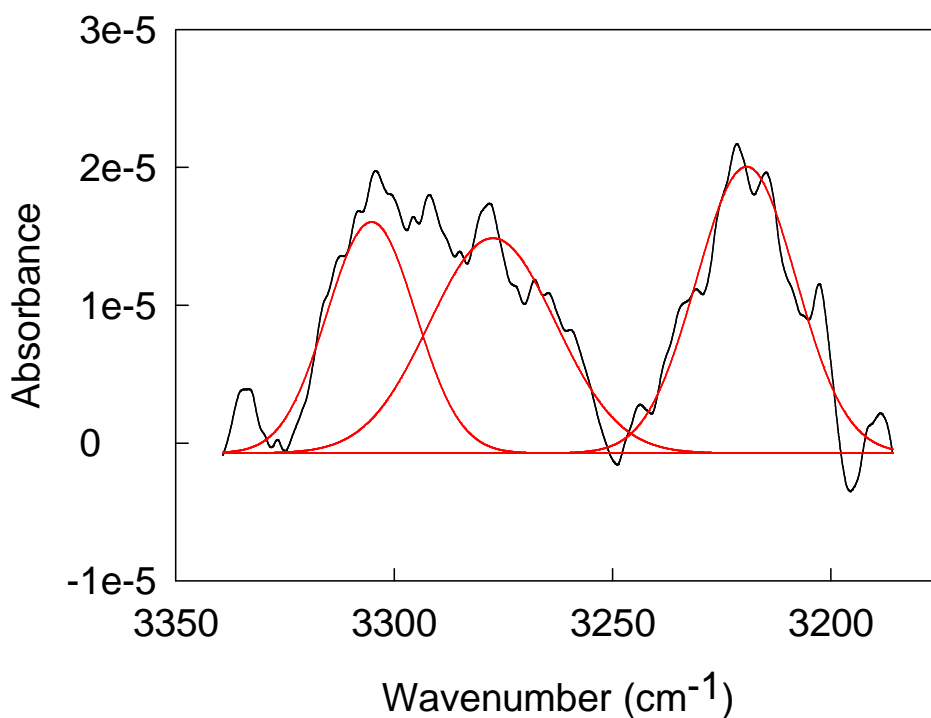


Figure 54. Deconvolution of amide A region of **1+**.

As already noted, information on the peptide conformation can be obtained from the amide I and II regions (Figure 55). We remind that the fine structure of these bands is quite complex because they are not pure modes but, instead, consist of several components. Let us focus our attention prevalently on the comparison of the two amide bands, the main reason being that from the ratio between the corresponding intensities the tilt of the peptide adsorbates can be estimated.

Whereas the intensity of the amide I band, which corresponds mostly to the C=O stretch and occurs at $1680 - 1672 \text{ cm}^{-1}$, increases with the number of residues for the plus series, the intensity of the amide II band, centered at $\sim 1530 \text{ cm}^{-1}$, is almost constant (see Figure 55). The main frequency is roughly constant for peptides **3+**, **4+** and **5+**, but the value decreases for peptides **1+** and **2+** (see Figure 56). The different sensitivity of the two bands on the peptide length are related to the metal-surface selection rules, according to which the transition moment related to the amide I band is more perpendicular to the surface, while the transition moment related to the amide II is only mildly affected.

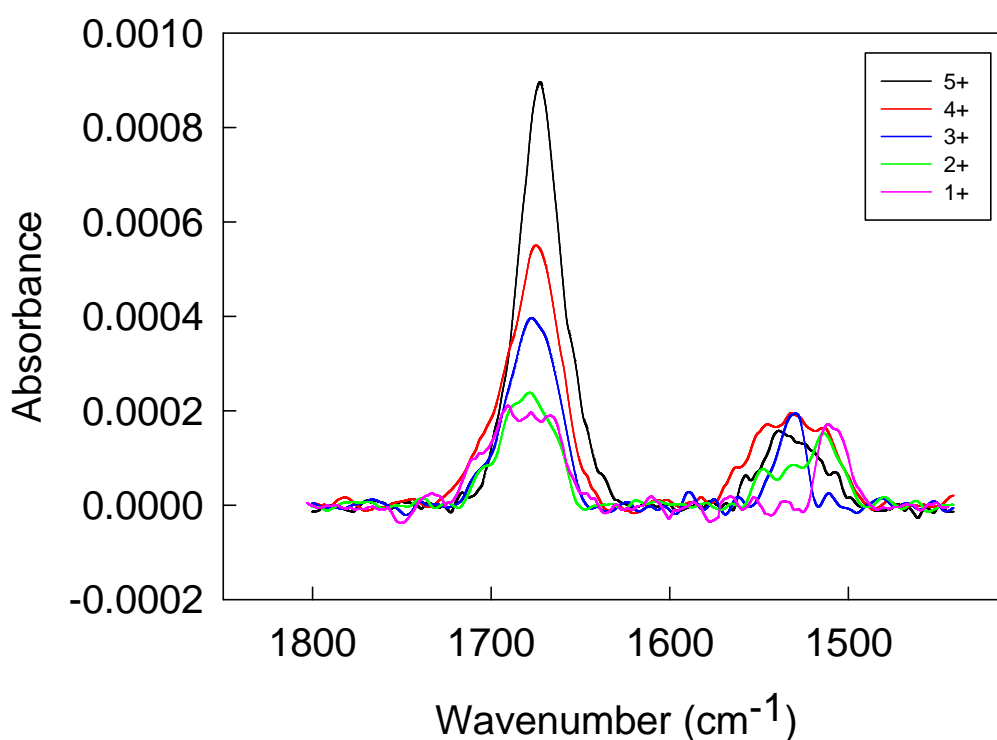


Figure 55. IRRAS spectra of the amide I and II bands for the plus series.

Concerning the Amide I band of the free and the SAM peptides (Figure 53), the frequency of the signal slightly decreases as the number of hydrogen bonds increases. This behavior is related to a progressive stabilization of 3_{10} -helix with an increase in the number of residues.¹⁰⁰ Unlike amide A, the amide I band of the self-assembled peptides is shifted by $\sim 4 \text{ cm}^{-1}$ to higher wavenumbers than in the corresponding free peptides. This behavior is quite intriguing because it would point to a less strong helical structure of the peptides while in the SAM. This is in contrast with the amide A behavior, the latter being easily understandable because of the reduced freedom degrees inside the SAM. At the present stage of investigation, we have no explanation of the different trend showed by the amide I data. As for the Amide A region, *I+* displays some different features from the other peptides of the plus series. This is evident from the shape of the amide I band (Figure 57) that is composed by more than one component. We will see that a similar complex situation is also displayed by *3-* and, particularly, *I-*. The complex pattern of the Amide I band confirms our initial hypothesis that when *I+* is self-assembled on a gold surface it undergoes a significant change of its secondary structure.

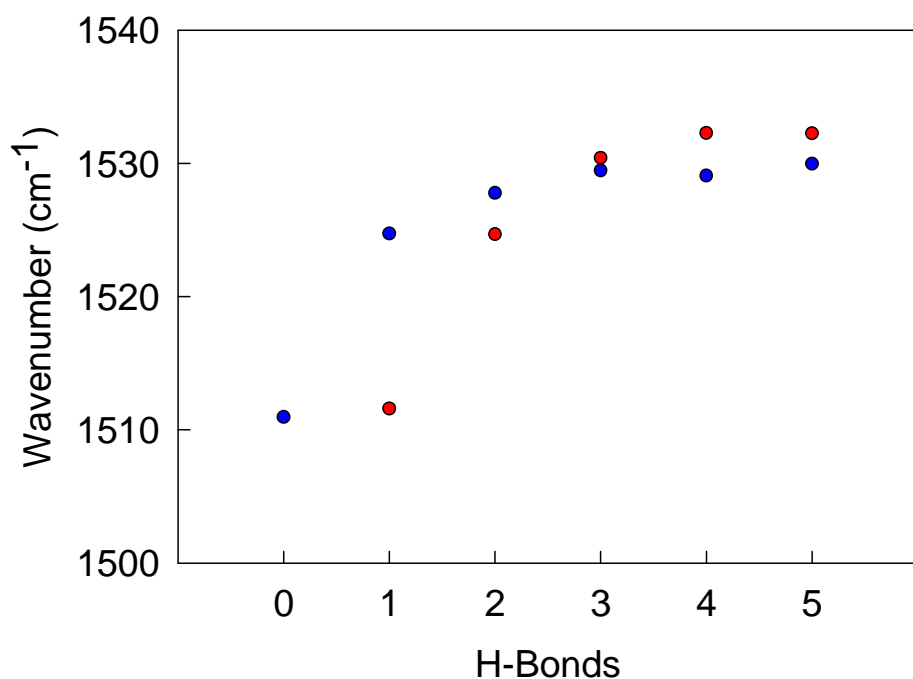


Figure 55. Comparison between the wavenumbers of the amide II band for the plus series of the free protected peptides (blue) and for the plus series of the self-assembled peptides (red).

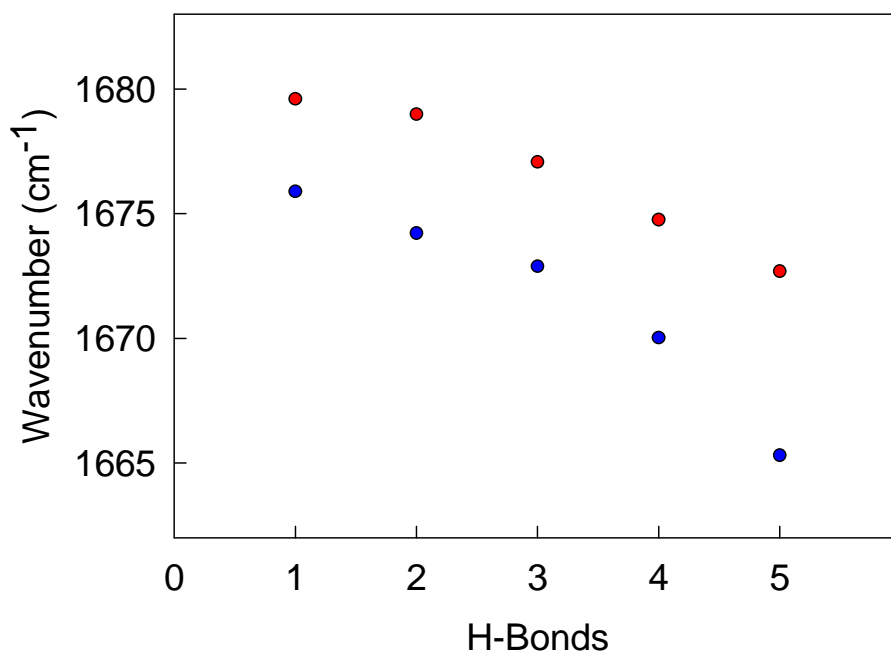


Figure 56. Comparison between the wavenumbers of the amide I band for the plus series of the free protected peptides (blue color) and for the plus series of the self assembled peptides (red color).

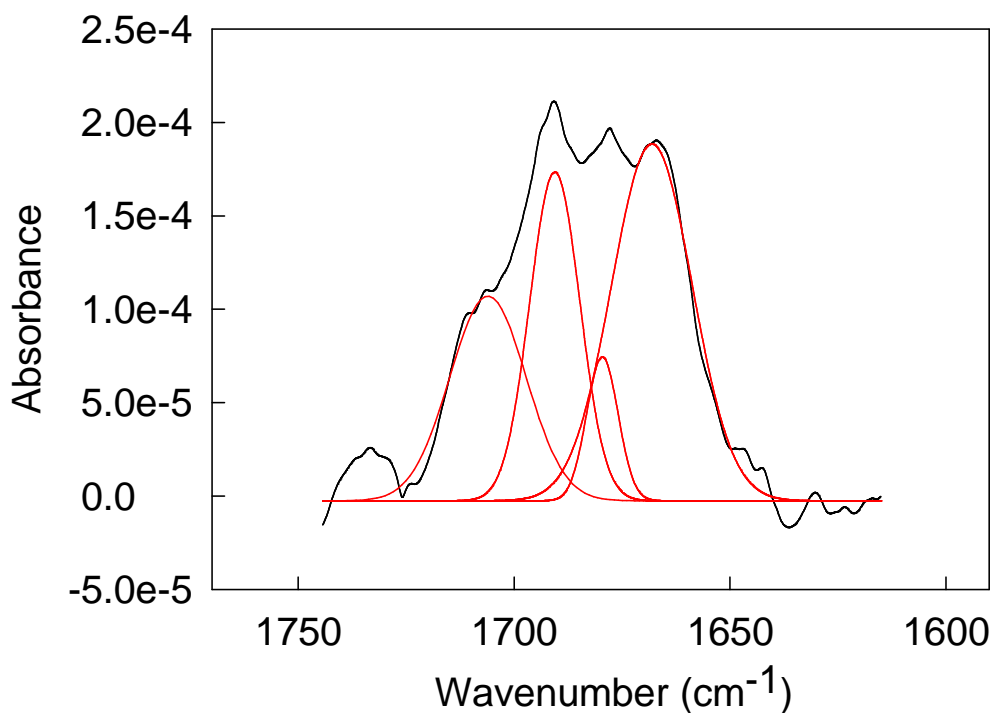


Figure 57. Deconvolution of amide I region of 1+.

The frequency of the main bands of the plus series, for both the Amide A and the amide carbonyl regions, are gathered in Table 5.

Table 5: Values of wavenumbers obtained for each peptide for the plus series.

<i>H-Bonds</i>	<i>Region</i>	<i>Wavenumber (cm-1)¹</i>
1	Amide I	1679.6 (1668.1, 1690.6)
	Amide II	1511.6
	Amide A	3305.2 (3219, 3277)
2	Amide I	1679.0
	Amide II	1524.7
	Amide A	3349.8 (3308.2)
3	Amide I	1677.1
	Amide II	1530.4
	Amide A	3334.7
4	Amide I	1674.8
	Amide II	1532.3
	Amide A	3323.8
5	Amide I	1672.7
	Amide II	1532.3
	Amide A	3316.0

¹ The frequency values obtained from deconvolution are in parenthesis.

Minus Series:

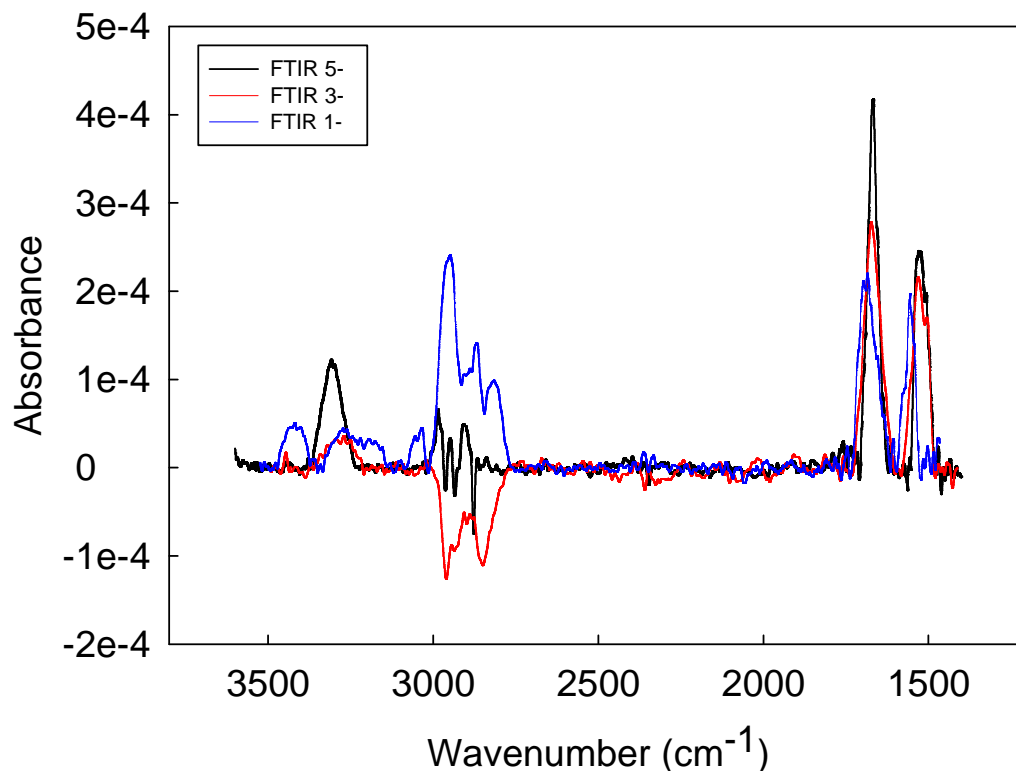


Figure 58. The FTIR-RAS spectra for the minus series correspond (bottom to top) to **1-** (blue), **3-** (red), and **5-** (black).

We now focus on the minus series. This series consistently displays absorbances significantly lower than those of the corresponding *plus* series. This is related to both a lower surface concentration (see Table 5) and other factors, as explained in the following.

The spectral region pertaining to the amide A band (Figure 59) shows that **1-** has a high-energy band in the region of free N-H bonds, and both **1-** and **3-** do not show the intramolecular band at the expected wavenumbers, but show a broad band at lower energies that most likely corresponds to the stretch of intermolecularly-bonded NH groups. We should mention, however, that for **3-** this behavior is less reproducible, as if for this peptide the SAM structure is very much dependent on the preparation of the SAM. We believe (see below) that this is related to this peptide being near the “transition” between forming 3_{10} -helices and other, more intramolecularly H-bonded structures. For **5-**, however, we observe a

behavior very similar to that of peptides from 2+ to 5+, albeit with a quite lower intensity.

Whereas the spectral region pertaining to the amide I and II bands (Figure 60) does not show significant differences for 3- and 5- with respect to the plus series (beside the intensity of the signals), *I-* displays a band that is quite different from that of the other peptides.

It appears, therefore, that peptides *I+*, *3-* and, particularly, *I-* undergo a heavy conformational change when organized in SAMs on a gold surface. This was already emphasized in previous work from this laboratory, showing that the packing degree of *I-* is particularly large.⁸⁹ The value, $6.40 \pm 0.70 \cdot 10^{-10}$ (Table 4), can indeed be compared with the surface coverage typical of alkanethiols' SAMs on Au (111) lattice, i.e., $7.76 \cdot 10^{-10} \text{ mol cm}^{-2}$.¹⁰²

Generally, for the other peptides the packing is quite smaller because the peptides have a more complex and bulky structure than a simple alkanethiol chain. The coverage calculated for *I-*, however, is as much as 82% the alkanethiol value, witnessing a very similar packing and suggesting that for this particular peptide the helical structure is probably lost in favor of a more elongated structure (note: ideal alkanethiols' SAMs are formed by molecules adopting an all-trans conformation).

The frequency of the main bands of the minus series, for both the Amide A and the amide carbonyl regions, are gathered in Table 6.

Table 6: Values of wavenumbers obtained for each peptide for the minus series.

<i>H-Bonds</i>	<i>Region</i>	<i>Wavenumber (cm-1)¹</i>
<i>1</i>	Amide I	1685.8 (1669.8; 1699.19)
	Amide II	1556.5
	Amide A	3421.3
<i>3</i>	Amide I	1673.0
	Amide II	1531.1
	Amide A	3303.6
<i>5</i>	Amide I	1671.7
	Amide II	1535.2
	Amide A	3314.8

¹ The frequency values obtained from deconvolution are in parenthesis.

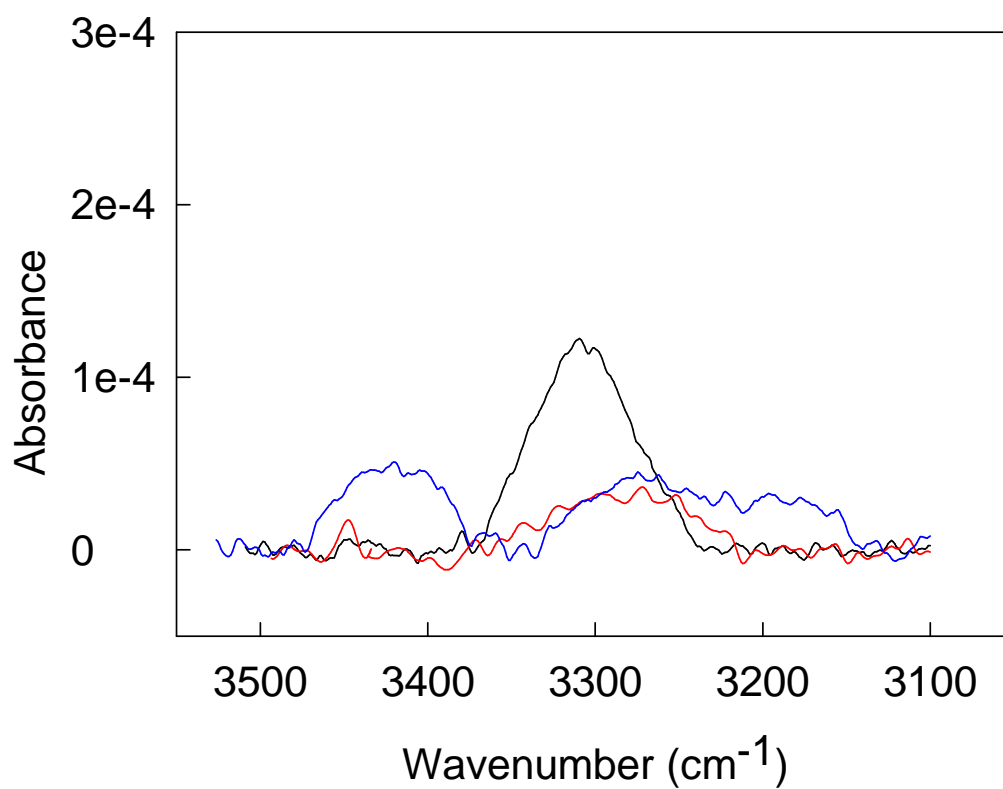


Figure 59. Amide A band of the peptide SAM of the minus series.

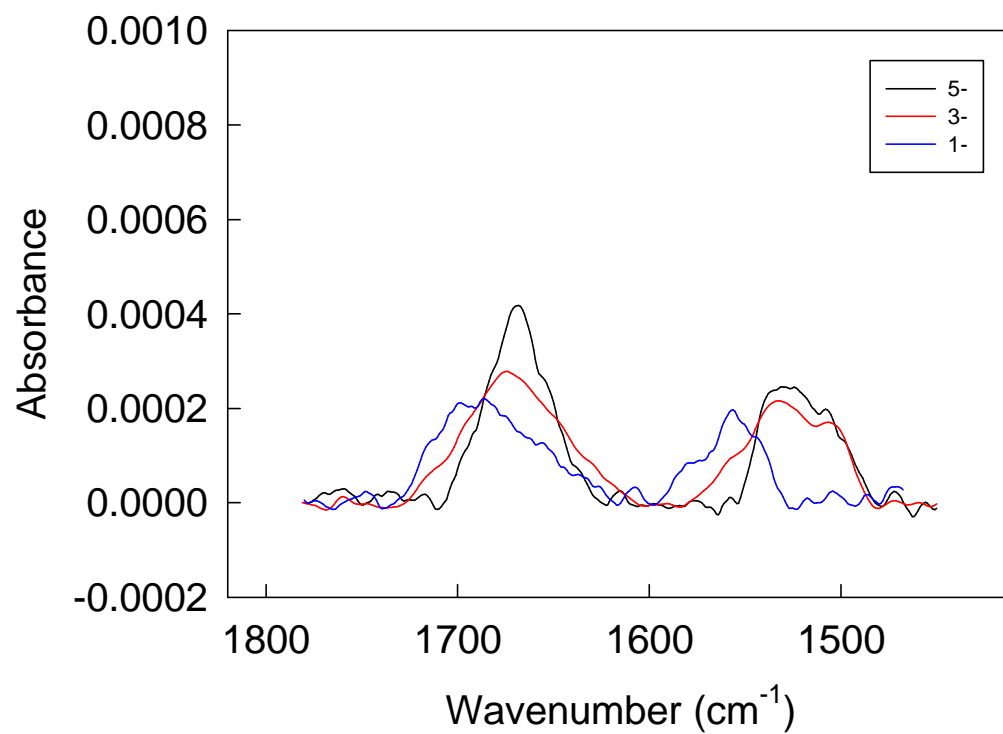


Figure 60. Amide I and II band of the peptide SAM of the minus series.

Based on the IRRAS observations, we can thus conclude that while in the SAM the *plus* series affords a more stable secondary structure than the *minus* series. The shortest peptides give less stable 3_{10} -helices, probably preferring to form intermolecular H-bonds. Disruption of the 3_{10} -helical structure is more evident with the *minus* series.

3.2.4 Determination of the Orientation of the Absorbed Molecules

The orientation of the absorbed molecules within the SAM is determined by several factors such as the adsorbate–substrate binding strength, the geometry of the binding site, the intermolecular interactions between the adsorbed molecules, and the solvent–adsorbate interactions.¹⁰³

As a result, the orientation of the peptide helix axis with respect to the substrate's surface normal is better described as a distribution of values. An orientation distribution function is thus necessary to interpret the IRRAS spectrum and calculate the average tilt angle from band intensities. Thus, Samulsky and coworkers¹⁰⁴ employed a Gaussian orientation distribution function to infer the peptide helix axis orientation in the SAM on gold. The helix axis orientation was obtained by optimizing the agreement between theoretical values for the amide I to amide II absorbance ratio, D (see equation 7), and the observed D value from the IRRAS experiments.

Figure 61 shows the coordinate system that describes the interaction between the polarized, incident IR electric field and the molecular transition moment in the grazing angle IRRAS experiment. Due to the surface selection rule¹⁰⁵, the only active electric-field component of the incident light (\mathbf{n}) is parallel to the Z-axis of the laboratory system (\mathbf{X} , \mathbf{Y} , \mathbf{Z}), the gold surface being in the \mathbf{X} – \mathbf{Y} plane. The transition moment \mathbf{m} (amide I or amide II band) is located in a molecule (helix)-fixed frame (x , y , z) by its respective polar and azimuthal angles (α , β). The x , y , z frame is oriented with the z -axis along the helix, and that axis is located in the laboratory system by θ , and Φ . γ is the azimuthal angle about the

helix axis. Using the relations among the Euler angles¹⁰⁶, the projection of \mathbf{m} on \mathbf{n} is given by:

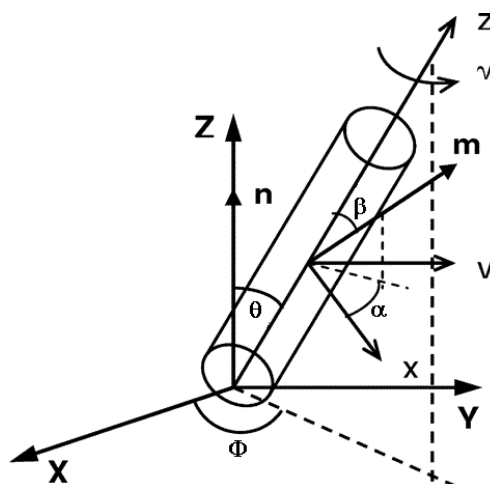


Figure 61. Coordinates of the laboratory (X, Y, Z) and molecular (x, y, z) systems for a tilted peptide on gold surface.

The IRRAS absorption intensity, A , is proportional to $|\mathbf{m} \cdot \mathbf{n}|^2$. Assuming uniform azimuthal distribution about the helix axis — γ is uniformly distributed over the interval $[0, 2\pi]$ — Samulski found that

— — — —

The α -dependence is simultaneously averaged by this assumption for γ . As the angles between the transition moment and the helix axis were determined to be 39° for β_1 (amide I band) and 75° for β_2 (amide II band),¹⁰⁷ A can be written as $A(\theta)$, where θ describes the tilt angle between the helix axis and the surface normal.

The observed IRRAS absorption intensity (A_{obs}) depends on the orientation distribution of the helices in the film. Thus, A_{obs} is the weighted superposition of contributions, $A(\theta) W(\theta) d\theta$, where $W(\theta)$ is the normalized helix axis orientation distribution function. Hence, we have

$$(5) \quad A_{obs} = \int_0^{\frac{\pi}{2}} A(\theta)W(\theta)d\theta \propto \int_0^{\frac{\pi}{2}} \langle |\mathbf{m} \cdot \mathbf{n}|^2 \rangle_{\gamma} W(\theta)d(\theta)$$

Similarly, the average of any function X of the tilt angle of the helix axis relative to the surface normal is

$$(6) \quad \langle X \rangle = \int_0^{\frac{\pi}{2}} X(\theta)W(\theta)d(\theta)$$

The amide I to amide II absorbance ratio is

$$(7) \quad D = K \frac{A_{obs}^I}{A_{obs}^{II}} = K \frac{\int_0^{\frac{\pi}{2}} \langle |\mathbf{m} \cdot \mathbf{n}|^2 \rangle_{\gamma}^I W(\theta)d(\theta)}{\int_0^{\frac{\pi}{2}} \langle |\mathbf{m} \cdot \mathbf{n}|^2 \rangle_{\gamma}^{II} W(\theta)d(\theta)}$$

where K is the scaling factor that relates the intrinsic ‘‘oscillator strength’’ of the amide I and amide II vibrational modes. K was determined to be 1.35 ± 2 from the transmission FTIR spectrum of a peptide KBr pellet.¹⁰⁴

The Gaussian orientation distribution function that was used to model the helix axis orientation distribution is

$$(8) \quad W(\theta) = N^{-1} \exp \left[-\frac{1}{2\sigma^2} (\theta - \theta_0)^2 \right] \sin(\theta)$$

where N is the normalization constant:

$$(9) \quad N = \int_0^{\frac{\pi}{2}} \exp \left[-\frac{1}{2\sigma^2} (\theta - \theta_0)^2 \right] \sin(\theta)d(\theta)$$

Assuming the monolayer to be an ideal isotropic film with a uniplanar distribution of helix axis confined to the gold substrate, θ results constant. Therefore, the helix-axis orientational distribution is a delta function: $W(\theta) = \delta(\theta - 90^\circ)$. This distribution is certainly reasonable for our monolayer.

The observed ratio of the amide I and amide II integrated intensities, $D_{\text{obs}} = A_{\text{obs}}^{\text{I}}/A_{\text{obs}}^{\text{II}}$, is thus calculated from the equation, for which we know $W(\theta) = \delta(\theta - 90^\circ)$. Therefore, the orientation of the peptides adsorbed on the gold surface was determined according to the following equation, assuming an isotropic monolayer:

$$(10) \quad D = K \frac{A_{\text{obs}}^{\text{I}}}{A_{\text{obs}}^{\text{II}}} = K \frac{\langle |m^{\text{I}} \cdot n|^2 \rangle}{\langle |m^{\text{II}} \cdot n|^2 \rangle} = 1.35 \frac{(3 \cos^2 \theta - 1)(3 \cos^2 \beta_1 - 1) + 2}{(3 \cos^2 \theta - 1)(3 \cos^2 \beta_2 - 1) + 2}$$

$$(11) \quad \delta D = \left| \frac{\partial D}{\partial A^{\text{I}}} \right| \cdot \delta A^{\text{I}} + \left| \frac{\partial D}{\partial A^{\text{II}}} \right| \cdot \delta A^{\text{II}} = \frac{1}{A^{\text{II}}} \cdot \delta A^{\text{I}} + \frac{A^{\text{I}}}{(A^{\text{II}})^2} \cdot \delta A^{\text{II}}$$

$A_{\text{obs}}^{\text{I}}$ and $A_{\text{obs}}^{\text{II}}$ are the observed absorbances of amide I and amide II bands, θ is the tilt angle of the helical axis, and β_1 and β_2 represent the angles between the transition moment and the helix axis, those value were taken to be 39° and 75° , respectively.¹⁰⁷

In order to take the maximum value of observed absorbance, we selected the two zones of the spectrum where the amide I and amide II bands are present. Then, we employed three different nonlinear regression analyses (the Gaussian, the Pseudo-Voigt, and the Lorentzian fitting methods) to optimize the agreement between the theoretical values for the amide I to amide II absorbance ratio, and the observed D value from the IRRAS experiments. After several tests, we opted for using only the Gaussian regression, which gave the best peaks. In some cases, to find the best values of maximum absorbance, we also used a deconvolution, and to calculate the corresponding error, we used the conventional linear propagation:

$$(11) \quad y = y_0 + a \cdot e^{\left[-0.5 \left(\frac{x-x_0}{b} \right)^2 \right]}$$

$$(12) \quad \delta y = \delta y_0 + e^{\left[-0.5\left(\frac{x-x_0}{b}\right)^2\right]} \cdot \delta a + \left\{ \frac{a(x-x_0)^2 e^{\left[-0.5\left(\frac{x-x_0}{b}\right)^2\right]}}{b^3} \right\} \cdot \delta b$$

$$+ \left\{ \frac{a(x-x_0) e^{\left[-0.5\left(\frac{x-x_0}{b}\right)^2\right]}}{b^3} \right\} \cdot \delta x_0$$

Then, to calculate the tilt angle of each peptide and the corresponding errors, we used the following equations, obtained from equation 10.

$$(13) \quad \theta = \arccos \left[\sqrt{\left(\frac{2K-2D}{D \cdot (3 \cos^2 \beta_2 - 1) - (3 \cos^2 \beta_1 - 1)K} + 1 \right) \cdot \frac{1}{3}} \right]$$

$$(14) \quad \delta \theta = \left\{ - \frac{1}{\sqrt{1 - \left(\frac{2K-2D}{D \cdot (3 \cos^2 \beta_2 - 1) - (3 \cos^2 \beta_1 - 1)K} + 1 \right) \cdot \frac{1}{3}}} \right. \\ \cdot \frac{1}{2} \frac{1}{\sqrt{\left(\frac{2K-2D}{D \cdot (3 \cos^2 \beta_2 - 1) - (3 \cos^2 \beta_1 - 1)K} + 1 \right) \cdot \frac{1}{3}}} \\ \cdot \frac{1}{3} \left(\frac{2}{D \cdot (3 \cos^2 \beta_2 - 1) - (3 \cos^2 \beta_1 - 1)K} \right. \\ \left. - \frac{(3 \cos^2 \beta_2 - 1)(2K-2D)}{(D \cdot (3 \cos^2 \beta_2 - 1) - (3 \cos^2 \beta_1 - 1)K)^2} \right) \left. \right\} \cdot \delta D$$

$$+ \left\{ - \frac{1}{\sqrt{1 - \left(\frac{2K-2D}{D \cdot (3 \cos^2 \beta_2 - 1) - (3 \cos^2 \beta_1 - 1)K} + 1 \right) \cdot \frac{1}{3}}} \right. \\ \cdot \frac{1}{2} \frac{1}{\sqrt{\left(\frac{2K-2D}{D \cdot (3 \cos^2 \beta_2 - 1) - (3 \cos^2 \beta_1 - 1)K} + 1 \right) \cdot \frac{1}{3}}} \\ \cdot \frac{1}{3} \left(\frac{2}{D \cdot (3 \cos^2 \beta_2 - 1) - (3 \cos^2 \beta_1 - 1)K} \right. \\ \left. + \frac{K(2K-2D)}{(D \cdot (3 \cos^2 \beta_2 - 1) - (3 \cos^2 \beta_1 - 1)K)^2} \right) \left. \right\} \cdot \delta K$$

From these calculations, we obtained the values shown in Table 7.

Table 7: Amide I to Amide II Absorbance Ratio and relative Tilt angle.

<i>H-Bonds</i>	$D = A^I/A^{II}$	<i>Tilt Angle θ (degrees)</i>
<i>1+</i>	1.16	54.7
<i>2+</i>	1.68	49.5
<i>3+</i>	2.06	44.6
<i>4+</i>	2.80	37.9
<i>5+</i>	5.90	22.4
<i>1-</i>	1.20	57.8
<i>3-</i>	1.25	56.7
<i>5-</i>	1.38	54.2

Of course, all these data rely on a series of assumptions. First, we assume of having a monatomically smooth Au(111) surface and that there is no surface roughness (i.e., an angular spread resulting from a less-than-flat surface that should be convolved with the angular distribution of the helix axes). This is a significant assumption as the IR beam size is macroscopic in areal dimensions and it is doubtful that a uniform surface (other than a single crystal) describes such a large area. On the other hand, in the Experimental section we stressed that the freshly annealed surface is mostly a (111) surface and the roughness factor is close to 1, being 1.16 ± 0.08 . Second, we assume that the SAM is isotropic and defect-free, and this is something that is obviously not true as thoroughly commented upon in the introducing chapter. Finally, how well is the helix axis defined? At the polypeptide-air interface, for example, we expect some dynamic behaviour that introduces some uncertainty about the definition of the helix axis itself. That the helices are stable is true for the longest peptides of the plus and minus series, but it is not completely valid for shorter peptides, particularly those of the *minus* series. For these peptides, θ_1 and θ_2 may thus be slightly different. Because of these assumptions, we consider that an error of at least $\pm 5^\circ$ is more reasonable than that of $\pm 1^\circ$ deriving from our calculations. Figure 63 shows that the long peptides of the *plus* series are less tilted than shorter ones.

We should stress that the figure also includes *I+* and *I-*, although the error on the determination of their amide II intensity indicates that the calculated tilt

angles suffer an even larger error than that indicated in the figure. Noteworthy, Figure 63 shows that when the number of H-bonds increases the tilt angle decreases smoothly. Therefore, it appears that long peptides are suitable to better self-assemble on the surface. In other words, the more rigid is the secondary structure of the peptide, the more the SAM is ordered and the molecules are perpendicular to the surface. It is also interesting to note that in the *minus* series the tilt angle depends very little on the peptide length. These angles are similar to those of *1+* and *2+*. This means that the peptides of the *minus* series are, on average, significantly more tilted than those of the *plus* series.

The tilt angles that we calculated are generally larger than those of alkanethiols, $\sim 30^\circ$. On the other hand, helical peptides show tilt angles in the range from 20° to 55° ,^{108,109,110,111} in line with our results. The majority of literature calculations are based on IRRAS data.

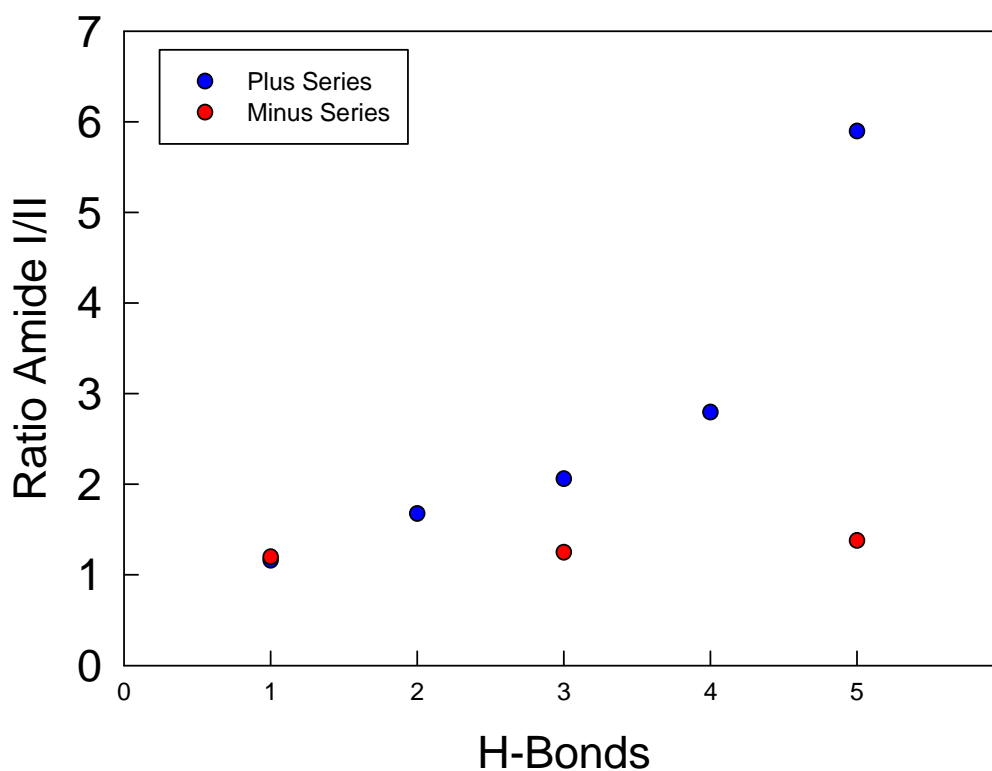


Figure 62. Dependence of the ratio between the absorbance of amide I and that of amide II on the number of H-bonds for the plus and the minus series.

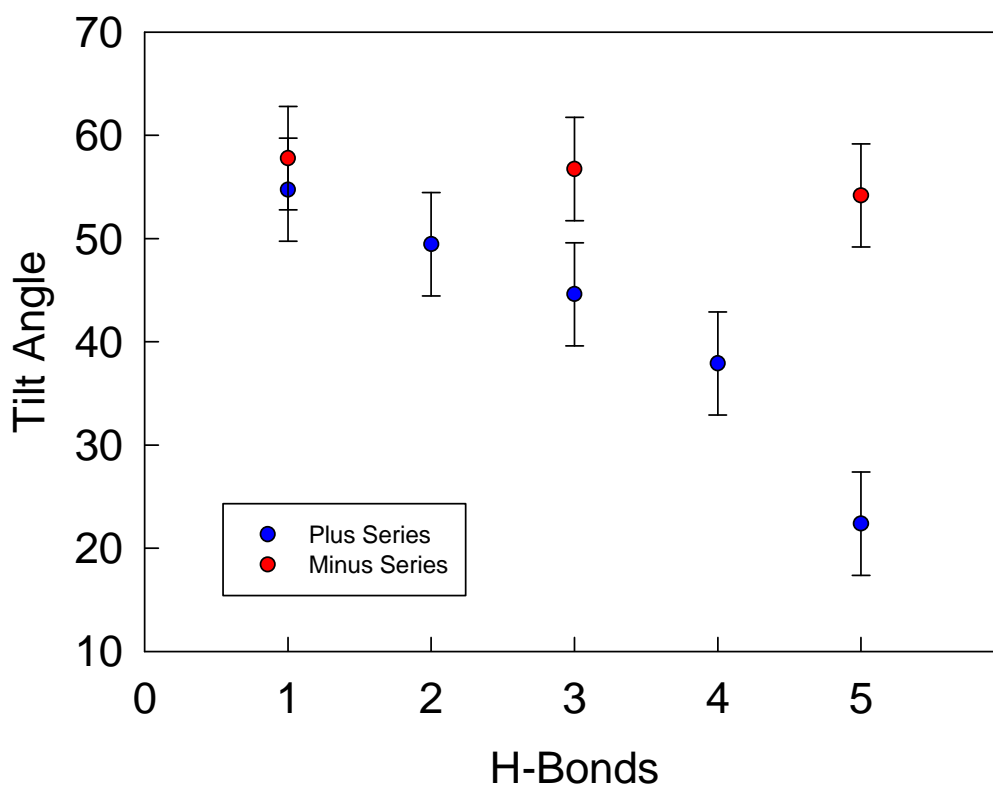


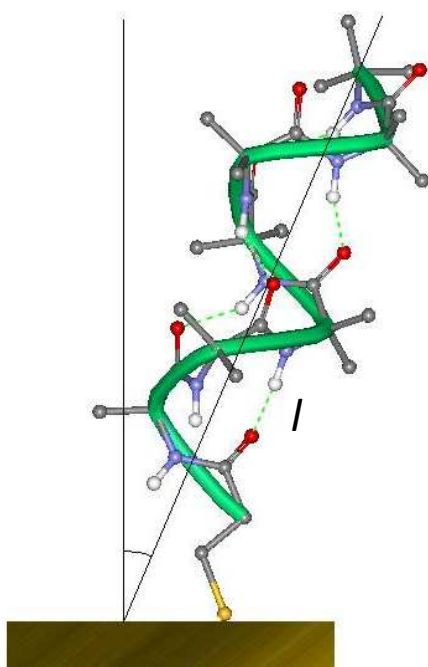
Figure 63. Dependence of the tilt angle of the helix axis on number of H-bonds for the plus and minus series.

3.2.5. Determination of the Thickness of the Monolayer

The thickness of the monolayers (h) can be calculated from the tilt angle (θ) and the length of the peptide (l). The lengths of the investigated peptides have been calculated (for perfect 3_{10} -helices) from molecular models. The length was calculated from the hydrogen of the SH group (mimicking Au) to the hydrogen of the most distant CH_3 of the *tert*-butyl group. The calculated lengths are: *1+*, 11.6 Å; *2+*, 13.6 Å; *3+*, 15.2 Å; *4+*, 16.7 Å; *5+*, 18.6 Å; *1-*, 11.3 Å; *3-*, 15.2 Å; *5-*, 18.9 Å. As shown in Figure 64, the thickness of the monolayer can be calculated by applying a simple trigonometric formula. This calculation logically brings with it all the approximations made with the calculation of the tilt angle. Although the calculated values are affected by a non-negligible error, a relative comparison between peptides of the *plus* and *minus* series can still be carried out.

Further investigations on the monolayer thickness have been planned for future work using other methods of analysis, such as ellipsometry and ARXPS (angle resolved X-ray photoelectron spectroscopy: this is a technique in which the photoelectron take-off angle allows reducing the depth from which the XPS information is obtained; its most important application is, in fact, the estimation of the thickness of thin films and thus SAMs), and the values will be compared. This comparison will provide a useful way to validate the method based on the amide I and amide II ratio.

As Figure 62 shows, the thickness of the monolayers for the *plus* series increases with the number of H-bonds but, due to the decrease of the tilt, not according to a linear function. For the *minus* series it appears that the thickness increases in a similar way, but with an average smaller slope. To conclude, the *minus* series forms thinner monolayers than the *plus* series. If we now consider the surface coverages of Table 4, a smaller thickness of these monolayers is probably determined by a less effective packing on the surface, which may allow the peptides to tilt more significantly.



$$h = l \cdot \cos \alpha$$

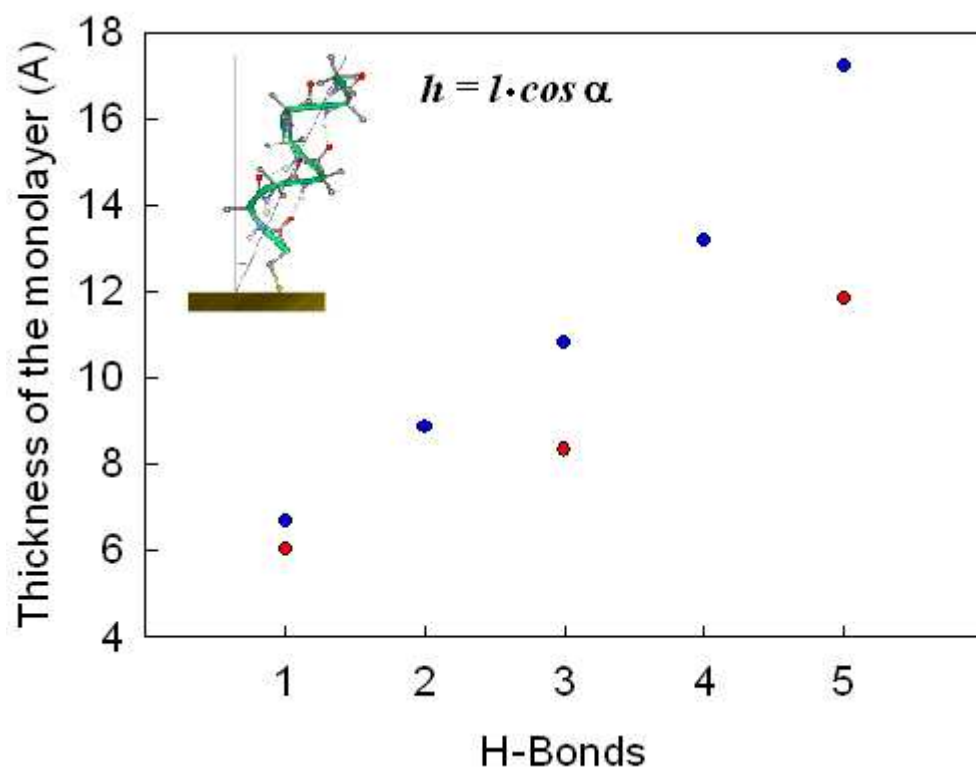


Figure 64. The graph shows the trend of the monolayer thickness as a function of the number of hydrogen bonds for the plus (blue circles) and the minus series (red circles). The inset shows a graphical representation showing how the calculation was carried out.

4. Conclusions

Nowadays the Enzyme-Linked Immunosorbent Assay (ELISA) based on optical absorbance is the standard bioanalysis method with claimed detection limits as low as 3 pg/mL for Prostate Specific Antigen (PSA).¹¹² ELISA, however, suffers limitations in analysis time, sample size, and multiplexing. Preliminary studies in Jim Rusling's laboratories suggest good potential for nanoparticles to make bioelectronic sensor array platforms to measure collections of cancer biomarkers simultaneously, at high sensitivity (for example the detection limit for PSA was obtained as low as 0.5 pg/mL)⁹, and without compromising analysis time or sample size. To assess the accuracy of the AuNP sensor in real biomedical situations, a collection of human serum samples with varying PSA content were used. These samples were also assayed by standard ELISA method. As Figure 65 shows, immunosensor results indeed display a very good correlation with ELISA from sub-ng/mL concentration range to above 10 ng/mL, for this representative serum samples set.⁹

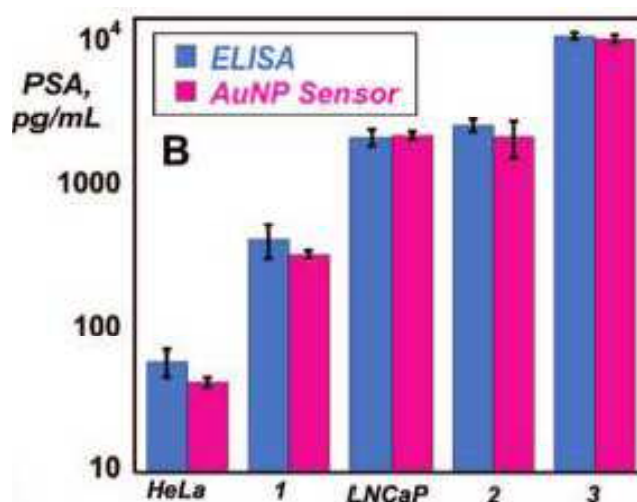


Figure 65. Validation of AuNP sensor results for human serum samples by comparing against results from ELISA determination for same samples.

It was thus demonstrated that the AuNP platform is competitive with other state-of-the-art approaches in terms of both sensitivity and detection limit in real samples, and may prove to have marked economic advantages in future array fabrication. On these grounds, we employed this kind of electrochemical immunosensor to a new biomarker that may be involved in carcinogenesis of cervix and progression of cervical carcinoma. We should stress, in fact, that nowadays researchers still do not know the detection limit of this particular biomarker; similarly, the difference of concentration between healthy individuals and patients with cancer is still unknown.

Since we did not know the range of the expression of the Nanog biomarker, we started by adopting the same approach that was previously adopted for the PSA biomarker.⁹ Step by step, we optimized the experimental conditions by changing the concentrations of the several solutions used for preparing the immunosensor. Inhibition of non-specific binding of labeled detection antibodies was the most crucial step, because if the concentration of BSA was too high the signal was annihilated, but if the concentration was too low the signal was not reproducible.

Since a significant number of biomarkers have normal levels in the low pg/mL range, we aimed at reaching sensitivity in this concentration range in order to make a sensor capable of measuring both normal (= low) concentrations representative of cancer-free patients and elevated levels indicative of cancer. Therefore, we implemented our immunosensor using StrMPs-bioAb₂-bioHRP that conferred the best sensitivity and the best detection limit, due to the high number of labels on each magnetic bead. In fact, as demonstrated in the Results and Discussion, we obtained a calibration plot that shows high sensitivity, good reproducibility and the low detection limit of 0.1 pg/mL; this will allow the study of serum samples from both healthy individuals and patients with cervical carcinoma. Integrating the electrochemical biosensor into a purposely designed electrochemical microfluidics device proved to be a very promising strategy to improve the sensor further. We believe that, after standardization of the method, this immunosensor should be readily adaptable to measure Nanog biomarker expression in real patients, for point-of-care early detection and monitoring of cancer disease.

We also carried out an investigation of the properties of two series of peptide SAMs in order to check their potential as possible templates for building the above biosensor/s. In a well-performing electrochemical biosensor, the control of the ET through the monolayer is of paramount importance. The ET behavior is dictated by the properties of the SAM in terms of electron tunneling and quality of the SAM itself. Aib-homopeptides were chosen for their peculiar properties to form stable and robust 3_{10} -helices even for short oligomers. For these systems, the ET rate is favored by the stiffness of the secondary structure, which in turn is associated with the presence of an extended network of intramolecular H-bonds. Two series of thiolated Aib-homopeptides were studied: a *plus* series with the positive pole of the dipole moment on the sulfur side and a *minus* series whose dipole moment is reversed. In each series the number of residues was varied. For the *plus* series, the number of residues varies from 1 to 6, allowing to study the effect of having from 0 to 5 intramolecular H-bonds (according to the 3_{10} -helix). For the *minus* series we focused on peptides with 1, 3, and 5 H-bonds.

The structure and the stability of the secondary structure of the adsorbed peptides while in the SAMs were studied by IRRAS spectroscopy. We observed differences as a function of both the peptide length and orientation. The data showed that stable 3_{10} -helices form for most peptides, while for the shortest peptides competition between intra- and intermolecular H-bonds makes things more complex. In general, we found that when peptides are organized in the SAM, a wide network of lateral interaction is established, which contributes to increase the stability of the SAM itself and strengthens the secondary structure of the SAM constituents. This is particularly true for the *plus* series that proved to be slightly more stable, as helices, than the corresponding series of free peptides in solution.

Complementary information on the organization of the SAM was gathered by calculation of the tilt angle. We found that the *plus* series gives SAMs with more vertically oriented molecules and thus thicker SAMs than for the *minus* series. It thus appears that the reversed dipole moment of the *minus* series is somehow slightly destabilizing the structure of the SAM relative to the *plus* series. Because of this destabilization, the peptides of the *minus* series prefer to

adopt a more pronounced tilt angle with respect to the surface normal. With *I-* the 3_{10} -helical structure is totally modified (or even lost) in favor of later interactions.

From our study, we conclude that long peptides of the *plus* series are liable to provide the most stable and ordered monolayers, whereas shorter peptides form SAMs that are less stable and more prone to defects. This evidence, together with the excellent ET properties of the long peptides of the *plus* series,⁸⁹ thus suggests that sufficiently long peptides of the *plus* series may provide a particularly convenient support for the construction of efficient electrochemical biosensors.

This Thesis was made possible by the collaboration (and friendship) between my supervisor, Prof. Flavio Maran, and co-supervisor, Prof. Jim Rusling. The research proceeded smoothly and although some aspects are still waiting to be addressed, the general outcome of the two related topics was as all of us hoped. New challenges are, however, around the corner. To improve the efficiency of the biosensor, we are about to optimize the immunosensor by changing some elements of the transducer, particularly by using Aib-peptide SAMs which should lead to very fast electrode kinetics. We are also investigating the possibility of increasing the active surface of the electrode substrate, for example by using nanostructured gold electrodes¹¹³ as an alternative to a bed of AuNPs. Some attempts in this direction have been carried out, but this an aspect that for time limitations of this Thesis could not be covered.

5. References

- [1] McNaught, A. D.; Wilkinson, A.; *Compendium of Chemical Terminology*, 2nd ed.; Blackwell Scientific Publications, Oxford, **1997**.
- [2] Wang, J.; *Glucose Biosensors: 40 years of advances challenges Electroanalysis*, **2001**, *13*, 983-988.
- [3] Turner, A. P. F.; Karube, I.; Wilson, G. S.; *Biosensors: Fundamentals and Applications*, Oxford University Press, **1987**.
- [4] Bashir, D. R.; Ferrari, M.; Wereley, S.; *Biomolecular sensing, processing and analysis*, Springer, **1987**.
- [5] Chaki, N. K.; Vijayamohanan, K.; *Biosensors and Bioelectronics*, **2002**, *17*, 1-12.
- [6] Koncki, R.; *Anal. Chim. Acta*, **2007**, *599*(1), 7-15.
- [7] Ligler, F. S.; *Anal. Chem.*, **2009**, *81*(2), 519-26.
- [8] Ramanathan, K.; Danielsson, B.; *Biosensor Bioelectron.*, **2001**, *16*(6), 417-23.
- [9] Mani, W.; Chikkaveeraiah, B. V.; Patel, V.; Gutkind, J. S.; Rusling, J. F.; *ACSNano*, **2009**, *3*(3), 585-594.
- [10] Pui-ye, C. C.; Cheung, C. Y.; Renneberg, R.; Seydack, M.; *Biochem. Engin./Biotechnol.*, **2008**, *109*, 123-154.
- [11] Pober, J. S.; Lichtman, A. H.; Abbas, A. K.; *Immunologia cellulare e molecolare*, **2002**, XI-596 p., 4th Ed., Piccin-Nuova Libreria.
- [12] Ambrosi, A.; Castañeda, M. T.; Killard, A. J.; Smyth, M. R.; Alegret, S.; Merkoçi, A.; *Anal. Chem.*, **2007**, *79*(14), 5232-40.
- [13] De la Encosura-Muñiz, A. ; Maltez-da Costa, M.; Merkoçi, A.; *Biosensors and Bioelectronics*, **2009**, *24*, 2475-2482.
- [14] Chikkaveeraiah, B. V.; Liu, H; Mani V.; Papadimitrakopoulos, F.; Rusling, J. F. *Electrochemistry Communications*, **2009**, *11*, 819-822.
- [15] Ye, F.; Zhou, C.; Cheng, Q.; Shen, J.; Chen, H.; *BioMed Central Cancer*, **2008**, *8*:108.

- [16] (a) Willner, I.; Katz, E. *Angew. Chem., Int. Ed.* **2000**, *39*, 1181-1218. (b) Gooding, J. J.; Mearns, F.; Yang, W.; Liu, J. *Electroanalysis* **2003**, *15*, 81-96. (c) Rosi, N. L.; Mirkin, C. A. *Chem. Rev.* **2005**, *105*, 1547-1562. (d) Rusling, J. F.; Wang, B.; Yun, S.-E. Electrochemistry of Redox Enzymes, In *Bioelectrochemistry*, Bartlett, P. N. Ed., John Wiley, N. Y. **2008**, Chapter 2, pp. 39-86. (e) Rusling, J. F.; Hvastkovs, E. G.; Hull, D. O.; Schenkman, J. B. *Chem Commun.* **2008**, 141-154. (f) Polsky, R.; Harper, J. C.; Wheeler, D. R.; Brozik, S. M. *Electroanalysis* **2008**, *20*, 671-679. (g) Tkac, J.; Davis, J. J. Label-free Field Effect Protein Sensing, In *Engineering the Bioelectronic Interface*, Davis, J. J. Ed., Royal Soc. Chem. UK, **2009**, pp. 193-224. (h) Polsky, R.; Harper, J. C.; Brozik, S. M. Nanoparticle and Biomolecular-Nanoparticle Hybrid Supramolecular Complexes for Electrochemical Signaling, In *The Supramolecular Chemistry of Organic-Inorganic Hybrid Materials*, Rurack, K., Martinez-Manez, R. Eds, John Wiley, N. Y. **2010**, Chapter 8, pp 273-296.
- [17] (a) Ulman, A. *Chem. Rev.* **1996**, *96*, 1533-1554. (b) Adams, D. M.; Brus, L.; Chidsey, C. E. D.; Creager, S.; Creutz, C.; Kagan, C. R.; Kamat, P. V.; Lieberman, M.; Lindsay, S.; Marcus, R. A.; Metzger, R. M.; Michel-Beyerle, M. E.; Miller, J. R.; Newton, M. D.; Rolison, D. R.; Sankey, O.; Schanze, K. S.; Yardley, J.; Zhu, X. *J. Phys. Chem. B* **2003**, *107*, 6668-6697. (c) Love, J. C.; Estroff, L. A.; Kriebel, J. K.; Nuzzo, R. G.; Whitesides, G. M. *Chem. Rev.* **2005**, *105*, 1103-1169. (d) Chen, D.; Li, J. *Surface Sci. Reports* **2006**, *61*, 445-463. (e) Newton, M. D.; Smalley, J. F. *Phys. Chem. Chem. Phys.* **2007**, *9*, 555-572.
- [18] (a) Marcus, R. A.; Sutin, N. *Biochim. Biophys. Acta* **1985**, *811*, 265-322. (b) Barbara, P. F.; Meyer, T. J.; Ratner, M. A. *J. Phys. Chem.* **1996**, *100*, 13148-13168.
- [19] (a) Newton, M. D. *Chem. Rev.* **1991**, *91*, 767-792. (b) Nitzan, A. *Ann. Rev. Phys. Chem.* **2001**, *52*, 681-750. (c) Paddon-Row, M. N. *Aus. J. Chem.* **2003**, *56*, 729-748.
- [20] (a) Skourtis, S. S.; Beratan, D. N. *Adv. Chem. Phys.* **1999**, *106*, 377-452. (b) Regan, J. J.; Onuchic, J. N. *Adv. Chem. Phys.* **1999**, *107*, 497-553. (c) Winkler, J. R. *Curr. Opin. Chem. Biol.* **2000**, *4*, 192-198. (d) Gray, H. B.;

Winkler, J. R. In *Electron Transfer in Chemistry*; Balzani, V., Ed.; Wiley-VCH: Weinheim, 2001; Vol. 1, pp 3-23.

- [21] (a) Page, C. C.; Moser, C. C.; Chen, X.; Dutton, P. L. *Nature* **1999**, *402*, 47-52. (b) Kelley, S. O.; Barton, J. K. *Science* **1999**, *283*, 375-381. (c) Jortner, J.; Bixon, M.; Langenbacher, T.; Michel-Beyerle, M. E. *Proc. Nat. Acad. Sci.* **1998**, *95*, 12759-12765. (d) Schuster, G. B. *Acc. Chem. Res.* **2000**, *33*, 253-260. (e) Giese, B. *Ann. Rev. Biochem.* **2002**, *71*, 51-70. (f) Berlin, Y. A.; Burin, A. L.; Ratner, M. A. *Chem. Phys.* **2002**, *275*, 61-74. (g) Lewis, D.; Liu, J.; Weigel, W.; Rettig, W.; Kurnikov, I. V.; Beratan, D. N. *Proc. Nat. Acad. Sci.* **2002**, *99*, 12536-12541.
- [22] a) Anderson, P. W. *Phys. Rev.* **1950**, *79*, 350-356. (b) McConnell, H. M. *J. Chem. Phys.* **1961**, *35*, 508-515.
- [23] (a) Grozema, F. C.; Berlin, Y. A.; Siebbeles, L. D. A. *J. Am. Chem. Soc.* **2000**, *122*, 10903-10909. (b) Bixon, M.; Jortner, J. *J. Am. Chem. Soc.* **2001**, *123*, 12556-12567. (c) Li, X.-Q.; Zhang, H.; Yan, Y. J. *J. Phys. Chem. A* **2001**, *105*, 9563-9567. (d) Renger, T.; Marcus, R. A. *J. Phys. Chem. A* **2003**, *107*, 8404-8419.
- [24] (a) Long, Y.-T.; Abu-Irhayem, E.; Kraatz, H.-B. *Chem. Eur. J.* **2005**, *11*, 5186-5194. (b) Schlag, E. W. , Sheu, S.-Y. ; Yang, D.-Y. ; Selzle, H. L.; Lin, S. H. *Angew. Chem., Int. Ed.* **2007**, *46*, 3196-3210.
- [25] (a) Yanagisawa, K.; Morita, T.; Kimura, S. *J. AM. Chem. Soc.* **2004**, *126*, 12780-12781. (c) Giese, B.; Graber, M.; Cordes, M. *Curr. Opin. Chem. Biol.* **2008**, *12*, 755-759.
- [26] Antonello, S.; Maran, F. *Chem. Soc. Rev.* **2005**, *34*, 418-428.
- [27] Rampi, M. A.; Whitesides, G. M. *Chem. Phys.* **2002**, *281*, 373-391.
- [28] Smalley, J. F.; Finklea, H. O.; Chidsey, C. E. D.; Linford, M. R.; Creager, S. E.; Ferraris, J. P.; Chalfant, K.; Zawodzinsk, T.; Feldberg, S. W.; Newton, M. D. *J. Am. Chem. Soc.* **2003**, *125*, 2004-2013.
- [29] (a) Morita, T.; Kimura, S. *J. Am. Chem. Soc.* **2003**, *125*, 8732-8733. (b) Watanabe, J.; Morita, T.; Kimura, S. *J. Phys. Chem. B* **2005**, *109*, 14416-14425. (c) Kai, M.; Takeda, K.; Morita, T.; Kimura, S. *J. Pept. Sci.* **2008**, *14*, 192-202. (d) Takeda, K.; Morita, T.; Kimura, S. *J. Phys. Chem. B*

- 2008**, *112*, 12840–12850. (e) Arikuma, Y.; Takeda, K.; Morita, T.; Ohmae, M.; Kimura, S. *J. Phys. Chem. B* **2009**, *113*, 6256–6266.
- [30] (a) Galka, M. M.; Kraatz, H.-B. *ChemPhysChem* **2002**, *3*, 356-359. (b) Bediako-Amoa, I.; Sutherland, T. C.; Li, C.-Z.; Silerova, R.; Kraatz, H.-B. *J. Phys. Chem. B* **2004**, *108*, 704-714. (c) Kraatz, H.-B.; Bediako-Amoa, I.; Gyepi-Garbrah, H.; Sutherland, T. C. *J. Phys. Chem. B* **2004**, *108*, 20164-20172. (d) Dey, S. K.; Long, Y. T.; Chowdhury, S.; Sutherland, T. C.; Mandal, H. S.; Kraatz, H. B. *Langmuir* **2007**, *23*, 6475–6477. (e) Orłowski, G. A.; Chowdhury, S.; Kraatz, H. B. *Langmuir* **2007**, *23*, 12765–12770.
- [31] (a) Bilewicz, R.; Sek, S.; Zawiska, I. *Russ. J. Electrochem.* **2002**, *38*, 29-38. (b) Sek, S.; Moszynski, R.; Sepiol, A.; Misicka, A.; Bilewicz, R. *J. Electroanal. Chem.* **2003**, *550-551*, 359-364. (c) Sek, S.; Sepiol, A.; Tolak, A.; Misicka, A.; Bilewicz, R. *J. Phys. Chem. B* **2004**, *108*, 8102-8105. (d) Sek, S.; Tolak, A.; Misicka, A.; Palys, B.; Bilewicz, R. *J. Phys. Chem. B* **2005**, *109*, 18433–18438. (e) Sek, S.; Swiatek, K.; Misicka, A. *J. Phys. Chem. B* **2005**, *109*, 23121–23124. (f) Sek, S.; Misicka, A.; Swiatek, K.; Maicka, E. *J. Phys. Chem. B* **2006**, *110*, 19671–19677. forse solo SPM
- [32] For recent ET studies on redox proteins and relevant references, see: (a) Davis, K. L.; Drews, B. J.; Yue, H.; Waldeck, D. H.; Knorr, K.; Clark, R. A. *J. Phys. Chem. C* **2008**, *112*, 6571–6576. (b) Millo, D.; Ranieri, A.; Gross, P.; Ly, H. K.; Borsari, M.; Hildebrandt, P.; Wuite, G. J. L.; Gooijer, C.; van der Zwan, G. *J. Phys. Chem. C* **2009**, *113*, 2861-2866.
- [33] Brooksby, P. A.; Anderson, K. H.; Downard, A. J.; Abell, A. D. *Langmuir*, **2010**, *26*, 1334-1339.
- [34] Porter, M. D.; Bright, T. B.; Allara, D. L.; Chidsey, C. E. D. *J. Am. Chem. Soc.* **1987**, *109*, 3559-3568.
- [35] (a) Becka, A. M.; Miller, C. J. *J. Am. Chem. Soc.* **1992**, *96*, 2657-2668. (b) Becka, A. M.; Miller, C. J. *J. Phys. Chem.* **1992**, *96*, 2657-2668. (c) Becka, A. M.; Miller, C. J. *J. Phys. Chem.* **1993**, *97*, 6233-6239. (d) Terrettaz, S.; Becka, A. M.; Traub, M. J.; Fettingner, J. C.; Miller, C. J. *J. Phys. Chem.* **1995**, *99*, 11216-11224. (e) Cheng, J.; Sàghi-Szabò, G.; Tossel, J. A.; Miller, C. J. *J. Am. Chem. Soc.* **1996**, *118*, 680-684.

- [36] Kryszynski, P.; Brostowska-Smolka, M. *J. Electroanal. Chem.* **1997**, *424*, 61-67.
- [37] Doneux, T.; Steichen, M.; Bouchta, T.; Buess-Herman, C. *J. Electroanal. Chem.* **2007**, *599*, 241-248.
- [38] Protsailo, L. V.; Fawcett W. R. *Electrochim. Acta* **2000**, *45*, 3497–3505. (Studio tramite impedenza)
- [39] Smalley, J. F.; Newton, M. D.; Feldberg, S. W. *J. Electroanal. Chem.* **2006**, *589*, 1–6.
- [40] (a) Degefa, T. H.; Schön, P.; Bongard, D.; Walder, L. *J. Electroanal. Chem.* **2004**, *574*, 49-62. (b) Hwang, S.; Lee, B. S.; Chi, Y. S.; Kwak, J.; Choi, I. S.; Lee, S. *J. Electrochim. Acta* **2008**, *53*, 2630-2636.
- [41] Badia, A.; Lennox, B.; Reven, L. *Acc. Chem. Res.* **2000**, *33*, 475-481.
- [42] Bizzotto, D.; Yu, H.; Cheng, A.K.H.; Murphy, J. N. *J. Am. Chem. Soc.*, **2009**, *131*, 4042-4050.
- [43] (a) Zhao, X.; Wilbur, J. L.; Whitesides, G. M. *Langmuir* **1996**, *12*, 3257-3264. (b) Che, G.; Cabrera C. R. *J. Electroanal. Chem.* **1996**, *417*, 155-161. (c) Che, G.; Li, Z.; Zhang, H.; Cabrera C. R. *J. Electroanal. Chem.* **1998**, *453*, 9–17. (d) Protsailo, L. V.; Fawcett, W. R. *Langmuir* **2002**, *18*, 8933-8941. (Analisi dei difetti con Impedenza) (e) Benítez, G.; Vericat, C.; Tanco, S.; Lenicov, R. F.; Castez, M. F.; Vela, M. E.; Salvarezza R. C.; *Langmuir* **2004**, *20*, 5030-5037. (f) Kiani, A.; Alpuche-Aviles, M. A.; Eggers, P. K.; Jones, M.; Gooding, J. J.; Paddon-Row, M. N.; Bard, A. J. *Langmuir* **2008**, *24*, 2841-2849. (g) Preiner, M. J.; Melosh, N. A. *Langmuir* **2009**, *25*, 2585-2587.
- [44] (a) Liu, B.; Mirkin, M. V.; Bard, A. J.; Creager, S. E. *J. Am. Chem. Soc.* **2004**, *126*, 1485-1492.; (b) Finklea, O. H. *Langmuir* **1993**, *9*, 3660-3667; (c) Chailapaku, O.; Crooks, R. M. *Langmuir* **1995**, *11*, 1329-1340; (d) Orłowski, G. A.; Kraatz, H. *Electrochimica Acta* **2006**, *51*, 2934–2937.
- [45] Strattmann, M. *Adv. Mater.* **1990**, *2*, 191.
- [46] Ulman, A. *Thin Solid Films* **1996**, *273*, 48-53.
- [47] Nuzzo, R. C.; Dubois, L. H.; Allara, D. L. *J. Am. Chem. Soc.* **1990**, *112*, 558-569.
- [48] DePalma, V.; Tillman, N. *Langmuir* **1989**, *5*, 868-872.

- [49] Ferguson, G. S.; Chaudhury, M. K.; Sigal, G. B.; Whitesides, G. M. *Science* **1991**, *253*, 776-778.
- [50] Chen, J.; Reed, M. A.; Tour, J. M. *Science* **1990**, *286*, 1550-1552.
- [51] Katz, H. E.; Wilson, W. L.; Scheller, G. *J. Am. Chem. Soc.* **1994**, *116*, 6636-6640.
- [52] Malem, F.; Mandler, D. *Anal. Chem.* **1993**, *65*, 37-41.
- [53] Gooding, J. J.; Praig, V. G.; Hall, E. A. H. *Anal. Chem.* **1998**, *70*, 2396-2402.
- [54] Giz, M. J.; Duong, B.; Tao, N. J. *J. Electroanal. Chem.* **1999**, *465*, 72-79
- [55] Chen, D.; Li, J. *Surface Sci. Reports* **2006**, *61*, 445-463.
- [56] Love, J. C.; Estroff, L. A.; Kriebel, J. K.; Nuzzo, R. G.; Whitesides, G.M. *Chem. Rev.* **2005**, *105*, 1103-1169.
- [57] Nuzzo, R. G.; Zegarski, B. R.; Dubois, L. H. *J. Am. Chem. Soc.* **1987**, *109*, 733-740.
- [58] Valiokas, R.; Svedhem, S.; Svensson, S. C. T.; Liedberg, B. *Langmuir* **1999**, *15*, 3390-3394.
- [59] Schlenoff, J. B.; Li, M.; Ly, H. *J. Am. Chem. Soc.* **1995**, *117*, 12528.
- [60] Antonello, S.; Benassi, R.; Gavioli, G.; Taddei, F.; Maran, F. *J. Am. Chem. Soc.* **2002**, *124*, 7529-7538.
- [61] Poirier, G.E. *Langmuir* **1997**, *13*, 2019-2026.
- [62] Paradis, E.; Rowtree, P. *J. Electroanal. Chem.* **2003**, *550*, 175-185.
- [63] Zhang, L.; Goddard, W. A.; Jiang, S. *J. Chem. Phys.* **2002**, *117*, 7341-7349.
- [64] Jiang, S. *Mol. Phys.* **2002**, *100*, 2261-2275.
- [65] Fischer, D.; Curioni, A.; Andreoni, W. *Langmuir* **2003**, *19*, 3567-3571.
- [66] Heister, K.; Zharnikov, M.; Grunze, M.; Johansson, L. S. O. *J. Phys. Chem. B* **2001**, *105*, 4058-4061.
- [67] Yang, Y. W.; Fan, L. J. *Langmuir* **2002**, *18*, 1157-1164.
- [68] Dubois, L. H.; Zegarski, B. R.; Nuzzo, R.G. *J. Chem. Phys.* **1993**, *98*, 178-188.
- [69] Camillone, N.; Chidsey, C. E. S.; Eisemberger, P.; Fenter, P.; Li, J.; Liang, K. S.; Liu, G. Y.; Scoles, G. *J. Chem. Phys.* **1993**, *99*, 744-747.

- [70] Fenter, P; Eisemberger, P.; Liang, K. S. *Phys. Rev. Lett.* **1993**, *70*, 2447-2450.
- [71] Seydack, M., *Biosens Bioelectron* (2005) *20*, 2454.
- [72] Roy, S., and Gao, Z., *Nano Today* (2009) *4*, 318.
- [73] Pumera, M., et al., *Sensors and Actuators B* (2007) *123*, 1195.
- [74] Rosi, N. L., and Mirkin, C. A., *Chem Rev* (2005) *105*, 1547.
- [75] De la Enconsura-Muñiz A, Parolo C., Merkoçi A, *Materialstoday* (2010), 13.
- [76] De la Enconsura-Muñiz, A.; *Trends Anal Chem* (2008) *27* (7), 568.
- [77] Karle, I. L.; Balaram, P. *Biochemistry* **1990**, *29*, 6747-6756.
- [78] (a) Toniolo, C.; Crisma, M.; Formaggio, F.; Peggion, C. *Biopolymers* **2001**, *60*, 396-419. (b) Crisma, M.; Moretto, A.; Formaggio, F.; Toniolo, C. *Biopolymers* **2006**, *84*, 3-12.
- [79] Goodman, M.; Toniolo, C.; Pallai, P. In *Forum Peptides*; Castro, B., Martinez, J., Eds.; Nancy Dohr: France, 1985; pp 146-174.
- [80] (33) Toniolo, C.; Bonora, G. M.; Barone, V.; Bavoso, A.; Benedetti, E.; Di Blasio, B.; Grimaldi, P.; Lelj, F.; Pavone, V.; Pedone, C., *Macromolecules* **1985**, *18*, 895-902.
- [81] (a) Improta, R.; Barone, V.; Kudin, K. N.; Scuseria, G. E. *J. Am. Chem. Soc.* **2001**, *123*, 3311-3322. (b) Shin, Y.-G; Newton, M. D.; Isied, S. S. *J. Am. Chem. Soc.* **2003**, *125*, 3722-3732. (c) Wieczorek, R.; Dannenberg, J. *J. Am. Chem. Soc.* **2004**, *126*, 14198-14205.
- [82] (a) Kennedy, D. F.; Crisma, M.; Toniolo, C.; Chapman, D. *Biochemistry* **1991**, *30*; (b) Hanson, P.; Millhauser, F.; Formaggio, F.; Crisma, M.; Toniolo, C. *J. Am. Chem. Soc.* **1996**, *118*.
- [83] (a) Fabris, L.; Antonello, S.; Armelao, L.; Donkers, R. L.; Polo, F.; Toniolo, C.; Maran, F., *J. Am. Chem. Soc.* **2006**, *128*, 326-336. (b) Holm, A. H.; Ceccato, M.; Donkers, R. L.; Fabris, L.; Pace, G.; Maran, F., *Langmuir* **2006**, *22*, 10584-10589.
- [84] Perera, N. V.; Isley, W.; Maran, F.; Gascón, J. A. *J. Phys. Chem. C* **2010**, *114*, 1643-16050.
- [85] Wen, X. G.; Linton, R. W.; Formaggio, F.; Toniolo, C.; Samulski, E. T. *J. Phys. Chem. A* **2004**, *108*, 9673-9681.

- [86] a) Antonello, S.; Formaggio, F.; Moretto, A.; Toniolo, C.; Maran, F. *J. Am. Chem. Soc.* **2003**, *125*, 2874-2875. (b) Polo, F.; Antonello, S.; Formaggio, F.; Toniolo, C.; Maran, F. *J. Am. Chem. Soc.* **2005**, *127*, 492-493.
- [87] (a) Improta, R.; Antonello, S.; Formaggio, F.; Maran, F.; Rega, N.; Barone, V. *J. Phys. Chem. B* **2005**, *109*, 1023-1033. (b) Improta, R.; Barone, V.; Newton, M. D.; *Chemphyschem*, **2006**, *7*, 1211.
- [88] Becucci, L.; Guryanov, I.; Maran, F.; Guidelli, R. *J. Am. Chem. Soc.* **2010**, *132*, 6194-6204.
- [89] Hesari, M.; Antonello, S.; Armelao, L.; Gobbo, P.; Guidelli, R.; Guryanov, I.; Rampi, M. A.; Soldà, A.; Maran, F. Manuscript in preparation.
- [90] Lvov, Y.M Thin-Film Nanofabrication by alterbate Absorption of Polyions, Nanoparticles, and Proteins. *In Handbook of Surface and Interface of Material: Nanostructured Materials, Micelles, and Colloids*; Nalwa, H.S, Ed.; Academic Press: San Diego, 2001; Vol. 3, 170-189.
- [91] Angerstein-Kozłowska, H.; Conway, B. E.; Hamelin, A.; Stoicoviciu, L. *J. Electroanal. Chem.* **1987**, *228*, 429-453. Tkac, J.; Davis, J. J. *J. Electroanal. Chem.* **2008**, *621*, 117-120.
- [92] Haiss, W.; Thanh, N. T. K.; Aveyard, J.; Fernig, D. G.; *Anal. Chem.* **2007**, *79*, 4215-4221.
- [93] Galus Z.; *Fundamentals of electrochemical analysis*, 2nd Edition, Polish Scientific Publishers Pwn, **1976**.
- [94] Juntao Lu and Peifang Liu, *J. Electroanal. Chem.*, **1988**, *244*, 339.
- [95] Engstrom, R. C.; Weber, M.; Wunder, D. J.; Burgess, R.; Winqvist, S.; *Anal. Chem.* **1986**, *58*, 844.
- [96] Tanaka, K.; Tamamushi, R.; *Bioelectrochem. Bioenerg.* **1987**, *17*, 519.
- [97] Tanaka, K.; Kashiwagi, N.; *Bioelectrochem. Bioenerg.* **1988**, *20*, 1.
- [98] Zamlynni, V. PhD Thesis Work, “*Electrochemical and Spectroscopic Studies of Pyridine Surfactants at the Gold-Electrolyte Interface*”, **2002**, University of Guelph, ON Canada.
- [99] Sheppard, N.; Erkelens, J. *Appl. Spec.* **1984**, *38*, 471-485.
- [100] Toniolo, C.; Bonora, G. M.; Barone, V.; Bavoso, A.; Benedetti, E.; Di Blasio, B.; Grimaldi, P.; Lelj, F.; Pavone, V.; Pedone, C.; *Macromolecules* **1985**, *18*, 895-902

- [101] Buffeteau, T.; Desbat, B., *Appl. Spec.* **1989**, *6*, 1027-1032.
- [102] Strong, L.; Whitesides, G. M., *Langmuir* **1988**, *4*, 546-558.
- [103] Swalen, J. D.; Allara, D. L.; Andrade, J. D.; Chandross, E. A.; Garoff, S.; Israelachvili, J.; McCrthy, T. J.; Murray, R.; Pease, R. F.; Rabolt, J. F., Wynne, K. J.; Yu, H.; *Langmuir* **1987**, *3*, 932.
- [104] (a) Wen, X.; Linton, R.W.; Formaggio, F.; Toniolo, C.; Samulski, E.T.; *J. Phys. Chem. A* **2004**; (b) Enriquez, E. P.; Samulski, E.T. *Mat. Res. Soc. Symp. Proc.* **1992**, *255*, 423.
- [105] Greenler, R. G., *J. Chem. Phys.* **1966**, *44*, 310-315.
- [106] Michl, J.; Thulstrup, E. W.; *Spectroscopy with Polarized Light: Solute alignment by Photoselection, in Liquid Crystal, Polymers, and Membranes*; VCH Publishers: Deerfield Beach, FL, **1986**.
- [107] Tsuboi, M.; *J. Polymer Sci.* **1962**, *59*, 139-153.
- [108] Arikuma, Y.; Takeda, K.; Morita, T.; Ohmae, M.; Kimura, S. *J. Phys. Chem. B* **2009**, *113*, 6256–6266.
- [109] Kraatz, H.-B.; Bediako-Amoa, I.; Gyepi-Garbrah, H.; Sutherland, T. C. *J. Phys. Chem. B.* **2004**, *108*, 20164-20172.
- [110] Mandal, H. S.; Kraatz, H. B. *Chem. Phys.* **2006**, *326*, 246–251.
- [111] (a) Kitagawa, K.; Morita, T.; Kimura, S. *Thin Solid Films* **2006**, *509*, 18–26. (b) Watanabe, J.; Morita, T.; Kimura, S. *J. Phys. Chem. B* **2005**, *109*, 14416-14425. (c) Kitagawa, K.; Morita, T.; Kimura, S. *J. Phys. Chem. B* **2004**, *108*, 15090-15095.
- [112] Ward, M. A., Catto, J.W.F., Hamdy, F.C., *Ann. Clin. Biochem*, 2001, *38*, 633-651.
- [113] Cattarin, S.; Kramer, D.; Lui, A.; Musiani, M.; *J. Phys. Chem. C* **2007**, *111*, 12643-12649.